

# Comparative analysis of dynamic stall models for wind turbines airfoils

Mcs Thesis

Erik Grigoryants



# Comparative analysis of dynamic stall models for wind turbines airfoils

by

Erik Grigoryants

Student Name	Student Number
Erik Grigoryants	5742048

Main supervisor: D. von Terzi  
PHD supervisor: S. Chellini  
Project Duration: September, 2023 - April, 2024  
Faculty: Faculty of Aerospace Engineering, Delft

# Acknowledgements

*"A precious stone cannot be polished without friction, nor can a man be perfected without trials" - Seneca, 4 AD - 65 AD.*

This work is the culmination of my studies at the Technical University of Delft. The path has not always been easy, but it has always been fascinating and inspiring.

The writing of this thesis would not have been possible without the support of my wonderful teachers who supported me every step of the way. I sincerely thank my daily supervisor, Simone Chellini, for his support, patience, and enthusiasm. I also want to express my gratitude to my main supervisor, Prof. Dominic von Terzi, for guiding me and never leaving me without food for thought and motivation. I also express my gratitude to Professor Delphine de Tavernier, who introduced me to the topic and supported me in the early stages of the project. Your guidance significantly influenced my personal and professional development.

I also thank Niels Adema for allowing me to use his model's source code. It is in such interactions that the true driving force of science lies.

Of course, I cannot forget about my beloved family in the Netherlands, parents, sister, and girlfriend back home. Your support has been absolutely crucial to my success, and I cannot thank you enough.

And finally, all my new friends at TU Delft. This period of my life will undoubtedly remain in my memory as a happy one. Thank you for all the time we spent together.

*Erik Grigoryants  
Delft, May 2024*

# Nomenclature

## Abbreviations

Abbreviation	Definition
AoA	Angle of Attack
IEA	International Energy Agency
LLT	Low speed Low Turbulence
M	Mach number
RWT	Reference Wind Turbine
BL	Beddoes-Leishman
Re	Reynolds number

## Symbols

Symbol	Definition	Unit
$S$	Time parameter	[-]
$A$	Amplitude	[°]
$A_i$	Coefficients of indicial response function	[-]
$b_i$	Exponents of indicial response function	[-]
$C_{N\alpha}$	Slope coefficient of the normal force coefficient	[-]
$C_N^C$	Normal circulatory force	[-]
$C_L$	Lift coefficient	[-]
$C_m$	Pitching moment coefficient	[-]
$C_N^l$	Norman noncirculatory force	[-]
$C_N^p$	Normal force under potential flow conditions	[-]
$C_N^f$	Normal force coefficient for adapted nonlinear conditions	[-]
$C_N^I$	Noncirculatory (impulsive) normal force coefficient	[-]
$C_N^v$	Vortex induced normal force coefficient	[-]
$C_M^v$	Vortex induced pitching moment coefficient	[-]
$C_v$	Vortex lift increment	[-]
$CP_v$	Vortex induced center of pressure	[-]
$C_N^{dynamic}$	Total dynamic normal force coefficient	[-]
$c_{l,dyn}$	Dynamic lift coefficient	[-]
$c_{l,static}$	Static lift coefficient	[-]
$c_{l,pot}$	Potential lift coefficient	[-]
$cf_i$	Snel model coefficients	[-]
$\Delta c_{l,i}$	Lift coefficient corrections	[-]
$D_p, D_f$	Deficiency functions	[-]
$f, f', f''$	Frequency / Trailing edge separation point, Effective, Instantaneous	[-]
$ft_i$	Forcing terms	[-]
$k$	Reduced frequency	[-]
$K_\alpha$	Factor associated with the noncirculatory time constant	[-]

Symbol	Definition	Unit
$K_N$	Kirchhoff approximation parameter	[-]
$k_s$	Strouhal frequency	[-]
$n$	Current time sample	[-]
$M$	Mach number	[-]
$r$	reduced pitch	[-]
$t$	Time	[s]
$T_l$	Noncirculatory time constant	[-]
$T_p, T_f, T_v$	Time constants (semi-chords)	[-]
$T_{vl}$	Vortex passage time constant	[-]
$U_\infty$	Free-stream velocity	
$X, Y$	Circulatory deficiency function	[-]
$\alpha$	Angle of Attack	[°]
$\alpha_o$	Mean angle of oscillation	[°]
$\alpha_E$	Effective Angle of Attack	[°]
$\alpha_{max}$	Maximum Angle of Attack	[°]
$\beta$	Prandtl-Glauert compressibility factor	[-]
$\tau$	Time constant	[-]
$\cdot$	Time derrivative	

# Summary

Wind energy is a crucial component of the ongoing energy transition. Over the past decade, technologies in this field have advanced significantly. Currently, the industry is following a trend of increasing the size of wind turbines, both onshore and offshore units. However, this trend brings about complexities in design, maintenance, and operation. Wind turbines are highly dynamic structures, and accurate prediction of dynamic loads is crucial for future design and, consequently, installation costs and lifetime expectancy.

Dynamic stall is a highly dependent process influenced by various parameters such as Reynolds number and airfoil geometry. It involves significant changes in pressure in the flow field around the airfoil due to the development and shedding of vortex structures from the leading or trailing edge. Another characteristic is flow reversal from the trailing edge, leading to a delay in boundary layer attachment and the formation of significant hysteresis in lift force, pitching moment, and drag force values. Due to the constant rotation of the rotor, this process is cyclic, necessitating accurate modeling for proper assessment of fatigue damage, instability levels, and turbine noise.

This study aims to compare the results of dynamic stall models for the FFA-W3-211 airfoil, with a maximum thickness of 21.1% of the chord length. Previously unavailable dynamic data for the considered airfoil is obtained through experiments in a Low-Speed Low-Turbulence Wind Tunnel located at TU Delft. Static and dynamic polars are obtained for various Reynolds numbers, amplitudes, mean angles, and oscillation frequencies. Measurements are conducted using pressure taps located on the airfoil model, and static data is validated against existing data and RFOIL results.

The study considers two semi-empirical models. The first is the Beddoes-Leishman model, one of the most popular at the time of writing. Its optimization and comparison with the default version revealed that optimized shape-based coefficients are crucial for obtaining correct results. It is found that the optimized model significantly outperforms the default version in almost all cases. Additionally, it is established that the model lacks the leading edge vortex effect in modeling negative stall.

The second model chosen is the first-order Snel model. Optimization of this model also led to significant improvements in the results obtained. A significant improvement in modeling both hysteresis size and reattachment area with increasing Reynolds number is identified. However, a significant drawback of the model in modeling negative stall is revealed. During upstroke motion, the model predicts trailing edge vortex effects instead of leading edge, which negatively affects the overall model performance.

Comparison of the two models identified their strengths and weaknesses. The Beddoes-Leishman model appears more stable for all cases considered, while the Snel model is sensitive to changes in Reynolds number. It is also noted that both models have difficulties in correctly determining dynamic stall onset angle of attack and the slope of the normal force coefficient. Additionally, both models tend to overpredict values in a greater number of cases.

When comparing negative stall, the optimized Beddoes-Leishman model performs significantly better than the Snel model. It accurately predicts the overall form and severity of hysteresis as well as the reattachment area. The Snel model requires additional modifications for correct modeling of negative stall.

# Content

<b>Acknowledgements</b>	<b>i</b>
<b>Nomenclature</b>	<b>ii</b>
<b>Summary</b>	<b>iv</b>
<b>1 Introduction</b>	<b>1</b>
1.1 Motivation for the research	1
1.2 Research questions and thesis structure	3
<b>2 Dynamic stall</b>	<b>5</b>
2.1 Physical mechanisms	5
2.2 Understanding, Implications, and Advances	7
2.3 Effect of parameters	9
<b>3 Dynamic stall modelling</b>	<b>11</b>
3.1 Beddoes-Leishman model	12
3.1.1 Modifications review	14
3.2 Snel model	16
3.2.1 Snel model modifications review	17
<b>4 Experimental methodology</b>	<b>18</b>
4.1 Facility	19
4.2 Experimental methods	19
4.2.1 Pressure taps	19
4.2.2 Thermal imaging	20
4.2.3 Wake measurements	20
4.2.4 Positioning of the model	20
4.3 Wind tunnel model	21
4.4 Corrections	23
4.5 Experimental matrices	24
4.5.1 Static polars	24
4.5.2 Dynamic polars	24
<b>5 Beddoes-Leishman model optimization results</b>	<b>31</b>
5.1 Optimization	31
5.2 $T_p$ coefficient determination	32
5.3 Comparison parameters	33
5.4 Results comparison	33
5.4.1 Oscillation around $\alpha_0 = 11^\circ$ at $Re = 1 \times 10^6$	35
5.4.2 Oscillation around $\alpha_0 = 11^\circ$ at $Re = 2 \times 10^6$	36
5.4.3 Oscillation around $\alpha_0 = -8^\circ$ at $Re = 1 \times 10^6$	40
5.4.4 Oscillation around $\alpha_0 = -8^\circ$ at $Re = 2 \times 10^6$	40
<b>6 Snel model optimization results</b>	<b>44</b>
6.1 Results comparison	45
6.1.1 Oscillation around $\alpha_0 = 11^\circ$ at $Re = 1 \times 10^6$	45
6.1.2 Oscillation around $\alpha_0 = 11^\circ$ at $Re = 2 \times 10^6$	46
6.1.3 Oscillation around $\alpha_0 = -8^\circ$ at $Re = 1 \times 10^6$ and $Re = 2 \times 10^6$	49
<b>7 Model comparison</b>	<b>53</b>
7.1 Oscillation around $\alpha_0 = 11^\circ$ at $Re = 1 \times 10^6$ and $Re = 2 \times 10^6$	53
7.2 Oscillation around $\alpha_0 = -8^\circ$ at $Re = 1 \times 10^6$ and $Re = 2 \times 10^6$	54

---

<b>8</b>	<b>Conclusions and Further work</b>	<b>63</b>
8.1	Evaluation of the Beddoes-Leishman model results . . . . .	63
8.2	Evaluation of the Snel model results . . . . .	64
8.3	Evaluation of model comparison results . . . . .	64
8.4	Further research . . . . .	65
	<b>References</b>	<b>68</b>
<b>A</b>	<b>Additional dynamic polars</b>	<b>72</b>
<b>B</b>	<b>Figures for <math>\alpha_0 = 0^\circ</math></b>	<b>74</b>
<b>C</b>	<b><math>T_P</math> coefficient determination</b>	<b>77</b>
<b>D</b>	<b>Beddoes-Leishman cases comparison</b>	<b>80</b>
D.1	Oscillation around a mean angle of $\alpha_0 = 11^\circ$ . . . . .	80
D.2	Oscillation around a mean angle of $\alpha_0 = -8^\circ$ . . . . .	81
<b>E</b>	<b>Snel cases comparison</b>	<b>82</b>
E.1	Oscillation around a mean angle of $\alpha_0 = 11^\circ$ . . . . .	82
E.2	Oscillation around a mean angle of $\alpha_0 = -8^\circ$ . . . . .	83

# 1

## Introduction

### 1.1. Motivation for the research

The current wind energy development is an impressive upsurge compared to historical beginnings. Over the past three decades, Figure 1.1, there has been a tremendous leap in installed capacity (IRENA, 2018). This rapid progress has been made possible by, among other factors, an in-depth study of the complex aerodynamics of wind turbines. The result has been technological solutions that significantly increase the efficiency of wind power plants. At the same time, there has been a strong adoption of advanced materials and innovative manufacturing methods, contributing to developing more reliable and efficient blades for wind turbines. The adoption of the Paris Agreement by countries, as well as individual country targets aimed at increasing installed wind power capacity (IEA, 2020), (Vasakova et al., 2011) and many other confirm the importance of the development of this energy sector worldwide.

Wind Turbine industry is currently experiencing a trend of wind turbine size increase. Larger machines are capable of extracting more energy from the wind, therefore reducing the carbon footprint and bringing even more clean energy to the communities. However, larger and larger sizes introduce ever-increasing difficulties in design optimization and control strategies (Lantz et al., 2019). Dynamic stall appears as one of the many challenges faced by the wind energy sector.

Dynamic stall, a complex aerodynamic phenomenon characterized by a sudden loss of lift and an increase in drag, represents a critical challenge in the aviation and wind energy sectors. It occurs as a result of variations in the inflow conditions caused by yaw misalignment (Tran et al., 2014), wind turbulence (Kim & Xie, 2016), shear and gusts (Wong, Rival, et al., 2016), tower shadow (Yoshida, 2020), and aero-elastic effects of the blade (Corke & Thomas, 2015). Regardless of the cause, this phenomenon has a significant effect on the blade lift and drag forces, as well as the development of excessive moments and negative damping (Mallik & Raveh, 2020), which leads to increased fatigue (X. Liu et al., 2020) and high risk of dangerous instabilities (Faber, 2018).

Dynamic stall is important to accurately model the aerodynamic forces and estimate the extreme and fatigue loads. In dynamic stall modelling, extensive research has led to the creation of various models and their refined versions. These models exhibit a remarkable ability to predict the aerodynamic behavior of a pitching airfoil, while also maintaining computational simplicity. As a result, they have become indispensable tools for researchers and manufacturers in the study and construction of wind turbines.

Dynamic stall models are primarily semi-empirical. This means that their application requires input data such as static lift coefficients, drag force coefficients and moments that can be obtained through experiments. The wind tunnel is an integral part of the process of studying aerodynamic effects and obtaining data, including the study of dynamic stall. Over the years, dynamic stall research has conducted many wind tunnel experiments that have characterized and collected data for many types of airfoil (McCroskey et al., 1982), (J. Leishman, 1990), (Rice et al., 2019). Typically, wind tunnel experiments employed 2D pitching models (Ferreira et al., 2007), demonstrating their representativeness

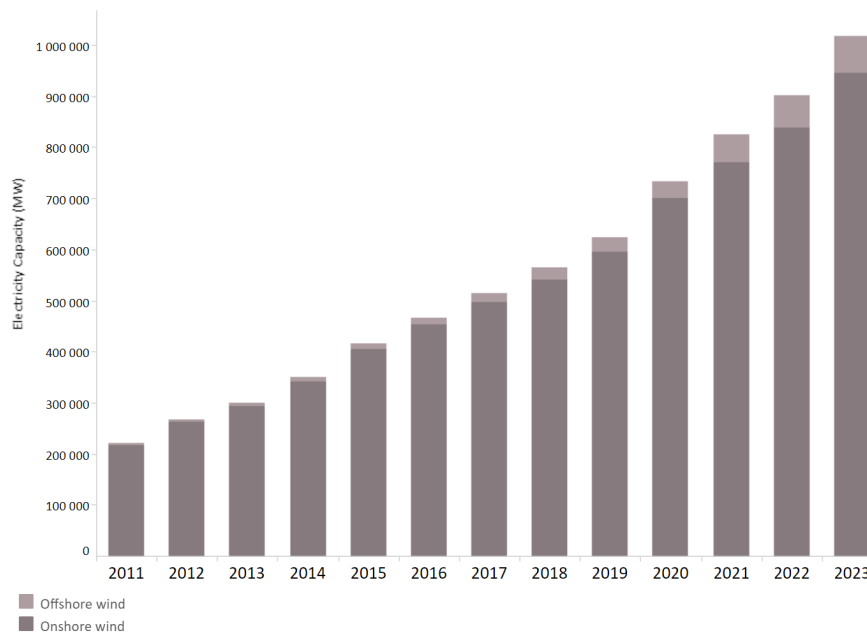


**Figure 1.1:** Worldwide installed wind energy capacity (“IRENA – International Renewable Energy Agency”, 2024)

for dynamic stall phenomena. These tests offered valuable insights into dynamic stall characteristics, including onset behavior, sensitivity to Reynolds and Mach numbers, and dependence on airfoil geometry. Additionally, they yielded quantitative aerodynamic load measurements.

There are many different models that are widely used in popular software to model the wind turbine behaviour, such as OpenFAST (“Unsteady Aerodynamics — OpenFAST documentation”, n.d.). There is no clear answer as to which model is the best, and additional research is required to better understand the differences between these models and their performance for different airfoils and operational regimes. It is essential to recognize that no single model can capture all aspects of dynamic stall across various conditions. Therefore, continued investigation and validation of dynamic stall models using experimental data are necessary to improve their accuracy and reliability.

Another important instrument in the wind energy industry development are reference wind turbines (RWTs). They play a vital role by providing openly available data for models representing current wind turbine technology. These models are utilized across various disciplines, including aerodynamic, structural, and aeroelastic turbine modelling, as well as wind farm flow modeling. Early RWT examples include the NREL WindPACT turbine series (Rinker et al., 2018) and the NREL 5 MW RWT (NREL, 2009). With the continuous development of commercial turbine technology, upscaling to larger power ratings has become prevalent in the offshore wind energy market. The wind energy community has recognized the need for larger offshore reference wind turbines to address this trend. These larger RWTs enable researchers and practitioners to investigate future turbine technology, identify technological challenges, and evaluate the suitability of numerical modeling tools and design practices for the next generation of offshore wind turbines. The development and maintenance of these larger RWTs, such as those with power ratings exceeding 15 MW, are essential for advancing offshore wind energy technology and ensuring its continued growth and success.

Different types of airfoils from FFA-W3 family are used in the latest reference turbines, such as a DTU 10 MW (*The DTU 10-MW reference wind turbine*, 2013), IEA Wind 15-Megawatt Offshore Reference Wind Turbine (Gaertner et al., 2020) and recently released IEA Wind 22-Megawatt Offshore Reference Wind Turbine (Zahle et al., 2024). The tip airfoil section is particularly important as it is a key area for capturing energy (Xi & Zhao, 2022). It is also found that the flapwise and edgewise extreme bending moments near the blade tip exhibit larger sensitivity towards uncertainty in the static airfoil data compared to the blade root (Abdallah et al., 2015).

Despite the tip airfoil importance and wide use of the FFA-W3-211 airfoil in the reference turbines, there are only a limited amount of research dedicated to this airfoil, for example Bertagnolio et al., 2001. Experimental data on the dynamic stall behavior of the FFA-W3-211 airfoil are not available at the time of writing. The lack of data can significantly impact the dynamic stall modeling results. More accurate modeling of this effect can have an impact on the predictions of the power produced as well as the fatigue loads, especially as uncertainties in dynamic loading predictions can reach 30% (Scheepers & Snel, 2007).

To address this gap, this thesis aims to perform experiments in an LLT wind tunnel and compare the results with the considered models. The objective is to obtain static and dynamic polars over a range of Reynolds numbers, reduced frequencies, amplitudes and mean angles of attack for the FFA-W2-211 airfoil. The optimization process is then carried out for two selected semi-empirical models: the Beddoes-Leishman model and the first-order Snell model. In addition, a two-dimensional comparison of the optimized models with recently obtained experimental data is present. This holistic approach offers valuable insights into how the FFA-W3-211 airfoil behaves dynamically, aiding in the advancement of dynamic airfoil modeling for wind turbine design and analysis.

## 1.2. Research questions and thesis structure

In order to achieve the aim of the thesis, it is important to set up the proper research question:

**How do various optimized models perform in simulating dynamic stall compared to experimental data for the FFA-W3-211 airfoil?**

To address the stated problem, this paper is organized into chapters, each of which answers one of the sub-questions and eventually answers the stated research question.

Chapter 2 answers the question:

- What are the physical mechanisms of dynamic stall?

This chapter focuses on the phenomenon of dynamic stall itself. A literature review is conducted, exploring advances in the understanding of the physical mechanisms underlying dynamic stall. In addition, this chapter discusses the different phases of stall and the effects of different parameters on the flow characteristics. This chapter provides a deeper understanding of dynamic stall, its effects and applications in aerodynamics.

Chapter 3 addresses the following question:

- What are the methods for modeling dynamic stall?

This chapter reviews the most common methods used for dynamic stall modeling. It provides detailed descriptions of these methods and describe modifications added to these models over the years of research. The purpose of this analysis is to gain an understanding of the strengths and limitations of the various approaches to dynamic stall modeling.

Chapter 4 provides an in-depth exploration of the experimental aspect of the project. It is outline the experimental setup, detailing the methodology used for data collection. Additionally, the chapter discusses the process of data measurement, including any relevant instrumentation and techniques employed. Furthermore, it offers insights into the methods used for data processing and post-processing to ensure accurate and meaningful analysis of the experimental results.

The subsequent chapters, 5 and 6, addresses the following inquiries:

- How are the models optimized to align with the experimental data?
- How does the performance of the optimized model compare to that of the default model?

These chapters reviews the optimization procedures for the selected models, describe methods for evaluating their performance, and make comparative analyses between the optimized and standard models.

Chapter 7, the focus of which is the question:

- How do the results of optimized models compare to the experimental data?

In this chapter, the results of optimized models are compared with the experimental data.

Finally, in Chapter 8, the obtained results are discussed, and suggestions for further work is provided.

# 2

## Dynamic stall

Understanding the stall process is essential for design and operation in aviation and wind energy applications. Dynamic stall is associated with a sharp drop in lift and an increase in the drag force. This leads to excessive loads and instability in the operation of the devices (Ormiston & Bousman, 1975). In the case of dynamic operating conditions, which are directly related to the operation of wind turbines, there is a risk of entering dynamic stall. This regime is a more complex process than static stall and has a greater impact on important factors in equipment operation, such as power production and fatigue loads (Butterfield et al., 1991).

This chapter discusses the main physical characteristics of dynamic stall phenomena. It is organized as follows: Section 2.1 presents an overview of the physical mechanisms underlying dynamic stall. Then, section 2.2 presents a literature review of dynamic stall research conducted in recent years and highlights advances in its understanding. Finally, 2.3 summarizes the influence of key parameters on dynamic stall characteristics.

### 2.1. Physical mechanisms

Stall occurs when a certain angle of attack (AoA) is exceeded. As known, an increase in AoA results in increase in lift force. However, this trend stops at a certain critical value of the AoA. This value corresponds to the boundary layer detachment on a large scale and a drastic drop in the lift force. This phenomenon is known as a static stall (Y. Liu et al., 2012).

Significant differences can be observed when the airfoil experiences dynamic, oscillatory motion and, as a consequence, the AoA constantly changes. The resulting phenomenon is called dynamic stall. An important distinguishing characteristic of dynamic stall as opposed to a static, is the formation of a large leading edge vortex (**carr-1988A**). In his work McCroskey showed that it is associated with the highly nonlinear fluctuating pressure field (McCroskey, 1981).

A proper understanding of the dynamic stall effect on airfoils requires observations well before the noticeable change in polars. Referring to Figure 2.1, the sequence initiates at point (a), when the airfoil in motion exceeds the static stall AoA without any variation in the surrounding flow. Further increase of AoA past the critical value results in point (b) with gradual flow reversal. It starts at the trailing edge and continuously progresses towards the leading edge.

Initiation of the following stage, point (e), highly depends on parameters such as motion characteristics, geometric shape, and Reynolds number. There, the boundary layer can no longer be considered thin and attached and formation of the strong vortical flow at the leading edge begins.

Process (g) describes the development of the vortex structure at the leading edge. This structure moves

rearward at approximately half of the free-stream velocity (*Handbook of Wind Energy Aerodynamics*, 2022). the moving vortex introduces distortion in the pressure distribution along the airfoil surface, resulting in discrepancies between static and dynamic values. For instance, pitch moment experiences a rapid decrease to negative values. Drag forces start to increase. However, lift continues to increase until the vortex structure crosses the mid-chord. This behavior is referred to as vortex-induced lift (*Handbook of Wind Energy Aerodynamics*, 2022). Process (g) is also known as moment stall, as the change in the position of the pressure center causes a large nose-down pitching moment. Described vorticity accumulation on the surface is often used in DS models to predict the aerodynamic behavior of the airfoil (see chapter 3).

Upon reaching a certain angle of attack, point (h), the formed vortex advances to the trailing edge and detaches from the airfoil surface into the wake. This process is accompanied by a sharp drop in lift force and transitioning to the full stall regime, points (i) and (j), respectively. The flow on the blade surface becomes completely detached.

Reverse motion of the airfoil, process (k), is accompanied by a major delay in the attachment of the boundary layer and the formation of a significant hysteresis in the values of lift force, pitching moment, and drag force.

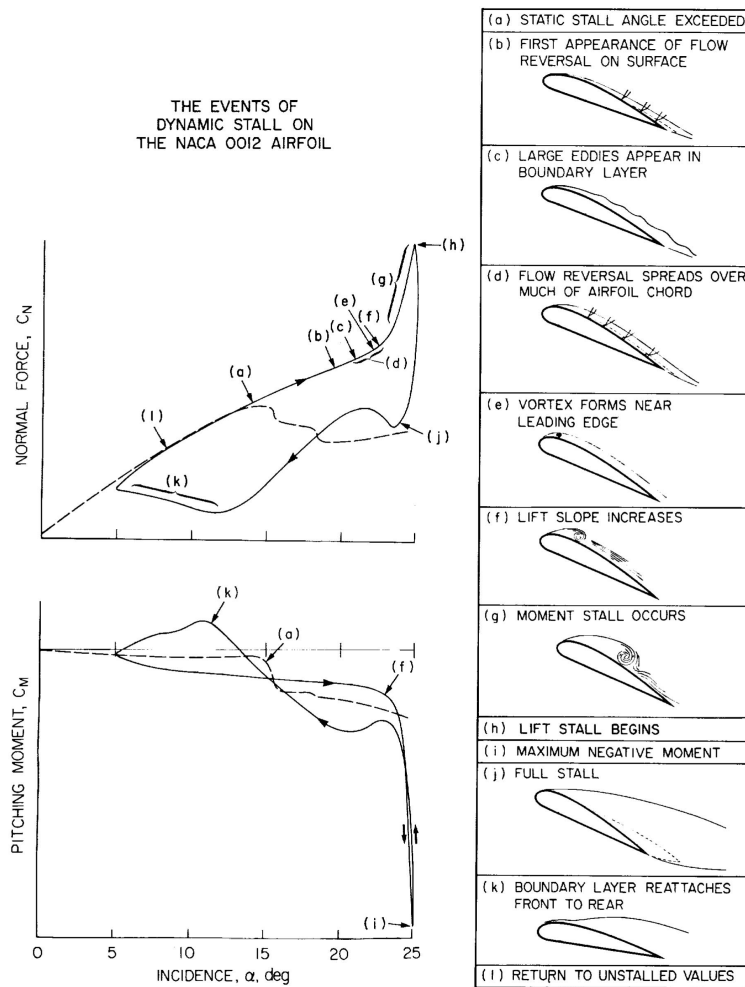


Figure 2.1: Dynamic stall stages on NACA 0012 airfoil, (McCroskey, 1981)

## 2.2. Understanding, Implications, and Advances

Dynamic stall challenges are of interest to researchers for a long time. For example, Halfman et al., 1951 investigated stall-flutter. Their manuscript describes the effects of blade geometry, Reynolds number, mean angle of attack, and other parameters on the behavior of lift and momentum in both pitching and translational oscillations. The work emphasizes the high complexity of the phenomenon under investigation, as well as the lack of tools for predicting aerodynamic responses under dynamic stalling conditions.

In subsequent years, researchers turned their attention to studying dynamic stall within the realm of helicopter blade design. This shift is driven by the frequent occurrence of blade stall during high-speed and complex maneuvers performed by pilots. As a consequence, helicopter blades often enter stall, leading to torsional stresses during portions of each revolution where blade stalling is anticipated.

Several key observations emerged from this research. Firstly, peak loading is found to increase with higher pitching rates, particularly within the range where loading is vortex-induced. Additionally, it is noted that the pitch axis location has minimal influence on peak loading, indicating a lack of sensitivity to heaving velocity and the dynamic stall angle of attack. Perhaps most notably, the rate of change of angle of attack is identified as the dominant factor in determining vortex-induced peak lift and moment during dynamic stall.

In the following years, research aimed at gaining a deeper understanding of the mechanisms underlying dynamic stall has intensified. For instance, the paper by (Johnson & Ham, 1972) puts forth a theory elucidating the origin of the stall angle of attack delay during dynamic stall of an airfoil. The authors attribute this delay and other dynamic stall features to the behavior of the laminar separation bubble on the airfoil's leading edge. They found that dynamic stall occurs when suction is lost at the 15% chord station. Comparing the dynamic stall angle with the angle at which the bubble reattachment point passes the 15% chord station revealed nearly identical delays at each angle due to pitch rate. The authors argue convincingly for the significant influence of the leading edge shed vortex on dynamic stall characteristics. However, there is still a lack of experimental data and theoretical understanding to develop mathematical models capable of accurately predicting the flow behavior associated with dynamic stall.

During the same period, researchers actively expanded both the experimental database and theoretical understanding of dynamic stall processes. For instance, the study by (McAlister et al., 1978) presents an extensive examination of dynamic stall on the NACA 0012 airfoil using hot-wire probes and surface-pressure transducers. Significant results are obtained, indicating that the leading-edge separation bubble has no direct effect on the gross stall character and persists even during the onset of suction collapse. Moreover, the study revealed a correlation between the strength of the stall vortex and the airfoil's circulation at the time of vortex formation. With additional data on vortex origin time and shedding velocity, the study suggests that a semi-empirical model for the airfoil oscillating through stall becomes feasible.

Additionally, numerous efforts are made to visualize dynamic stall under various conditions. For instance, (McAlister & Carr, 1979) conducted flow visualizations to independently expose the behavior of the viscous and inviscid domains during unsteady airfoil stall using a water tunnel. Their experiments revealed that the onset of dynamic stall is characterized by a rapid movement of flow reversal toward the leading edge of the airfoil. Furthermore, experiments conducted in a water environment enabled the establishment of more precise mechanisms of dynamic-stall vortex occurrence, highlighting the emergence of minor protuberances that eventually transform into the aforementioned vortices. These phenomena are more noticeable in experiments conducted in an air environment with higher Reynolds numbers.

In their papers, (Ericsson & Reding, 1972) and (Ericsson & Reding, 1980), explored the quasi-steady theory, where time-history effects are condensed into one discrete past-time event, and the accelerated-flow effect is represented by an equivalent time lag. Their findings revealed that the accelerated flow

generated by nonzero pitch rates is a primary characteristic of leading and trailing edge stall. Moreover, the theory demonstrated the ability to rapidly predict dynamic stall characteristics using only static parameters as input.

Further advancements in the engineering method considered by the authors expanded its capabilities in predicting dynamic data. The constant time-lag approximation of the Kármán-Sears wake lag is found to apply to all dynamic stall occurrences, including stall during oscillations in pitch. Notably, parameters such as the moving separation point and the specific time required for the spilled vortex to reach the trailing edge, which depend on airfoil geometry, are identified based on observations.

By the late 1970s and early 1980s, researchers began investigating the effects of dynamic stall on wind turbines. Works such as (R. B. Noll & Ham, 1980), (RB & ND, 1982), (R. B. Noll & Ham, 1982), and (R. Noll et al., 1982) focused on studying the impact of dynamic stall on both vertical and horizontal wind turbines. These papers demonstrated that dynamic stall affects the loads and moments during wind turbine operation significantly.

Moreover, they highlighted the importance of considering additional loads, which can exceed static loads by a factor of 3 to 5. Neglecting these loads could result in a selected design that fails to meet specified power output and fatigue life requirements. These papers are among the pioneering works to apply knowledge of dynamic stall to the wind energy industry. As wind turbine technology continues to develop, an increasing number of studies are dedicated to exploring dynamic stall from the perspective of wind turbines.

L.W. Carr emphasizes the significant influence of dynamic stall on wind turbine performance in his paper (Carr, 1985). Carr refers to works such as (Veers, 1985) and (Laneville & Vittecoq, 1985), which demonstrate that a 30% error in predicting dynamic air loads can lead to a drastic reduction of up to 70 times in the expected lifespan of wind turbines. Additionally, Carr highlights the necessity of studying the Reynolds number effect, which posed a major challenge at the time due to the emergence of compressibility effects. He describes this issue as "an important, and presently unsolved, question."

Sufficient experimental data has allowed researchers to delve into the study of dynamic stall at a more fundamental level. In their paper (Ericsson & Reding, 1984), the authors investigate how the mode of oscillation for the airfoil determines which unsteady flow effect dominates. The main conclusions of this work are the confirmation of the linear dependence of dynamic stall overshoot on the dimensionless time rate of change of the angle of attack,  $c\dot{\alpha}/U_\infty$ .

The paper by Hibbs, B. D. (Hibbs, 1986), stands as one of the pioneering works evaluating the performance of horizontal wind turbines with dynamic stall. In this study, the author employs a modified propeller design (PROP) code to conduct the analysis. The research yields significant insights, revealing that the application of dynamic stall models has minimal impact on the performance of horizontal axis wind turbines. While most models tend to underpredict the peak power output of turbines, the discrepancy does not seem to stem from neglecting dynamic stall effects.

The study observes that dynamic stall increases cyclic loads experienced by the blades, both flapwise and edgewise. This finding underscores the importance of considering dynamic stall effects in fatigue analysis of the blades, as suggested by the author. Overall, this work contributes valuable insights into the understanding of dynamic stall's influence on horizontal wind turbine performance.

Advancements in helicopter and wind power engineering have underscored the importance of investigating previously less emphasized effects associated with dynamic stall, including compressibility, Reynolds number dependency, three-dimensional effects, and airfoil geometry. These parameters can significantly impact the loads experienced and the performance of equipment.

For instance, Miguel R. Visbal's paper (Visbal, 1990) delves into the study of dynamic stall of an airfoil pitched at a constant rate from zero incidence to a high angle of attack. By varying the free-stream Mach number, the study concludes that even at Mach numbers  $M = 0.3$  and  $M = 0.4$ , when the flow

is in the supercritical state, dynamic stall is still characterized by the formation and convection of a leading-edge vortex. At intermediate Mach numbers, noticeable compressibility effects, such as transitions between trailing-edge and leading-edge stall, are observed, along with a decrease in stall delay and maximum lift coefficient.

Similarly, the work by Lawrence W. Carr and M. S. Chandrasekhara (Carr & Chandrasekhara, 1996) represents a comprehensive investigation of compressibility effects during dynamic stall. The study establishes various facts and identifies areas requiring further research attention. Notably, it confirms the significant importance of compressibility effects at Mach numbers exceeding 0.2, observed across a wide range of Reynolds numbers. These findings highlight the complex interplay of factors influencing dynamic stall and emphasize the need for continued research in this area.

The following paper, (Spentzos et al., 2005), appears to be the first comprehensive numerical study of three-dimensional dynamic stall. The authors employ the full Navier–Stokes equations, coupled with a two-equation turbulence model. Some important conclusions are made. The most important one is that similarity between two-dimensional and three-dimensional calculations is good only in the mid-span area of the wing, whereas the outboard section is dominated by the vortex interaction.

In recent years, wind energy has gained significant traction, prompting a surge in research efforts aimed at understanding dynamic stall phenomena and its implications for wind turbine performance. By the early 21st century, a vast majority of turbines adopted a variable-speed stall-regulated control system. This approach involved adjusting rotational speed by specifying the required generator torque, thereby optimizing the extraction of aerodynamic power from the wind. Specifically, turbines are designed to stall in high wind conditions while maximizing efficiency in moderate winds (Muljadi et al., 2000).

The importance of accurate dynamic stall modeling has become increasingly apparent in the wind industry. Neglecting dynamic stall effects can lead to erroneous predictions, particularly concerning flap-wise vibrations in stall-regulated turbines. To ensure stability, it is recommended to incorporate dynamic stall models for lift calculations (M. O. L. Hansen et al., 2006).

Research by M.H. Hansen highlights the potential impact of stall-induced tower vibrations on turbine equipment lifespan. Although these vibrations may not be the primary design consideration for large active-stall-regulated turbines, they can significantly affect operational longevity. To mitigate risks, it is essential to assess airflow separation over airfoils (deep stall) and develop models for unsteady aerodynamic forces in such conditions (M. H. Hansen, 2007).

Despite advances in pitch-controlled turbine technology aimed at avoiding stall regimes, stall occurrences remain a concern. For instance, studies emphasize the importance of aerodynamic performance during yaw maneuvers, where stall effects can induce load fluctuations, particularly at the blade's inner sections. Accurate modeling of dynamic stall is crucial to understand and mitigate these effects (Ye et al., 2020).

## 2.3. Effect of parameters

The challenge in analyzing a dynamic stall is its dependence on a large number of parameters. This section briefly describes the influence of some of the parameters on the development of the dynamic stall.

### **Maximum angle of attack**

The maximum angle of attack,  $\alpha_{max}$ , determines the stall regime. At low values of this parameter, separation of the boundary layer almost does not occur, corresponding to the absence of stall. As the angle value increases, the unsteady effects in the boundary layer begin to magnify.

When a certain value is reached, the cycle enters the light stall mode. It shares some of the characteristics of static stall but also introduces hysteresis in a small part of the cycle. However, in the light stall regime  $C_l$  vs  $\alpha$  resembles the ellipses characteristic of attached flow and the oscillations in the pitching moment coefficient  $C_m$  have a small amplitude.

As the angle is further increased, the dynamic stall enters the deep stall regime. It is characterized by significant hysteresis throughout the cycle due to vortex shedding. For this reason, the lift force in the deep stall reaches significantly higher values than the static stall, followed by a subsequent sharp drop. A consequence of vortex shedding is also a strong nose-down pitching moment.

### **Airfoil geometry**

Variations in airfoil geometry, particularly thickness, camber, and leading edge sharpness, have a significant impact on boundary-layer separation, particularly in the context of the light stall regime. Different geometries are also important in determining whether the stall begins on the leading or trailing edge.

In the former case, the vortex structure begins to evolve within the first couple of percentage points along the chord, resulting in abrupt polar changes during the stall cycle. In the case of a trailing-edge stall, the boundary layer separation is initiated at the trailing edge. This results in a more gradual progression of the stall, with less negative damping and less unsteady effects (McCroskey, 1981).

### **Reduced frequency**

An increase in reduced frequency  $k$  results in a wider loop in the  $C_L$  vs  $\alpha$  curves and more significant hysteresis (*Handbook of Wind Energy Aerodynamics*, 2022). In cases where the range of angle of attack in each cycle is significant and the instantaneous value of  $\alpha(t)$  exceeds the static stall angle, an increase in the frequency value results in slower vortex detachment and flow reattachment. Further increase of the reduced frequency may even prevent the flow detachment at any point of the cycle (J. G. Leishman, 2002).

### **Mach number**

Mach number affects the dynamic stall in a similar way as the reduced frequency. With an increase in Mach number, the hysteresis loops increase. In some cases, even for low Mach numbers, occurrence of shock waves at the leading edge is possible. As the wind turbine increases in size, the possibility of local supersonic flow on the tip airfoil is discovered. Therefore, the assumption of low Mach numbers should be reconsidered for further designs (De Tavernier & Von Terzi, 2022).

# 3

## Dynamic stall modelling

Building upon the insights gained from the previous chapter, it becomes apparent that modeling unsteady aerodynamic processes is vital for optimizing designs, extending equipment lifespan, and enhancing the accuracy of energy generation predictions. However, due to the multitude of factors influencing flow field behavior during stall, its modeling presents a complex challenge. Over several decades of research on this phenomenon, numerous models of varying accuracy have been developed. These range from semi-empirical models, which rely on experimental data, to complex computational methods based on solving the Navier-Stokes equations (Spentzos et al., 2004). While a single model that fully captures all necessary processes has yet to be formulated, existing methods, when appropriately tuned, can effectively address the task with sufficient accuracy.

Given the necessity for precise and prompt results in dynamic stall modeling, semi-empirical models have gained the broadest traction. Their widespread use is attributed to their ease of application and low computational requirements. The combination of these factors sustains the interest of researchers and industry in their study and refinement.

Despite the widespread application of such models, there are numerous challenges associated with the determination of the requisite empirical coefficients for their implementation. Firstly, the utilization of experimental data obtained in a wind tunnel is inherently complex due to the presence of uncertainties and various effects that distort real measurements (refer to Chapter 4 for a detailed discussion). Secondly, model tuning is performed for a specific set of geometric parameters of the airfoil and operating conditions. This fact limits the spectrum of capabilities of tuned models and implies an individual approach and separate tuning for each new blade shape and operating condition. Additionally, when using such models, verification and validation against experimental data is a mandatory condition, which is not always readily available in the public domain and requires meticulous processing for its utilization, further complicating the process of dynamic stall modeling.

In this chapter, a description of classical versions of popular models and the principle of their application is provided in sections 3.1 - 3.5. Subsequently, a literature review of model modifications and enhancements is conducted. Finally, a brief comparison of the models is performed.

### 3.1. Beddoes-Leishman model

The Beddoes-Leishman Dynamic Stall (DS) model is a widely used model for representing the characteristics of an airfoil that undergoes a dynamic stall. Initially developed for helicopter rotorcraft, this model has been optimized for use in wind energy. It aims to provide a practical engineering method for incorporating the dynamic stall model in routine rotorcraft aerodynamics and aeroelastic response analyses. One of the significant advantages of this model is its ability to accurately reproduce the physical aspects of dynamic stall. The authors of this model divided it into four main blocks, which are described below (J. G. Leishman & Beddoes, 1989).

#### Attached Flow Behavior

One of the necessary properties of any aerodynamic model is the ability to describe the attached flow. In this model, this is achieved by superposing indicial aerodynamic responses. These functions, derived and subsequently improved, represent the sum of non-circulatory and circulatory loads.

Given the widespread use of nondimensional parameters in aerodynamics, a definition for the nondimensionalized time parameter  $S$  for each  $n$ -th step is introduced as described below, determining the relative distance covered by the airfoil in half-chords. In Equation (3.1),  $U_\infty$  stands for the free-stream velocity,  $t$  represents time, and  $c$  denotes the chord length.

$$S_n = \frac{2 \times U_\infty \times t}{c} \quad (3.1)$$

The first step in modeling attached flow is to calculate the normal circulatory force as shown in Equation (3.2):

$$C_{N_n}^C = C_{N_\alpha}(M) \times (\alpha_n - X_n - Y_n) = C_{N_\alpha}(M) \times \alpha_{E_n} \quad (3.2)$$

Here,  $C_{N_\alpha}(M)$  is the slope coefficient of the lift coefficient graph for the corresponding Mach number. The deficiency functions  $X$  and  $Y$  determine the delay in the angle of attack  $\alpha$  due to all unsteady aerodynamic effects and contain all the information about the time history of the shed wake effects on the aerodynamic loads. (J. G. Leishman & Beddoes, 1989) These functions are defined by Equations (3.3) and (3.4).

$$X_n = X_{n-1} \times e^{-b_1 \beta^2 \Delta S} + A_1 \Delta \alpha_n e^{-b_1 \beta^2 \frac{\Delta S}{2}} \quad (3.3)$$

$$Y_n = Y_{n-1} e^{-b_2 \beta^2 \Delta S} + A_2 \Delta \alpha_n e^{-b_2 \beta^2 \frac{\Delta S}{2}} \quad (3.4)$$

Here,  $\beta$  is the Prandtl-Glauert factor that accounts for the effects of compressibility at high subsonic speeds, equal to  $\sqrt{1 - M^2}$ .  $A_1$  and  $A_2$  are coefficients of the indicial response function, and  $b_1$  and  $b_2$  are exponents of the indicial response function.

Next, the calculation of the noncirculatory normal force is performed. This force, also called impulsive, has properties similar to an added-mass lift. The two components in Equation (3.5) contribute to the plunge velocity and a time decay represented by the deficiency function given by Equation (3.6).

$$C_{N_n}^I = \frac{4K_\alpha \times T_l}{M} \left( \frac{\Delta \alpha_n}{\Delta t} - D_n \right) \quad (3.5)$$

$$D_n = D_{n-1} e^{-\frac{\Delta t}{K_\alpha T_l}} + (\Delta \alpha_n - \Delta \alpha_{n-1}) e^{-\frac{\Delta t}{2K_\alpha T_l}} \quad (3.6)$$

$T_l$  is the time constant responsible for the decay of the loads due to the propagation of pressure disturbance, equal to  $c/a$ . (J. Leishman & Beddoes, 1986).  $K_\alpha$  is the factor associated with the noncirculatory

time constant, full definition is presented in original paper (J. G. Leishman & Beddoes, 1989).

To calculate the total normal force, it is necessary to sum the two components as shown in Equation (3.7).

$$C_{N_n}^p = C_{N_n}^l + C_{N_n}^c \quad (3.7)$$

### Leading Edge Separation

The next step is modeling leading edge separation. Works by Evans and Mort, as well as Beddoes, point out the high significance of critical leading edge pressure as a criterion for determining the onset of static leading edge stall. An important observation is the found relationship between pressure and normal force  $C_n$ , which implies further calculations in the  $C_n$  domain. However, for dynamic conditions, a delay is found both in  $C_n(t)$  and in pressure readings. This means that leading edge separation starts at significantly larger angles of attack for critical pressure. This phenomenon is one of the most important factors influencing the physical nature of stall delay. In their model, the author assumes that whatever properties apply to the pressure must also apply to the coefficient of normal force. To calculate the compensated normal force  $C'_{M_n}$  in unsteady conditions, Equation (3.8) introduces a first-order lag in the form of the deficiency function in Equation (3.9).

$$C'_{N_n} = C_{N_n} - D_{p_n} \quad (3.8)$$

$$D_{p_n} = D_{p_{n-1}} \times e^{\frac{\Delta S}{T_p}} + (C_{N_n}^p - C_{N_{n-1}}^p) \times e^{\frac{\Delta S}{2T_p}} \quad (3.9)$$

Here, the coefficient  $T_p$  is an important empirical coefficient, primarily dependent on the Mach number. Research has also shown that the values of this coefficient remain practically identical for different airfoil shapes (McCroskey et al., 1982).

### Trailing Edge Separation

As described in Chapter 2, the development of dynamic stall is accompanied by the movement of the separation point along the airfoil from the leading to the trailing edge. The associated loss of circulation due to trailing edge separation introduces a nonlinear force and moment behavior, especially with cambered airfoils. In the model under consideration, methods developed by Kutta describing the behavior of potential flow around a flat plate are applied. The parameter  $f$  is introduced to describe the separation point obtained from the analysis of static data. In their work, Gupta and Leishman adapt the original model to obtain values for high angles of attack.

$$C_N = C_{N_\alpha}(M) \left( \frac{1 + \sqrt{f}}{2} \right)^2 (\alpha - \alpha_0) \quad (3.10)$$

Parameter  $f$  is defined that it can take values from 1 (fully attached flow) to 0 (fully separated flow). This formulation is suitable for static conditions. In the case of unsteady conditions, to determine the effective separation point  $f'$ , it is necessary to use the corrected value of the normal force coefficient from Equation (3.8).

To obtain the instantaneous separation factor  $f''$ , it is necessary to apply one more deficiency function to account for the lag in the response of the boundary layer:

$$f''_n = f'_n - D_{f_n} \quad (3.11)$$

$$D_{f_n} = D_{f_{n-1}} e^{\frac{\Delta S}{T_f}} + (f'_n - f'_{n-1}) e^{\frac{\Delta S}{2T_f}} \quad (3.12)$$

It is important to note that the used time constant  $T_f$ , unlike other constants in Equations (3.6) and (3.9), has a strong dependence on the geometric shape of the airfoil.

The final step for calculating the coefficient of normal force for adapted nonlinear conditions is to use the modified separation point  $f''$ , as shown in Equation (3.13).

$$C_{N_n}^f = C_{N_\alpha}(M) \left( \frac{1 + \sqrt{f_n''}}{2} \right)^2 (\alpha_{E_n} - \alpha_0) + C_{N_n}^I \quad (3.13)$$

### Dynamic stall

As discussed before, significant changes in the airfoil pressure distribution, moments, and forces starts to appear only after the detachment of the vortex. This process is accompanied by an increase in lift force, which is often referred to as vortex-induced lift. This behavior is simulated in a similar way as an excess accumulation of circulation that is retained in the vicinity of the airfoil until some critical condition is reached. For a given time interval, the vortex increment  $C_{v_n}$  is defined as the difference between the instantaneous linearized value of the unsteady circulation lift force and the corresponding unsteady nonlinear lift force calculated using the Kirchhoff approximation as shown in Equations (3.14) -(3.15) (J. G. Leishman & Beddoes, 1989).

$$C_{v_n} = C_{N_n}^C (1 - K_{N_n}) \quad (3.14)$$

$$K_{N_n} = \frac{(1 + \sqrt{f_n''})^2}{4} \quad (3.15)$$

Simultaneously, the cumulative total of vortex lift  $C_N^v$  is subject to exponential decay over time, while also being susceptible to updates through additional increments. The authors again employ the same methodology as described earlier, resulting in discrete-time form as shown in (3.16).

$$C_{N_n}^v = C_{N_{n-1}}^v e^{\frac{\Delta S}{T_v}} + (C_{v_n} - C_{v_{n-1}}) e^{\frac{\Delta S}{2T_v}} \quad (3.16)$$

The pitching moment is also subject to the generation and separation of the vortex. The increment in the pitching moment  $C_M^v$  is modeled using the behavior of the center of pressure of the airfoil.

$$C_M^v = -CP_v C_N^v \quad (3.17)$$

Where  $CP_v$  is the location of the pressure center (aft of 1/4 chord), defined as:

$$CP_v = 0.2(1 - \cos(\frac{\pi \tau_v}{T_{vl}})) \quad (3.18)$$

As the generated vortex moves towards the trailing edge, the chord-wise position of the center pressure of the airfoil varies.

The equations presented above contain empirical constants, namely  $T_v$  and  $T_{vl}$ , which, respectively, represent the vortex decay time and the nondimensional time taken by the vortex to traverse the chord. Both these values are found to be relatively independent of the Mach number and airfoil shape. The value of  $\tau_v$  represents the nondimensional vortex time parameter in semi-chords. It is designed to be used in such a way that it is equal to zero at the beginning of the separation and equal to  $T_{vl}$  when the vortex reaches the trailing edge.

The final values of dynamic loads can be obtained by superposition, using Equations (3.19). The equation for the total dynamic normal force is shown here. The same principle applies to the pitching moment and chord force coefficients.

$$C_N^{dynamic} = C_N^f + C_N^v \quad (3.19)$$

### 3.1.1. Modifications review

The model discussed here has a rich developmental history, evolving into a widely applied tool for analyzing dynamic loads on airfoils. Continuous refinements, inspired by new findings and advancements, have positioned it as a valuable resource for engineers and researchers investigating the dynamic behavior of airfoils across various operational conditions.

A. Bjorck (Bjoerck, 1997) introduced enhancements to the model aimed at refining its accuracy in predicting blade vibrations during lead-lag motion, particularly in scenarios with varying relative velocities. These modifications focused on the computation of "shed wake effects" within the Beddoes-Leishman model. By transitioning the shed wake computation from being solely dependent on angle of attack history to being influenced by circulation history, the accuracy of calculations improved significantly.

In their research, K. Pierce and A. C. Hansen (Pierce & Hansen, 1995) integrated a model into YawDyn, a rotor analysis software developed at the University of Utah to analyze yaw movements and loads in horizontal axis wind turbines. Their adjustments primarily targeted angle of attack calculations to better reflect real-world wind turbine operating conditions. During their investigation, they identified discrepancies and significant loss of critical features between the tested airfoils and the model predictions, attributed to the use of exponential curve fitting for airfoil separation points. To rectify this issue, they implemented lookup tables and linear interpolation methods, resulting in a more precise reproduction of the normal force curve.

W. Sheng (Sheng et al., 2008) adapted the model for low Mach numbers. In this work, it has been demonstrated that the BL model is less applicable in reconstructing airloads below 0.12 Mach number. To ensure accuracy, several modifications have been implemented. To improve the accuracy of aircraft performance predictions, the original criterion based on the Evans-Mort correlation/shock reversal condition has been replaced with a new stall-onset criterion developed by Sheng et al. Another adjustment has been made to enhance the behavior of flow reattachments after stall regime. Previously, the initiation of the start of the return from stall process is assessed via the rise in suction at 2.5% chord (Green & Galbraith, 1994). However, the new method simply plots the incidence at which  $C_N$  is a local minimum against reduced pitch rate and extrapolates the results linearly back to the ordinate. This method ensures greater consistency with experimental data.

A significant amount of work has been devoted to using the BL model to investigate the S809 airfoil under various conditions. In a study by S. Gupta and J.G. Leishman (Gupta & Leishman, 2006), dynamic stall is analyzed for the S809 airfoil at different reduced frequencies, mean angles of attack, and amplitudes in angle of attack oscillations. The modified model used in the analysis showed good agreement with experimental data, capturing hysteresis in aerodynamic coefficients well. Yet, most of the drag coefficient is predicted accurately, there is a slight underprediction in the deep stall flow regime. Overall, the validation against experimental data showed good agreement. The model's mathematical structure makes it easy to incorporate into a wind turbine's comprehensive analysis code. The oscillations of the S809 airfoil and the fixed blade of the NREL Phase VI are researched by A. Gonzalez and X. Munduate. Despite the satisfactory results, the researchers identified the need to improve the models of the dynamic stall vortex shedding and reattachment processes due to the observed inaccuracies.

Another modification to the BL model is presented in the work of J.C.Dai, Y.P. Hu, D.S. Liu, and X. Long (Dai et al., 2011), dedicated to aerodynamic loads calculation for large-scale wind turbines. In the presented work, several modifications are introduced to the original model. First, the modifying factor  $e_0$  is included in the calculation of the chord force, which decreases the deviation between the test data and model results in the deep stall conditions. Second, when recreating pitching moment coefficient, instead of using zero lift AoA, the current AoA is utilized.

## 3.2. Snel model

Another model that is discussed is the Snel dynamic stall model. This model is created and discussed by H. Snel in (Snel, 1997). This model is originally designed for wind turbines and is used in different aeroelastic codes. One of the major advantages of the Snel method is the lack of airfoil specific coefficients.

This model is based on the work of Truong (Truong, 1993). He observed the behavior of lift coefficient in dynamic conditions and proposed the following idea. He assumed that the dynamic lift coefficient can be represented as the sum of three terms, as can be seen in (3.2). The first term is the static lift coefficient that is provided as the input in the model.

$$c_{l,dyn} = c_{l,static} + \Delta c_{l,1} + \Delta c_{l,2} \quad (3.20)$$

The second term,  $\Delta c_{l,1}$ , is the first order correction. Originally, Truong used the Beddoes-Leishman method described before to model this term. However, Snel, in his work utilizes the approach taken in the SIMPLE model (Montgomerie, 1996). In this work, the first-order correction term accounts for the forcing frequency response and is modeled as follows:

$$\tau \dot{\Delta c}_{l,1} + c f_{10} \Delta c_{l,1} = f t_1 \quad (3.21)$$

Here, the coefficient  $\tau$  is a typical time constant widely used in dynamic stall modelling that describes the time taken by the flow to travel across one semi-chord ( $\tau = \frac{c}{2U_\infty}$ , where  $c$  is the chord of the airfoil and  $U_\infty$  is the free stream velocity). The coefficient  $f t_1$  is the forcing term which represents the external forcing given to the system and is expressed as a non-dimensional derivative of  $\Delta c_{l,pot}$ :

$$f t_1 = \tau \dot{\Delta c}_{l,pot} \quad (3.22)$$

where  $\Delta c_{l,pot}$  is defined as the difference between the potential flow lift coefficient and the profile steady lift coefficient:

$$\Delta c_{l,pot} = c_{l,pot} - c_{l,static} = 2\pi \sin(\alpha - \alpha_0) - c_{l,static} \quad (3.23)$$

Going back to (3.2), coefficient  $c f_{10}$  represents the stiffness of the system that is trying to bring this term to steady state. This constant is modeled as follows:

$$c f_{10} = \begin{cases} \frac{1+0.5\Delta c_{l,pot}}{8(1+60\tau\dot{\alpha})} & \text{if } \dot{\alpha} c_{l,pot} \leq 0 \\ \frac{1+0.5\Delta c_{l,pot}}{8(1+80\tau\dot{\alpha})} & \text{if } \dot{\alpha} c_{l,pot} > 0 \end{cases} \quad (3.24)$$

Second-order correction term  $\Delta c_{l,2}$  in (3.2) relates to the higher frequencies dynamics, which should resemble an eigenfrequency of the equation. This term is modeled as the nonlinear mass-damper-spring system following:

$$\tau^2 \ddot{\Delta c}_{l,2} + c f_{21} \dot{\Delta c}_{l,2} + c f_{20} \Delta c_{l,2} = f t_2 \quad (3.25)$$

The coefficients  $c f_{20}$  is determined as shown below:

$$c f_{20} = k_s^2 (1 + 3(\Delta c_{l,2})^2 (1 + 3\dot{\alpha}^2)) \quad (3.26)$$

Coefficient  $c f_{21}$  is taking different values based on the upstroke or downstroke motion of the airfoil and is determined as follows:

$$c f_{21} = \begin{cases} 60\tau k_s (-0.01(\Delta c_{l,pot} - 0.5) + 2(\Delta c_{l,2})^2) & \text{if } \dot{\alpha} c_{l,pot} > 0 \\ 2\tau k_s & \text{if } \dot{\alpha} c_{l,pot} \leq 0 \end{cases} \quad (3.27)$$

In this system, the coefficient  $k_s$  is the reduced frequency of the vortex shedding in a uniform flow, or Strouhal frequency, which is equal to 0.2

Finally, the forcing term for the second-order correction,  $ft_2$  can be calculated as:

$$ft_2 = 0.12(-0.15 \times \Delta c_{l,pot} + 0.05 \Delta \dot{c}_{l,pot}) \quad (3.28)$$

### 3.2.1. Snel model modifications review

The model described above is initially introduced in 1997, and since then, researchers have continuously explored ways to enhance its accuracy and applicability. However, compared to the Beddoes-Leishman model, modifications to the Snel model have received relatively less attention in the literature.

In a notable study by Adema and Snel (Adema et al., 2020), the authors undertook significant enhancements to the second-order Snel model, integrating it into the turbine design software Bladed. Their work encompassed several key modifications. Firstly, a dimensional analysis is conducted, introducing a time constant to render parameters such as chord length, wind speed, and pitching frequency dimensionless. This adjustment facilitates more versatile application across varying scenarios.

Furthermore, the authors replaced the previous empirical value of  $2\pi$  with the true value of the lift coefficient slope. This slope, calculated between the intercepts at angles of attack  $\alpha = 0^\circ$  and lift coefficient  $C_L = 0$ , offers a more accurate representation of aerodynamic behavior.

An important refinement involved substituting the lift coefficient  $CL$  with the normal force coefficient  $C_N$ . This change is motivated by the observation that the lift coefficient tends toward zero at high angles of attack, even as unsteady vortex shedding persists. Thus, modeling vortex shedding in relation to the normal force on the airfoil provides a more realistic depiction of the aerodynamic phenomena.

Moreover, improvements are made to the modeling of downstroke motion and vortex shedding. These enhancements aim to capture the intricacies of aerodynamic behavior more effectively.

Lastly, the constants within the model are optimized to better align with experimental data, ensuring greater fidelity in predictive capabilities. These modifications collectively represent significant advancements in the Snel model, enhancing its utility and accuracy for turbine design and analysis.

This modification of the model is used in the present work due to its simplicity and encouraging results.

# 4

## Experimental methodology

Obtaining accurate and reliable experimental data is an integral part on the way towards the improvement of aerodynamic modeling. In this context, the utilization of wind tunnels, namely the Low-speed Low Turbulence (LLT) wind tunnel located at TU Delft, is an invaluable instrument that provides controlled conditions for a detailed study of the aerodynamic phenomena under consideration. This chapter is devoted to describing the process of obtaining and processing the data obtained during the conducted experiment.

The goal of any mathematical model is to reproduce real-world phenomena with high accuracy. As described earlier, the vast majority of models for dynamic stall are semi-empirical, which means that experimental data must be available. Although some models allow the use of simplified methods such as "mean airfoil" or "flat plate", the availability of real experimental data allows for the model optimisation for the accurate performance. Validation of mathematical models is a vital step towards increasing their accuracy and reliability. It bridges the gap between theoretical assumptions and practical applications, ensuring that models can reproduce reality. Comparing model predictions with experimental results helps to ensure the stability of the model and helps test its predictive capabilities.

This chapter is divided into sections as follows. Section 4.1 describes the parameters and capabilities of the facility in which the experiment is conducted. Section 4.2 focuses on describing the experimental data collection methods and their features. Next, Section 4.3 deals with the experimental model. Section 4.4 focuses on the corrections that need to be applied to the data obtained. Finally, Section 4.5 describes and analyze the results of the experiment.

## 4.1. Facility

The experiment is undertaken in a low-speed, LTT at the Delft University of Technology. A 708 kW DC motor drives this recirculating wind tunnel, powering a six-bladed fan. The octagonal test section measures 1.80 by 1.25 by 2.60 m. The maximum flow velocity is  $u_\infty = 120 \text{ m s}^{-1}$ . For testing two-dimensional airfoils, the maximum chord-based Reynolds number is  $Re = 3.5 \times 10^6$ . The wind tunnel design is capable of low turbulence levels due to the high contraction factor of 17.8 between the settling chamber and the test section. The turbulence intensity in the test section ranges from 0.015% at 20 m/s up to 0.07% at 75 m/s. The technical drawing of the general view is shown in the Figure 4.1.

### *The Low Speed, Low Turbulence Wind Tunnel.*

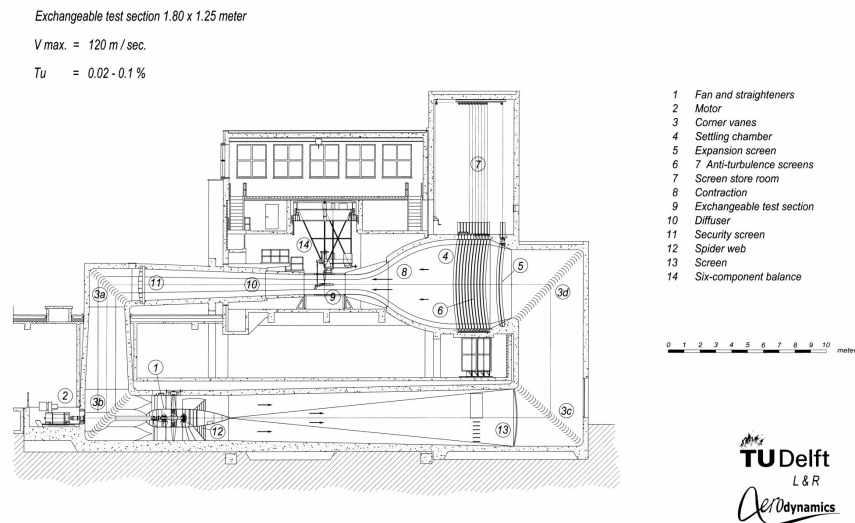


**Figure 4.1:** The Low Speed, Low Turbulent Wind Tunnel

1 - Fan and straighteners, 2 - Motor, 3 (a-d) - corner veins, 4 - Settling chamber, 5 - Expansion screen, 6 - 7 Anti-Turbulent screens, 7 - Screen store room, 8 - Contraction, 9 - Exchangeable test section, 10 - Diffuser, 11 - Security screen, 12 - spider web, 13 - Screen, 14 - 6 component balance

## 4.2. Experimental methods

Conducting an experiment is a crucial aspect of any successful project, and the accuracy of data measurements significantly influences the results' quality. This section outlines the methods and equipment employed for collecting measurements.

The primary goal of the current experiment is to acquire static and dynamic polars of the analyzed airfoil for subsequent use in model assessment and tailoring. The equipment used for data collection falls into three main categories: pressure measurement, thermal imaging, wake measurement.

### 4.2.1. Pressure taps

In wind tunnel experiments, surface pressure distribution on two-dimensional airfoil sections is commonly measured using pressure taps. These taps, located either on the tunnel walls or directly on the airfoil model, provide data that can be integrated to calculate lift force. In our study, pressure taps are positioned on the airfoil model itself. A total of 93 taps, each with a 0.3 mm diameter hole, are drilled on the airfoil's pressure and suction sides. To enhance the representation of suction peak, a local refinement is implemented at the leading edge. Although the original model design included a trailing edge orifice, data collection is hindered by malfunctioning equipment.

### 4.2.2. Thermal imaging

Two thermal cameras are installed to capture both sides of the model. To improve thermal imaging, the wind tunnel is equipped with heat lamps to provide flow heating. Infrared imaging serves several purposes. First, it allows to confirm the two-dimensional behavior of the flow. Secondly, this method allows for the high-accuracy detection of defects or dust particles on the model surface, which may impact the behavior of the boundary layer. Finally, observing changes in the boundary layer, such as laminar to turbulent regime change or flow separation, is possible with this method. On Figure 4.2 images from thermal cameras are presented for the clean airfoil at  $Re = 2 \times 10^6$  and  $\alpha_0 = 0^\circ$ . The sharp change from light to dark areas makes it easy to distinguish the transition from laminar to turbulent flow.

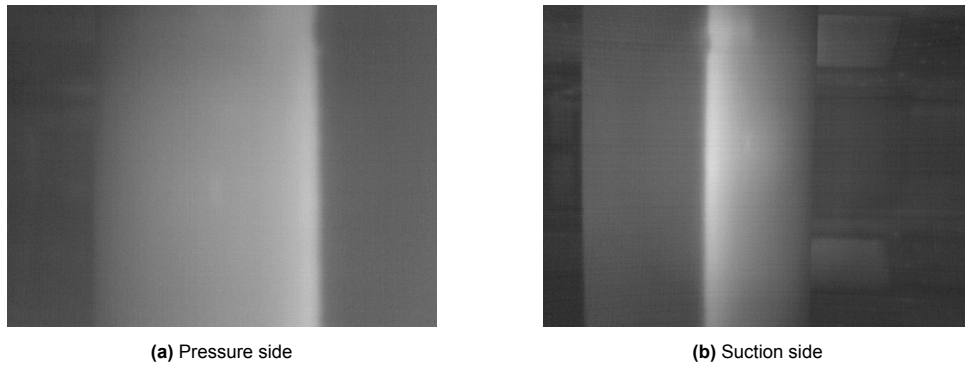


**Figure 4.2:** Thermal images of pressure and suction side.  $Re = 2 \times 10^6$ ,  $\alpha_0 = 0^\circ$

### 4.2.3. Wake measurements

The wake rake (Figure 4.6) is a tool used for measuring the aerodynamic drag of objects in a stream, with a long-standing history of practical application (Terra et al., 2018), (Timmer, 2008). A common method to measure resistance forces involves using a Pitot-tube rake to analyze the pressure field in the object's wake. This approach applies the conservation of momentum principle to a defined control volume encompassing the object. It is frequently employed to estimate the aerodynamic drag of stationary airfoils or three-dimensional models. Beyond assessing the drag force, the wake rake also offers insights into the velocity distribution behind the model, aiding in understanding the wake flow structure and associated aerodynamic loads.

During the experiment, the wake rake is utilized to estimate the momentum loss in the wake. The estimation is based on the collection of static data from 67 pressure tubes and 16 static tubes, which are placed over a total length of  $504mm$ . The wake is installed on the two-degree-of-freedom traverse, allowing it to collect data across the entire model span. However, at some angle of attack, the wake becomes too wide to be captured by the wake rake. Therefore, drag forces are calculated using pressure taps on the model.

### 4.2.4. Positioning of the model

The model's position plays a crucial role in obtaining accurate data. The angle of attack is the most important parameter in the calculations, and hence, it is necessary to ensure the correct position of the model. In this experiment, a turntable is used to change the angle of attack for static data collection, that can be seen on Figure 4.6. However, for dynamic tests, it is necessary to use a linear actuator to accurately control the angle of attack and oscillation frequency since it involves motions beyond the turntable's capabilities.

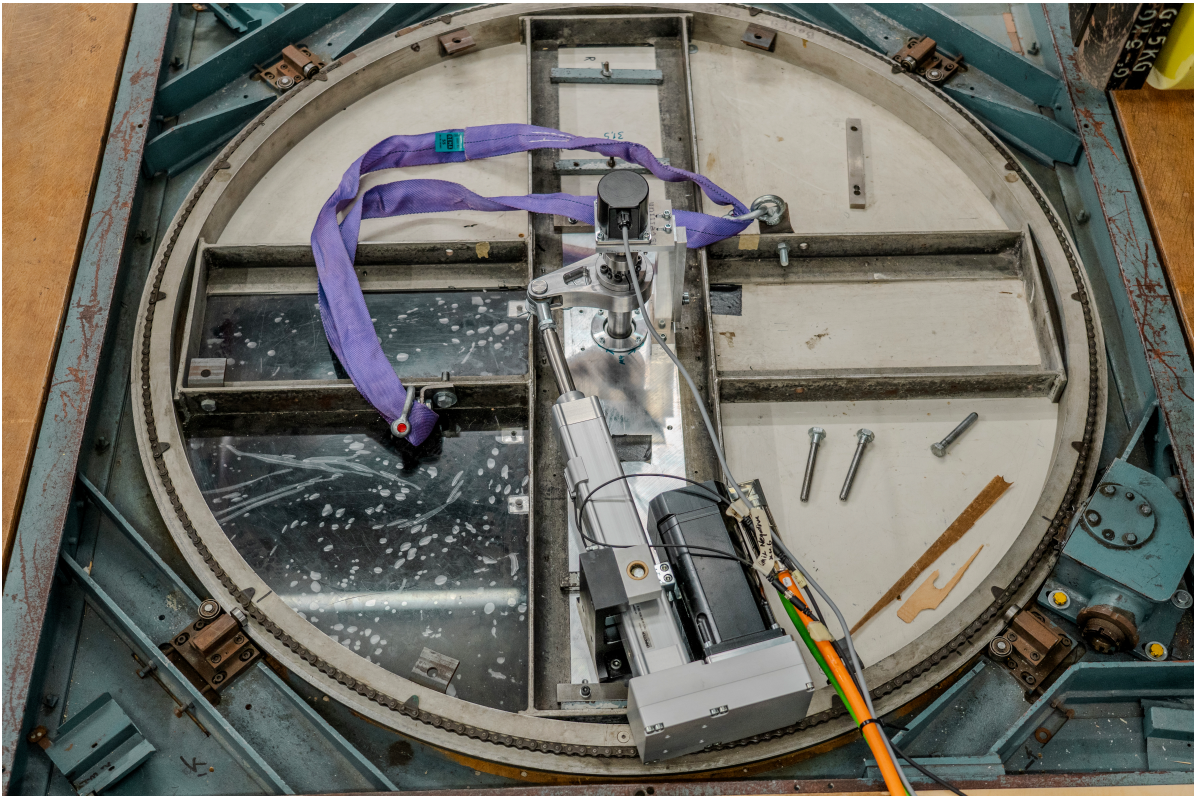


Figure 4.3: Linear actuator

### 4.3. Wind tunnel model

The model in question is one of the FFA-W3 family of airfoils shown on the Figure 4.5, namely FFA-W3-211. This airfoil was designed by FFA (The Aeronautical Research Institute of Sweden) (Bertagnolio et al., 2001).

An FFA-W3-211 airfoil model is manufactured from a carbon fiber-based composite material Figure 4.6. The maximum airfoil thickness is 21.1% of the chord length, shown in Figure 4.5. The airfoil has a chord length  $c = 600\text{mm}$  and height  $h = 1246\text{mm}$ , which allows it to span the height of the LTT test section. The surface of the model is polished to remove any manufacturing impurities. Throughout the experiment, the surface of the airfoil is constantly cleaned with paper towels soaked in alcohol to prevent any flow transition caused by dust particles and impurities.

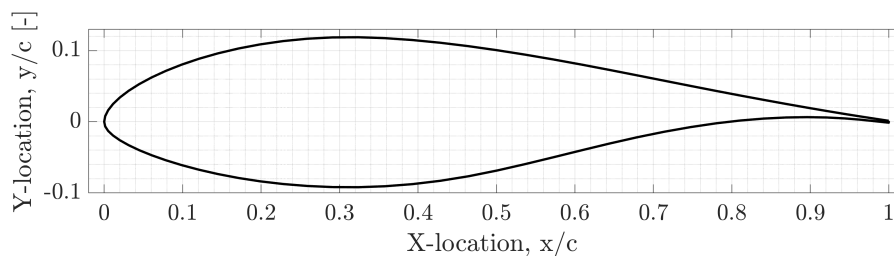
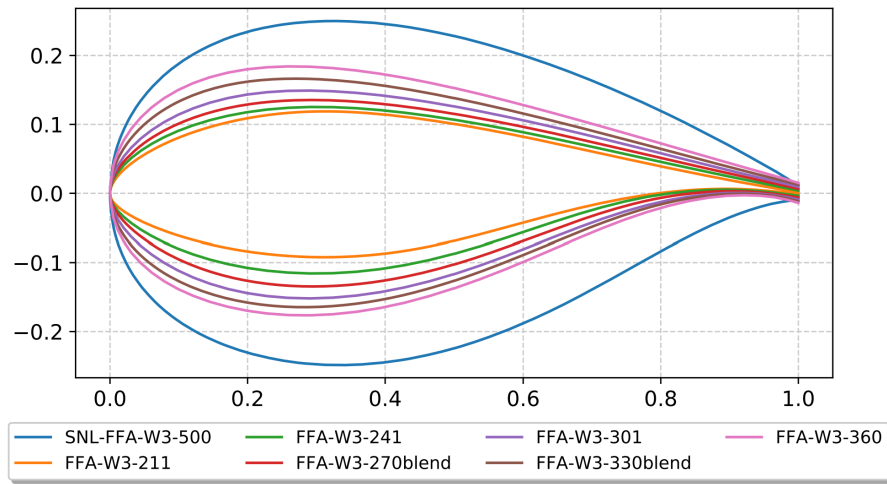
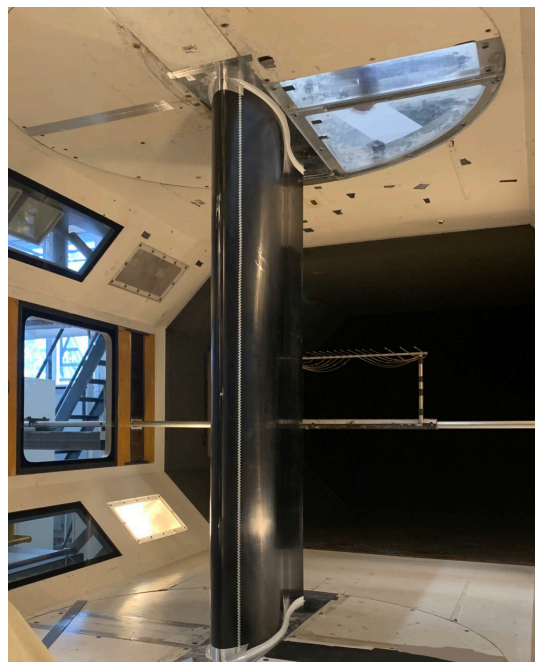


Figure 4.4: DTU FFA-W3-211 airfoil coordinates



**Figure 4.5:** FFA-W3 airfoil family used in the IEA Wind 15-MW blade design

The airfoil has a variable thickness of about  $3\text{mm}$ , with additional reinforcement along the leading edge. In contrast, the trailing edge thickness is  $1.7\text{mm}$ . To fix the airfoil in the wind tunnel, an aluminum shaft connects two flat plates with ribs on both sides of the model.



**Figure 4.6:** Setup for static measurements. Gaps between the upper and lower boundaries are taped. Turntable and wake rake can be observed

Selecting the geometry and size of a model is a complex process that depends on various factors. The main aim of the research is to test the model profile at maximum possible values of Reynolds number. An increase in this number means an increase in flow velocity, lift, and aerodynamic drag. However, the wind tunnel design, particularly the main bearing and testing section size, limits the loads and model size. As a result, compromises must be made while working with such a complex, interconnected system. In this case, the final configuration is a balance between the capabilities of the experimental facility itself, blockage effects, and free flow velocity.

A chord length of  $0.6\text{m}$  is selected to allow for a pitching oscillation range of  $-20^\circ$  to  $20^\circ$ . By filling the



**Figure 4.7:** Tubes exiting the model for measuring pressure distribution

entire height of the testing section, we can assume a 2D wing theory. These parameters ensure that the blockage effect does not exceed the maximum acceptable value. of 15% at  $Re = 3.5 \times 10^6$ .

## 4.4. Corrections

This section will briefly discuss corrections that are applied to the obtained wind tunnel data. A detailed description of the equations is given in (Timmer, 2014).

### **Streamline curvature**

The first important correction applied relates to the streamline curvature. When a fluid flows around an object, the streamlines curve due to the object's shape and other factors influencing the behavior of the flow. Curvature degree of the streamlines plays a significant role in determining airfoil polars.

In wind tunnels, the flow is constrained, which results in unwanted flow interactions. The normal curvature of the free air flow about a model is straightened by the tunnel walls. This results in the artificial increase of the camber as well as pressure gradients compared to unconstrained value. Ultimately, this virtually increases the angle of attack, leading to higher lift and quarter chord moments.

**Wake blockage**

The test section walls affect the smooth development of backward vortices that extend several diameters behind the wind turbine, causing the wake blockage effect. The wake size is directly related to the resistance that counteracts the wind turbine to the flow of air, i.e., to the energy taken from the air stream (Bešlagić et al., 2020). The formed wake has a lower velocity and thus a higher pressure than the free stream. To satisfy the flow continuity, the velocity of the air outside the wake must be greater than the free stream velocity, causing pressure differences along the model that affect the drag and lift as a consequence (Shyu & Chuang, 2008).

**Solid blockage**

The presence of a model within the constraints of the test section reduces the effective area of flow around it. This decrease in the area increases the velocity of the air as it flows over the model and thus decreases the pressure around the model. Moving further down the tunnel, the solid blockage decreases, and the flow velocity returns to its initial value. The solid blockage is directly related to the ratio between the wind turbine model projection surface and the cross-sectional area of the wind tunnel test section perpendicular to the airflow direction causing pressure gradients that must be corrected.

## 4.5. Experimental matrices

This section will primarily delve into the outcomes derived from the conducted experiment. Initially, it will encapsulate a summary of the static experiment results, followed by the presentation of findings from the dynamic section. A detailed account of the relationship between the normal force coefficient  $C_N$  and the angle of attack  $\alpha$  will be provided. Furthermore, the observed hysteresis will be analysed concerning various parameters. Lastly, graphical representations of the pressure coefficient  $CP$  vs relative x coordinate of the model  $x/c$  will be presented.

### 4.5.1. Static polars

To verify the obtained values, the  $Cl$  vs  $Cd$  plot is created and compared to the RFOIL and Wind Turbine Airfoil Catalogue (Bertagnolio et al., 2001). The data is depicted on Figure 4.8.

The static polars, namely the lift coefficient  $C_P$  versus angle of attack and the lift coefficient versus drag coefficient  $C_D$ , are shown in Figure 4.9. The Figure 4.9a clearly depicts a distinct dependence of the lift coefficient on the Reynolds number. The linear region extending from  $\alpha = -8^\circ$  to  $\alpha = 11.3^\circ$  shows an increased slope with increasing Reynolds number. Notably, the post-stall behavior also depends on the Reynolds number, with the  $\alpha$  onset for  $Re = 5 \times 10^5$ ,  $7.5 \times 10^5$ , and  $1 \times 10^6$  greater than for other values of  $Re$ . Considering this, a threshold at  $Re = 1.5 \times 10^6$  beyond which the stall angle remains constant is determined.

Another distinct difference is how abrupt the stall is. Lift before the defined threshold value experiences a more gradual decline after stall when the below-threshold lift seems to drop significantly in a much shorter time period.

Similar behavior is observed in Figure 4.9b, where the three highest values of  $Re$  yield higher drag coefficients compared to the other curves.

### 4.5.2. Dynamic polars

Dynamic polars presented in this section are obtained by averaging the measured pressure distribution over multiple cycles. The airfoil is following a sinusoidal motion, defined in (4.1). In total, 180 cases were measured. The selected parameters are similar to those presented in (Chellini et al., 2023) and summarised in Table 4.1.

$$\alpha(t) = \alpha_0 + A * \sin(2\pi ft) \quad (4.1)$$

Where  $\alpha_0$  is the mean angle of attack,  $A$  is the amplitude and  $f$  is the desired oscillating fre-

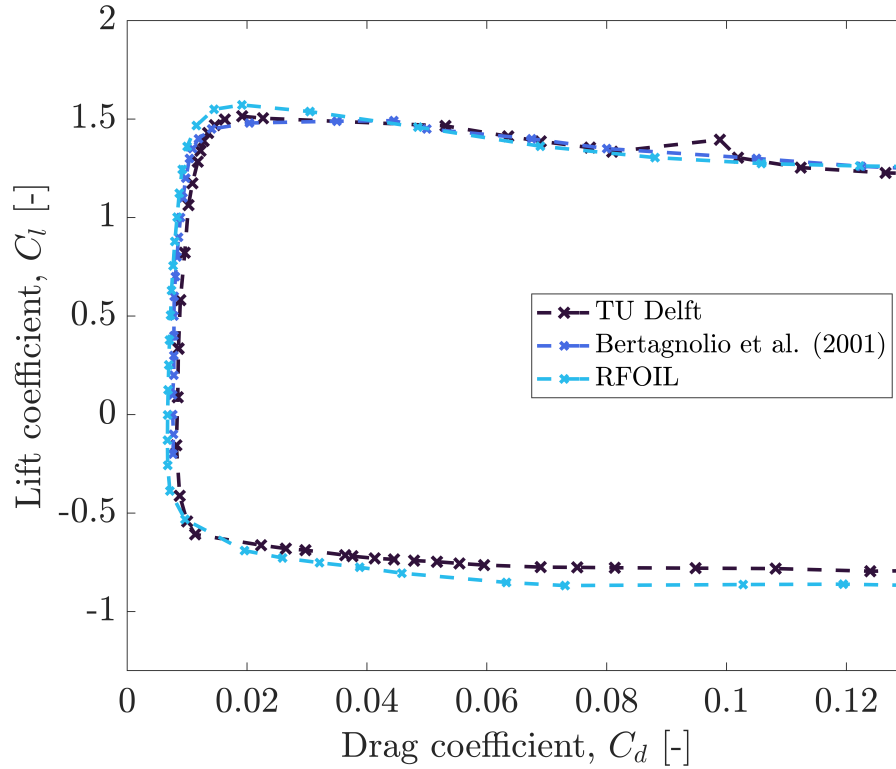


Figure 4.8:  $C_l$  vs  $C_d$  comparison for static polars

quency. The same oscillating frequency term is also found in the reduced frequency, which is defined in (4.2).

$$k = \frac{\pi f c}{U_\infty} \quad (4.2)$$

Cases with a mean angle of attack ( $\alpha_0 = 0^\circ$ ) hold limited interest in this study, as the dynamic stall region is either not reached or is in its initial stages, lacking representativeness. Consequently, these graphs are relocated to the appendix for a more comprehensive documentation.

Parameter	Values				
$Re, [-]$	$5 \times 10^5$	$1 \times 10^6$	$2 \times 10^6$		
$A, [\text{deg}]$	3	5	7	9	11
$f, [\text{Hz}]$	0.6	1.2	1.8	2.4	
$k, [-]$	0.046	0.091	0.137	0.182	
$\alpha_0, [\text{deg}]$	-8	0	11		

Table 4.1: Set of parameters for the dynamic part of the experiment

### Frequency dependency at positive angles

In instances of positive angle of attack stalls, a comparable pattern emerges. Elevated reduced frequencies lead to heightened overshoot in normal coefficient and a prolonged delay in boundary layer reattachment. For Reynolds numbers  $Re = 1 \times 10^6$  and  $Re = 2 \times 10^6$ , hysteresis amplification becomes more noticeable as the frequency value increases. Figures for  $Re = 5 \times 10^5$  and  $Re = 1 \times 10^6$  are presented in Appendix A.

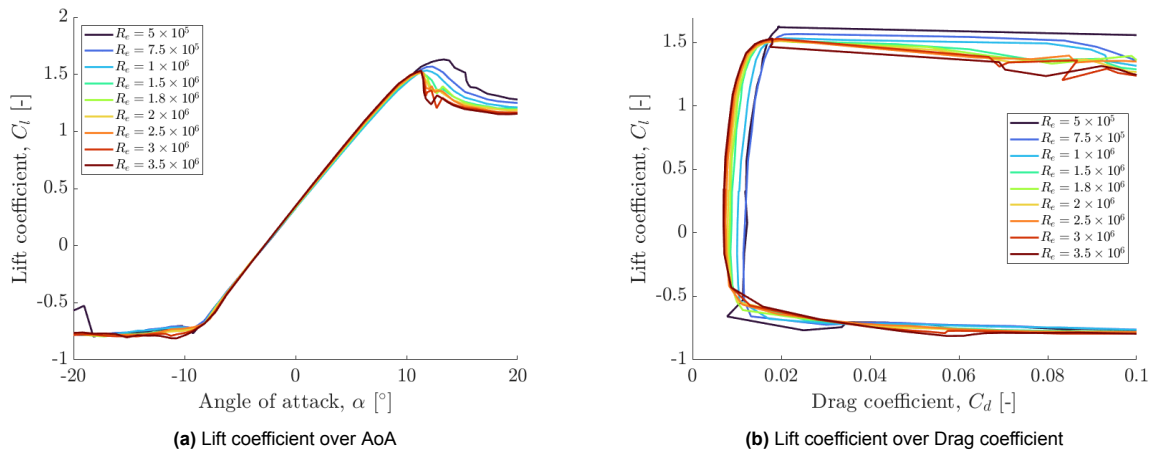


Figure 4.9: Steady polars

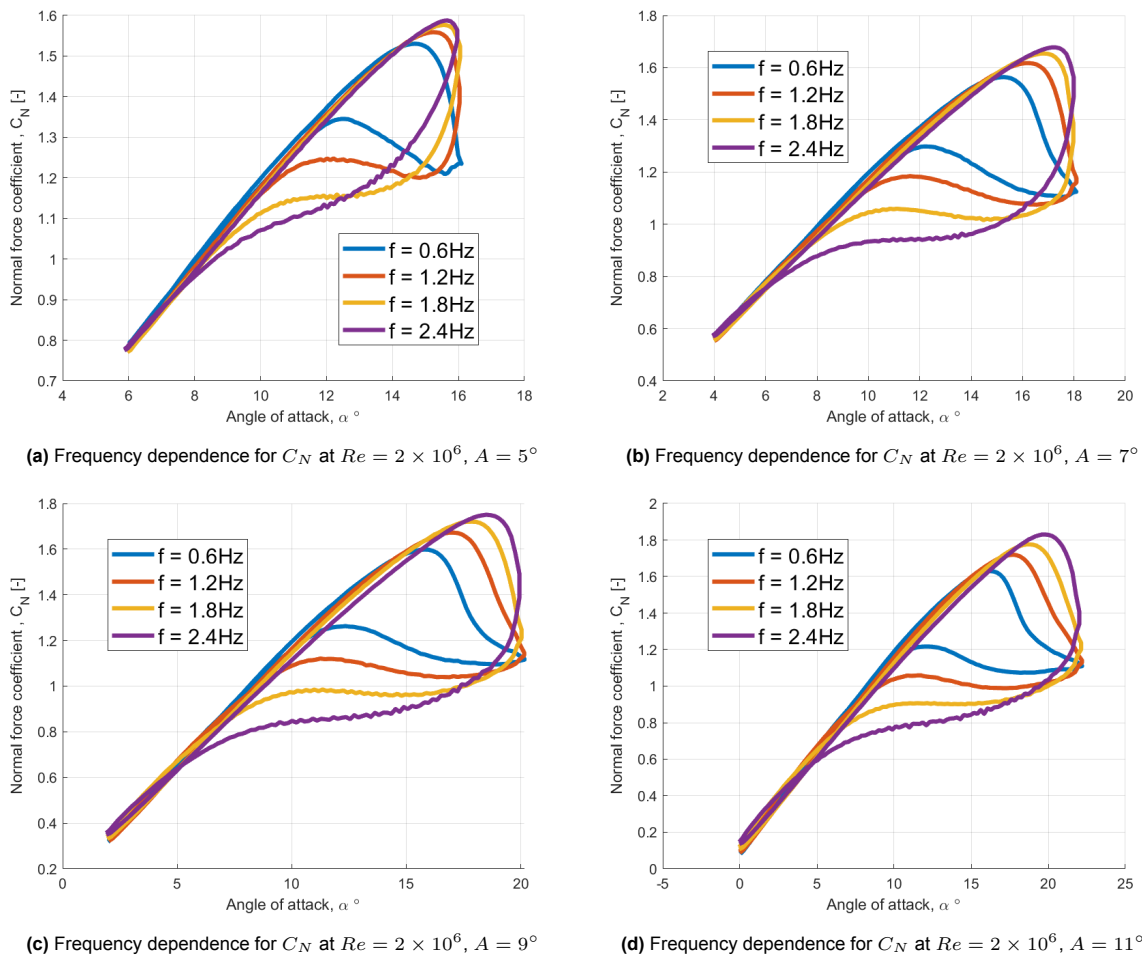
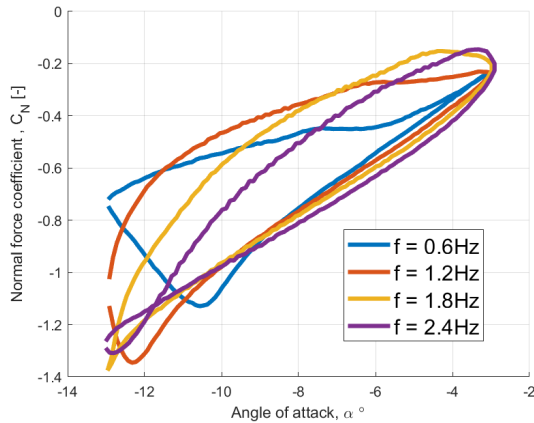


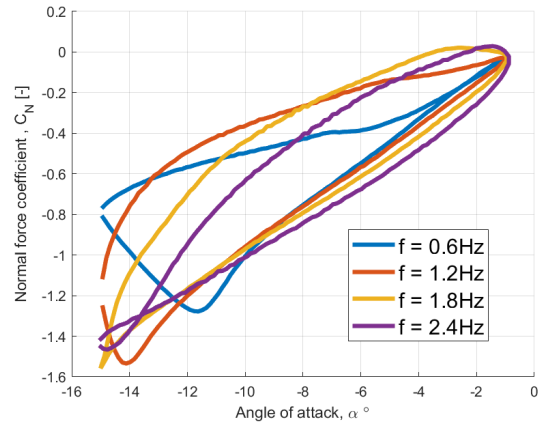
Figure 4.10: Dynamic normal coefficient frequency dependence for various amplitudes at  $Re = 2 \times 10^6$ ,  $\alpha_0 = 11^\circ$

### Frequency dependency at negative AoA

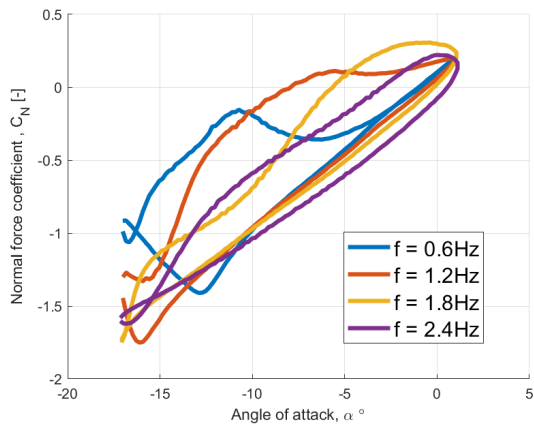
The analysis begins by examining the frequency changes at different Reynolds numbers, amplitudes, and mean angles. Figure 4.11 shows the normal coefficient as a function of angle of attack for four different amplitude cases:  $A = 5^\circ, 7^\circ, 9^\circ$  and  $11^\circ$  degrees, at a  $Re = 5 \times 10^5$ . Notably, the  $f = 0.6Hz$  cases show significant differences from the other frequency values. The angle of attack of the dynamic stall for these cases occurs earlier, resulting in faster detachment of the vortex from the trailing edge and a pronounced increase in  $C_N$  values before the upstroke motion. This also leads to the lower slope values at the linear region.



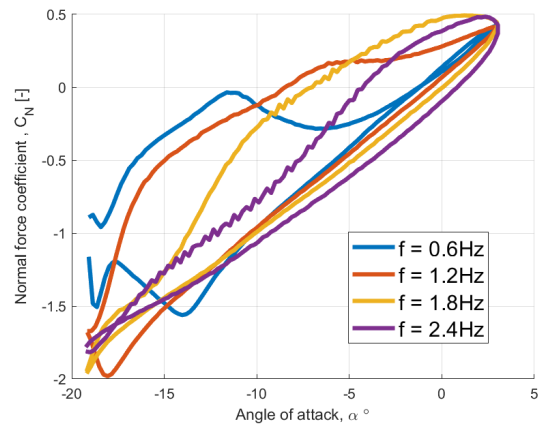
(a) Frequency dependence for  $C_N$  at  $Re = 5 \times 10^5$ ,  $A = 5^\circ$



(b) Frequency dependence for  $C_N$  at  $Re = 5 \times 10^5$ ,  $A = 7^\circ$



(c) Frequency dependence for  $C_N$  at  $Re = 5 \times 10^5$ ,  $A = 9^\circ$



(d) Frequency dependence for  $C_N$  at  $Re = 5 \times 10^5$ ,  $A = 11^\circ$

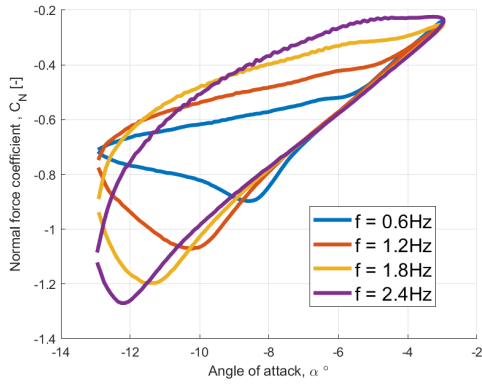
**Figure 4.11:** Dynamic normal coefficient frequency dependence at  $Re = 5 \times 10^5$ ,  $\alpha_0 = -8^\circ$

Another remarkable observation relates to the reattachment region for the  $f = 1.2Hz$ . The  $C_N$  values experience a decline before reaching the maximum angle of attack, resulting in lower values compared to the  $f = 1.8Hz$  and  $f = 2.4Hz$  curves. This particular behavior can result from the complex unsteady boundary layer reattachment behavior, which depends on both the Reynolds number and the reduced frequency.

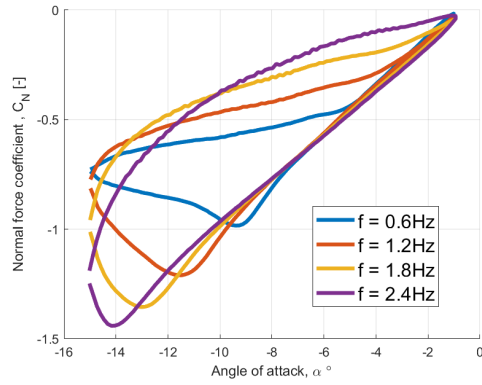
Continuing the exploration of frequency dependence, the cases for  $Re = 1 \times 10^6$  and  $2 \times 10^6$  are considered, as depicted in Figure 4.12 and Figure 4.13 respectively. An observable trend emerges with increasing Reynolds number, where the boundary layer reattachment process becomes smoother. In Figure A.2b, for instance, at  $Re = 1 \times 10^6$  and  $A = 5^\circ$ , it becomes apparent that for frequency values

of  $f = 0.6Hz$  and  $f = 1.2Hz$ , the boundary layer reattaches by the end of the cycle.

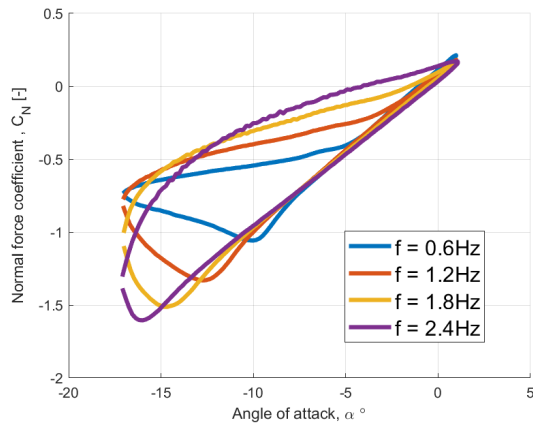
Comparing this with the  $Re = 2 \times 10^6$  case, it is apparent that the frequency influences the level of unsteadiness of the boundary layer since its reattachment initiates at lower values of AoA, as illustrated in Figure 4.13. Furthermore, a consistent pattern emerges regarding the impact of frequency on the stall force. As frequency increases, both the angle at which vortex detachment from the trailing edge occurs and the minimum value of the normal force coefficient elevate. This results in a broadening of the hysteresis loop and an extended time for the reattachment of the boundary layer.



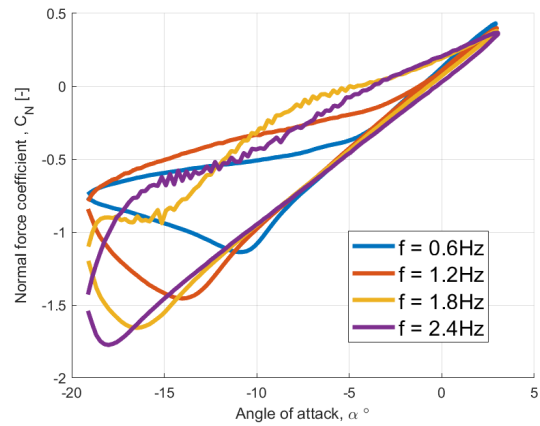
(a) Frequency dependence for  $C_N$  at  $Re = 1 \times 10^6$ ,  $A = 5^\circ$



(b) Frequency dependence for  $C_N$  at  $Re = 1 \times 10^6$ ,  $A = 7^\circ$

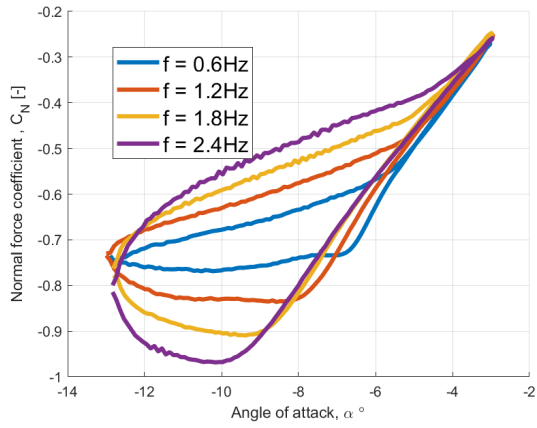


(c) Frequency dependence for  $C_N$  at  $Re = 1 \times 10^6$ ,  $A = 9^\circ$

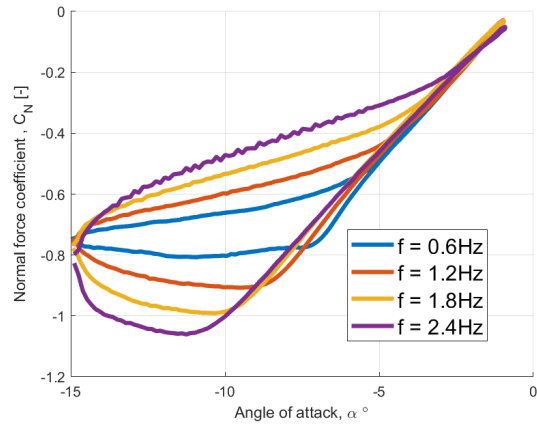


(d) Frequency dependence for  $C_N$  at  $Re = 1 \times 10^6$ ,  $A = 11^\circ$

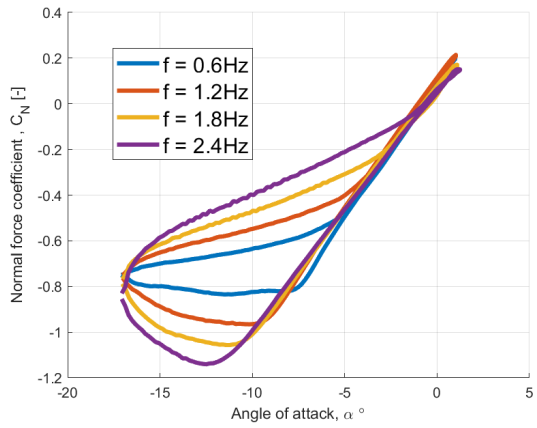
**Figure 4.12:** Dynamic normal coefficient frequency dependence for various amplitudes at  $Re = 1 \times 10^6$ ,  $\alpha_0 = -8^\circ$



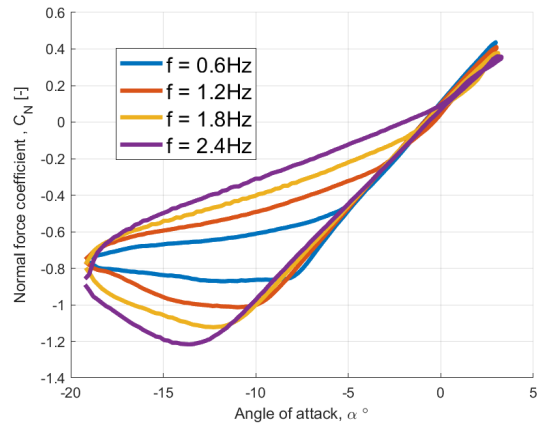
(a) Frequency dependence for  $C_N$  at  $Re = 2 \times 10^6$ ,  $A = 5^\circ$



(b) Frequency dependence for  $C_N$  at  $Re = 2 \times 10^6$ ,  $A = 7^\circ$



(c) Frequency dependence for  $C_N$  at  $Re = 2 \times 10^6$ ,  $A = 9^\circ$



(d) Frequency dependence for  $C_N$  at  $Re = 2 \times 10^6$ ,  $A = 11^\circ$

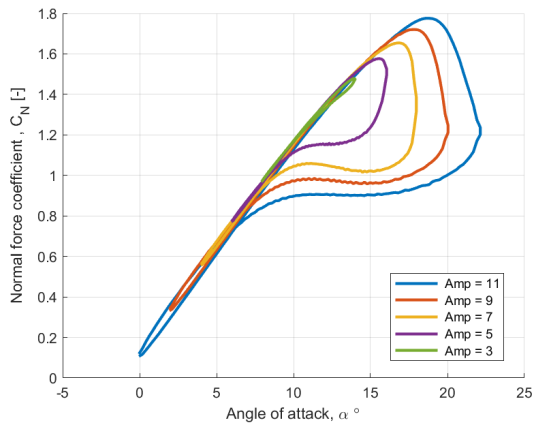
**Figure 4.13:** Dynamic normal coefficient frequency dependence for various amplitudes at  $Re = 2 \times 10^6$ ,  $\alpha_0 = -8^\circ$

### Amplitude dependency

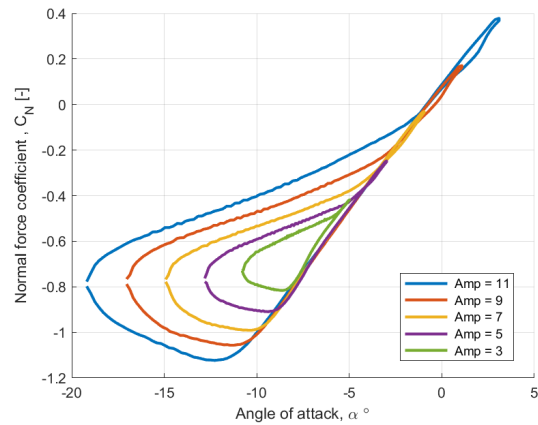
In examining the relationship between the normal force coefficient and amplitude, consistent findings emerged across all cases. For clarity, this section highlights two cases at  $Re = 2 \times 10^6$ ,  $f = 1.8Hz$ , with mean angles of  $\alpha_0 = 11^\circ$  and  $\alpha_0 = -8^\circ$ . Additional cases are detailed in Appendix A and Appendix B. The observed patterns, as the amplitude increases from  $A = 3^\circ$  to  $A = 11^\circ$ , are as follows:

- Augmentation in the maximum normal coefficient value.
- Widening of the hysteresis loop
- Prolonged delay in the reattachment of the boundary layer.

These trends provide valuable insights into the impact of amplitude variations on aerodynamic characteristics.



(a) Amplitude dependence for  $C_N$ ,  $f = 1.8Hz$ ,  $\alpha_0 = 11^\circ$



(b) Amplitude dependence for  $C_N$  at  $f = 1.8Hz$ ,  $\alpha_0 = -8^\circ$

**Figure 4.14:** Dynamic normal coefficient amplitude dependence at  $Re = 2 \times 10^6$

# 5

## Beddoes-Leishman model optimization results

A notable aspect of this thesis is its focus on optimizing shape constants, a feature often overlooked in other studies where these constants remain unchanged. The significance of this optimization lies in its demonstrated impact on model results, particularly in relation to the airfoil geometry. It's highlighted that these shape constants exhibit considerable influence and are heavily dependent on the specific characteristics of the airfoil.

The original values of the four shape parameters are derived for airfoils typically utilized in the wind turbine industry, which tend to have higher thicknesses and cambers. However, it's concluded that these coefficients are not directly applicable to the airfoil shape under consideration due to its distinct characteristics.

The chapter is structured as follows. section 5.1 explains the selection of optimization variables and the methodology employed. Next, in an effort to streamline the optimization process and minimise the number of variables, section 5.2 introduces a data-driven approach to determine  $T_p$  coefficients, thereby excluding it from the optimization. Followed by section 5.3, which describes the parameters used to conduct a quantitative comparison between the optimized model and the standard model. Finally, section 5.4 presents the comparative analysis of model parameters and offers insights into the implications of the optimization results.

### 5.1. Optimization

The Beddoes-Leishman model, as mentioned previously, is a semi-empirical model that relies on a set of eight empirical coefficients. These parameters consist of four-time delays characterising the airfoil's aerodynamics, denoted as  $T_p$ ,  $T_f$ ,  $T_v$ , and  $T_{vl}$ . Four shape-based coefficients characterise the geometry or hysteresis loop shape, typically found in the literature as  $A1$ ,  $A2$ ,  $b1$ , and  $b2$ .

Typically, shape based coefficients are not optimized and take values the same as they are proposed by Beddoes (Beddoes, 1982). However, these coefficients are dependent on airfoil shape, as shown in (Singapore Wala et al., 2018). Therefore, this study aims to consider this fact and optimize both time-based and shape-base coefficients to increase the model reliability for the airfoil in question.

The optimization process is conducted separately for each case of amplitude and reduced frequency, considering different Reynolds numbers. This approach is necessary due to significant variations in stall onset, hysteresis loop shape and size, and other parameters discussed below at different Reynolds numbers.

Subsequently, the optimization results for each case at a single Reynolds number are averaged to obtain a set of coefficients for a specific Reynolds number. This methodology enhances the robustness of the model and enables the utilization of a fixed set of values without requiring individual optimization for each specific airfoil. This approach is proven to give positive results in Singapore Wala et al., 2018.

The optimization of the BL model is carried out using the linear least square minimisation objective function as shown in (5.1), where  $E$  and  $M$  are Experimental data and Model output, respectively. Processed data is normalised over the maximum or minimum  $C_N$  values based on positive or negative mean AoA oscillation to better visualise the overlap.

$$Obj = \min \sum (E - M)^2 \quad (5.1)$$

The obtained values of the semi-empirical coefficients for the examined cases are summarized in Table 5.1. Notably, there's a significant deviation from the default values, particularly in the  $T_p$  and  $T_f$  coefficients. These deviations profoundly influence various aspects of the hysteresis loop. Increasing  $T_p$ , for instance, delays the boundary layer reattachment, leading to a broader hysteresis loop and a higher stall onset AoA. Conversely, the impact of the  $T_v$  is relatively minor, affecting the stall AoA marginally while preserving the reattachment area.

Interestingly, the optimization of shape-based parameters, although less explored in the literature, proved to be highly beneficial. Elevating the  $A1$  and  $A2$  parameters increases the  $C_N$  slope, while the  $b1$  and  $b2$  coefficients exhibit an opposite trend, decreasing the slope with higher values. These adjustments notably affect the reattachment area, particularly during the downstroke motion. The default values of the BL model allow  $C_N$  to exceed the linear region, influencing the slope and resulting in secondary hysteresis loops at lower AoA values. This effect is more pronounced at higher frequencies, where complete flow reattachment may not occur by the cycle's end. Precise optimization of the shape parameters can significantly enhance the model's ability to predict reattachment values and improve overall performance.

## 5.2. $T_p$ coefficient determination

Johan Boutet's work presents a method to reduce the number of optimisation parameters by establishing a relationship between the dynamic angle of attack onset and the reduced pitch, determining the time-lag coefficient  $T_p$  (Boutet et al., 2020). For the sinusoidal motion of the airfoil in (5.2), the pitch velocity oscillates so that the reduced pitch rate is a function of time, as shown in (5.2) (Boutet et al., 2020).

$$\alpha(t) = \alpha_0 + A * \sin(2 * \pi * A * t) \quad (5.2)$$

$$r(t) = k * A * \cos(ft) \quad (5.3)$$

Figure 5.1 illustrates this relationship for oscillations around mean angles of attack  $\alpha_0 = 11^\circ$  and  $\alpha_0 = -8^\circ$  degrees. As depicted in the graphs, an increase in frequency leads to a higher delay in stall onset and an increase in stall onset angle of attack values, consistent with previous observations. Additionally, the figure highlights the dependency on Reynolds number. A decrease in Reynolds number increases the dynamic angle of attack onset for the same reduced pitch value.

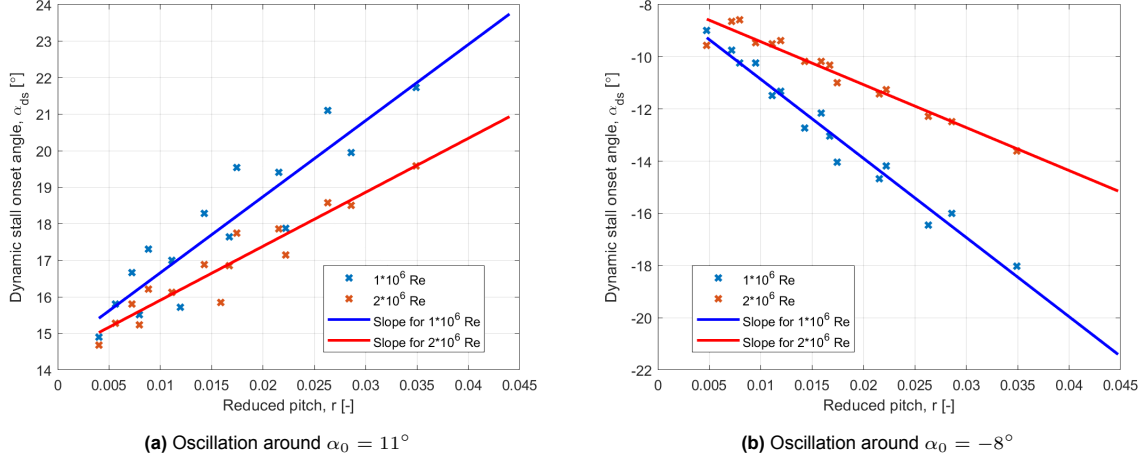


**Figure 5.1:** Determination of time lag  $T_p$  for  $Re = 1 \times 10^6, 2 \times 10^6$  at different amplitudes and frequencies for the FFA-W3-211 airfoil

The aforementioned analysis results in four different values for the  $T_p$  coefficient for two different Reynolds numbers, presented in the Table 5.1. The implementation of the MATLAB code for finding the  $T_p$  coefficient is presented in Appendix C.

### 5.3. Comparison parameters

In this section the numerical parameters that are selected to compare the default and optimized BL model are described.

- **The  $L_2$ -norm**, also known as the Euclidean norm, represents the magnitude of the difference between the model and the data vectors, denoted as  $v$ , normalized by the total number of points in the vector,  $N$ . Mathematically, the  $L_2$ -norm is defined as:

$$L_2\text{-norm} = \sqrt{\frac{1}{N} \sum_{k=1}^N v_k^2}$$

This formula calculates the square root of the average of the squared elements of the vector  $v$ , providing a measure of the overall discrepancy between the model and the observed data.

- **The lift hysteresis parameter**, denoted as  $\Delta C_L^H$ , offers insight into the magnitude of the hysteresis loop and consequently, the severity of unsteady effects. It quantifies the difference between the lift in the upper part of the loop and that in the return part,  $C_{L_{upper}}^H - C_{L_{lower}}^H$ , at the angle of attack corresponding to the static stall AoA,  $\alpha^{st}$ .
- **The reattachment parameter:** Denoted as  $\Delta C_L^R$ , provides insights into the extent of the reattachment area within the hysteresis loop. It signifies the disparity between the lift in the upper portion of the loop and that in the return portion, expressed as  $C_{L_{upper}}^R - C_{L_{lower}}^R$ , at the angle of attack 20% above or below the minimum or maximum AoA, denoted as  $\alpha^{20\%}$  for positive ( $11^\circ$ ) and negative ( $-8^\circ$ ) mean angles, respectively.

### 5.4. Results comparison

In this section, the results of the BL model optimization are presented, and comparison with the original model is conducted. To facilitate comparison between different cases, the discussion is organized as

follows:

$R_e = 1 \times 10^6$  The analysis begins with examining the results for Reynolds numbers of  $R_e = 10^6$ . This section further divides the data to compare the effects of varying frequencies while maintaining constant amplitude values.

$R_e = 2 \times 10^6$  The focus shifts to the cases with  $R_e = 2 \times 10^6$ . Similar to the previous subsection, the impact of different frequencies on the flow characteristics is analyzed while keeping the amplitude values constant.

Before discussing the results, it is necessary to verify that the model works correctly and remains consistent over the entire range of the angle of attack. This verification is shown in Figure 5.2. It can be seen that the model generates slightly shifted results compared to the experimental data. The lack of complex dynamical corrections in the experimental polars can explain this discrepancy. However, the value of the  $C_n$  slope is consistent for the whole span of mean angles of attack; this proves that the physics of the model is consistent throughout the tested ranges.

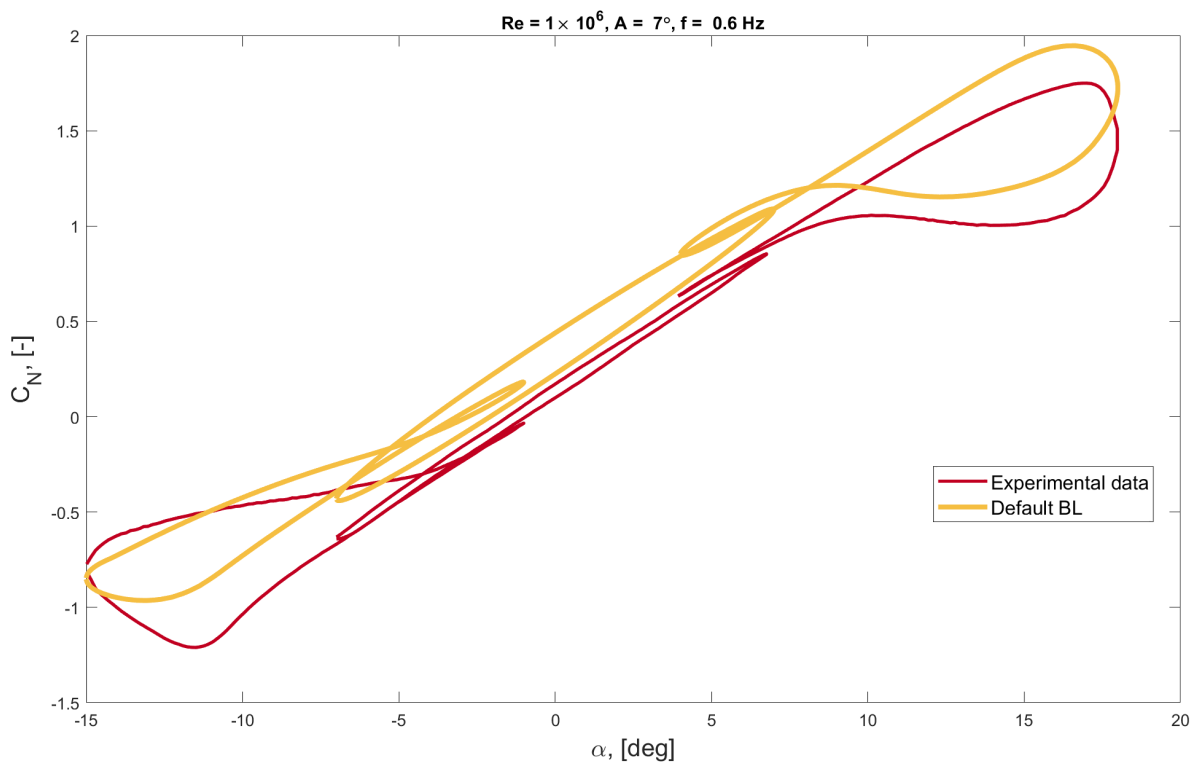


**Figure 5.2:** Normal coefficient plot against the three tested mean angles of attack. The plot serves as validation of the BL model for the full span of AoA

**Table 5.1:** Comparison of semi-empirical parameters for the default and optimized BL models

Parameter Model	Physics based					Shape based			
	Tp	Tf	Tv	Tvl		A1	A2	b1	b2
<b>Default</b>	1.7	3	6	11		0.23	0.7	0.14	0.53
<b>Opt</b> $Re = 1 \times 10^6$ , $\alpha_0 = 11^\circ$	3.65	1.83	2.7	6		0.52	0.57	0.96	0.88
<b>Opt</b> $Re = 2 \times 10^6$ , $\alpha_0 = 11^\circ$	2.5	0.14	5.8	6		1.33	1.31	1.88	1.88
<b>Opt</b> $Re = 1 \times 10^6$ , $\alpha_0 = -8^\circ$	4	1.8	2	6		0.52	0.57	0.96	0.88
<b>Opt</b> $Re = 2 \times 10^6$ , $\alpha_0 = -8^\circ$	2.9	1.15	0.18	6		0.8	0.8	1.88	1.88

To improve the readability and coherence of the paper, the main part is devoted to comparing the hysteresis parameter, the reattachment parameter, and the case analysis for an amplitude of  $9^\circ$ . As discussed earlier in chapter 4, changes in the oscillation amplitude do not affect the fundamental shape of the hysteresis loop. Consequently, the behavior of all parameters remains unchanged for different amplitude values. This approach simplifies the discussion and contributes to a clearer understanding of the results. All other cases for different amplitudes can be found in **Appendix D**.

#### 5.4.1. Oscillation around $\alpha_0 = 11^\circ$ at $Re = 1 \times 10^6$

Figure 5.5a and Figure 5.5b show a comparison of hysteresis and reattachment parameters for  $1 \times 10^6$   $Re$  on the y-axis, respectively, with the reduced frequency plotted on the x-axis.

When considering the values of the hysteresis parameters, it is evident that the optimized model consistently overestimates the loop size. This trend is particularly pronounced at low frequencies, where the default model exhibits noticeably better predictive ability. However, as the frequency increases, the default model significantly lags behind the optimized model. This discrepancy indicates a clear improvement in hysteresis loop prediction by the optimized model compared to its default counterpart.

Notably, the tuned values more closely follow the pattern of the experimental hysteresis loop data, showing a gradual increase up to a reduced frequency value of 0.137, followed by a slight flattening. A particularly significant difference is observed when simulating higher amplitude oscillations, where the optimized model shows a nearly perfect fit to the experimental data.

Overall, these results highlight the effectiveness of the optimized model in capturing the complex dynamics of hysteresis loops, especially noticeable at high amplitudes.

The values of the reattachment parameter also show a notable pattern: the optimized model consistently outperforms the default model in all considered cases. In contrast to the hysteresis parameter, the loop reattachment area is noticeably better predicted at lower amplitudes, demonstrating a near perfect match. It is interesting to note that the default model encounters problems in accurately predicting the linear behavior of the  $C_N$  coefficient after boundary layer reattachment, resulting in pronounced loops at lower angles of attack, as shown in the figures.

Despite the refined fit in the low reduced frequency range, the optimized model encounters drawbacks in the higher frequency ranges. In these cases, reattachment is faster and much more abrupt than observed in the experimental data. Nevertheless, the optimized model shows a significant improve-

ment over the default model. This improvement highlights the effectiveness of the optimized model in capturing the subtleties of the reattachment phenomenon and its overall superior performance under various conditions.

When comparing the L2 norm, shown in Figure 5.7, it is evident that the optimized model is a better fit compared to the default. However, for frequency values of 0.6 Hz at all amplitudes, the default model results in a lower value than the optimized one. Similar dominance of the default model can be seen for the 7° amplitude 1.2 Hz frequency case. In all other cases, the optimized model shows a better fit to the experimental data. Peaks in the L2-norm for the default model at 1.8 and 2.4 Hz frequencies show that the original BL model performance significantly decreases with increase in frequency. The optimized model, on the other hand, shows more stable values.

#### 5.4.2. Oscillation around $\alpha_0 = 11^\circ$ at $Re = 2 \times 10^6$

At a Reynolds number of  $2 \times 10^6$ , the hysteresis parameter, as depicted in Figure 5.6a, mirrors the behavior observed at  $1 \times 10^6$  Reynolds number. The optimized model continues to overestimate the size of the hysteresis loop, particularly evident at lower reduced frequency values. However, as the reduced frequency increases, the optimized model demonstrates a marked improvement compared to the default values.

An interesting observation relates to the behavior of the experimental data. At higher Reynolds numbers, the hysteresis loop shows an almost linear increase with increasing reduced frequency. In contrast to the  $1 \times 10^6$  values, there is no noticeable sharp smoothing in this frequency range.

Similarly, reattachment parameter values, illustrated in Figure 5.6b, exhibit significant enhancement using optimized parameters across all considered cases. Notably, the data forms a distinctive U-shape, with values for certain reduced frequencies being nearly identical. However, the optimized model fails to capture this behavior accurately, particularly dropping further at the final reduced frequency.

The analysis of the L2-norm for this particular case of Reynolds number shown in Figure 5.7 highlights the clear superiority of the optimized model, demonstrating its better fit to all scenarios. An intriguing observation arises when examining the values of the amplitude  $A = 5^\circ$ : both models show a distinct pattern compared to the other amplitudes. Instead of the typical tendency to improve predictions at low frequencies, followed by a decline, both models show the opposite behavior. They improve their predictive abilities with increasing frequency, indicating a deviation from the expected model.

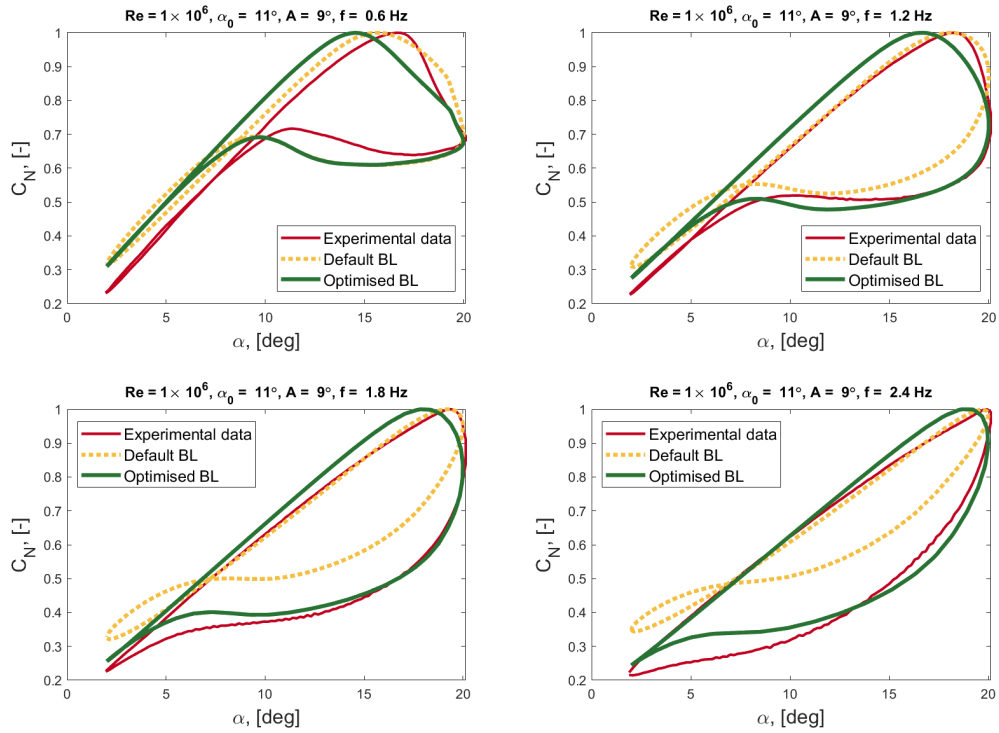


Figure 5.3: Comparison of the optimized and default BL model with experimental data for  $1 \times 10^6$  Re,  $11^\circ$  mean,  $9^\circ$  amplitude.

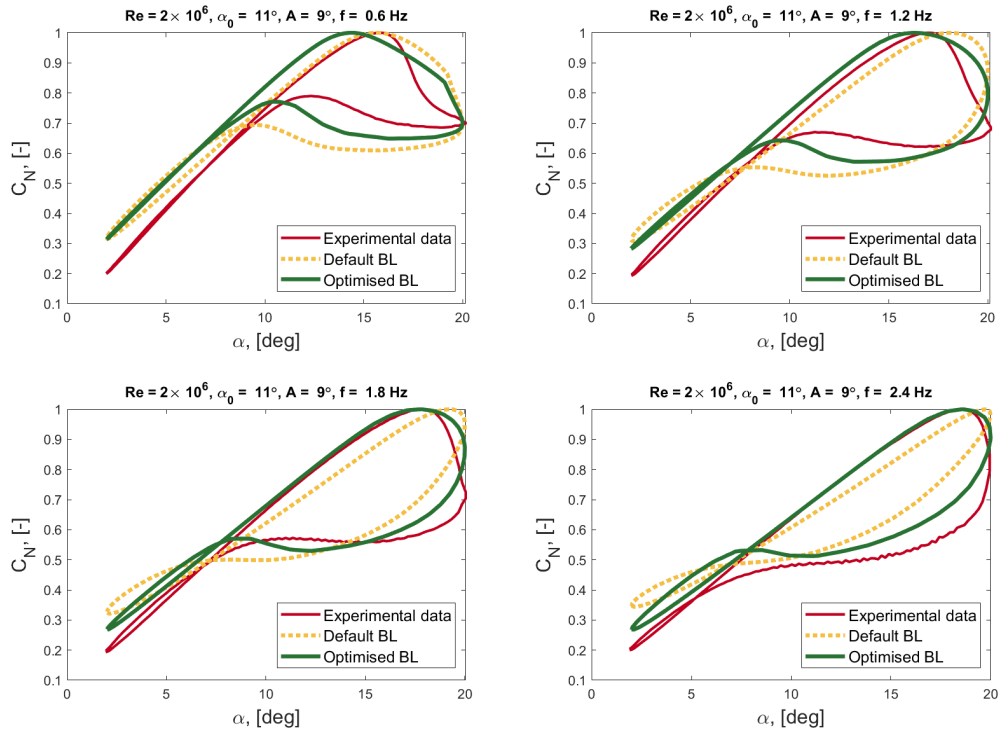


Figure 5.4: Comparison of the optimized and default BL model with experimental data for  $2 \times 10^6$  Re,  $11^\circ$  mean,  $9^\circ$  amplitude.

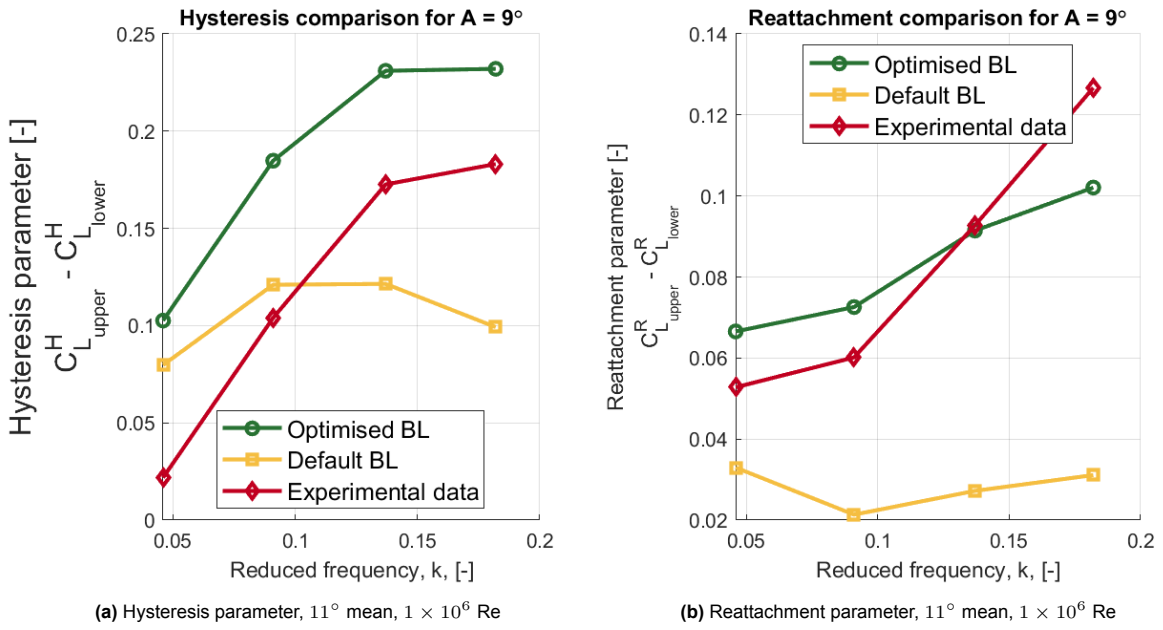


Figure 5.5: Comparison of hysteresis and reattachment parameters

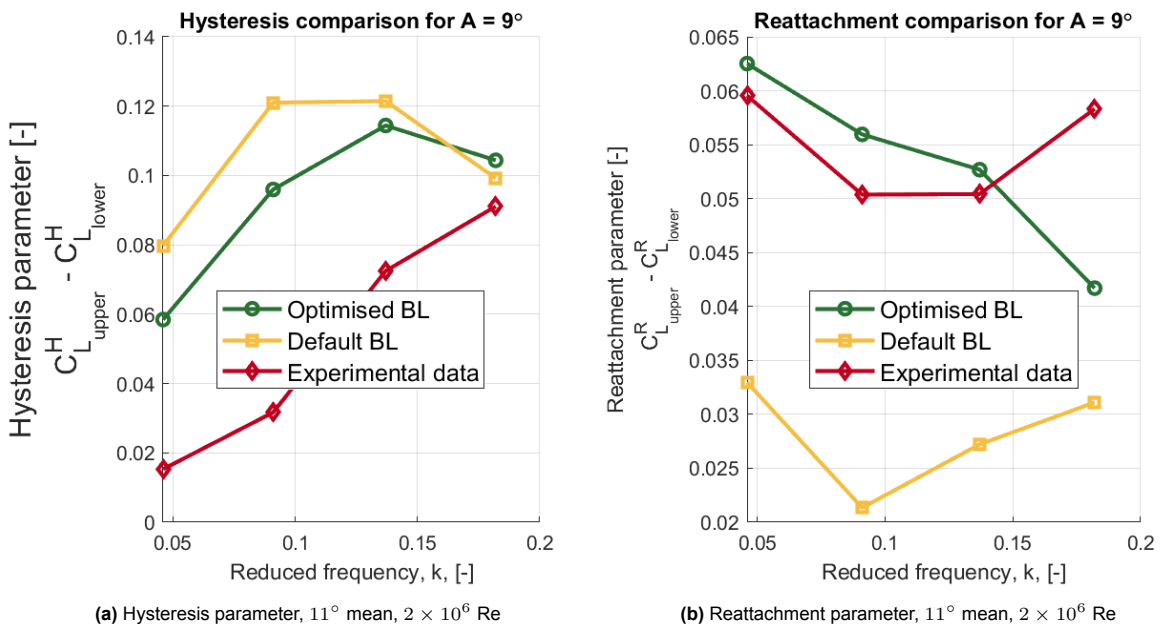


Figure 5.6: Comparison of hysteresis and reattachment parameters

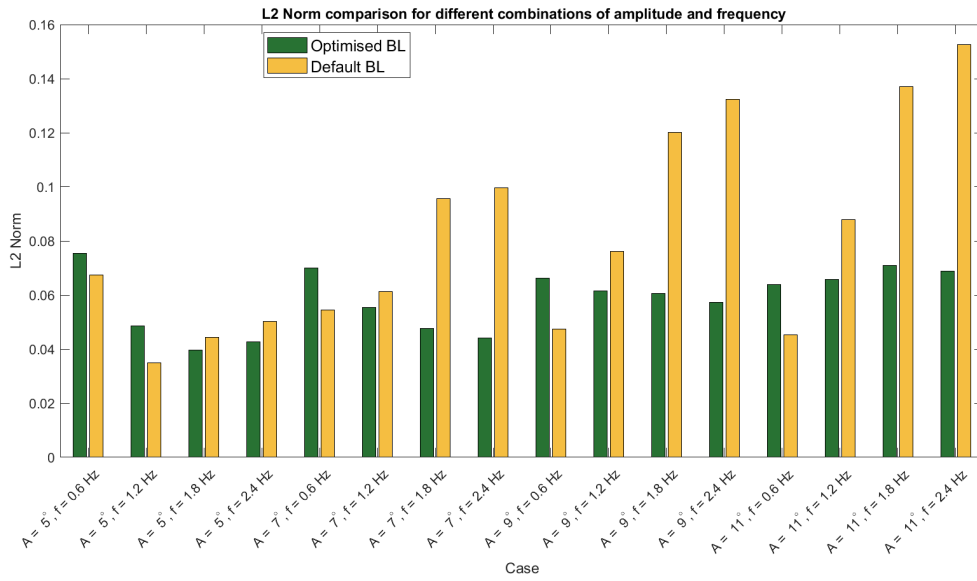


Figure 5.7: L2 parameter comparison for 11° oscillation for 1 × 10<sup>6</sup> Re

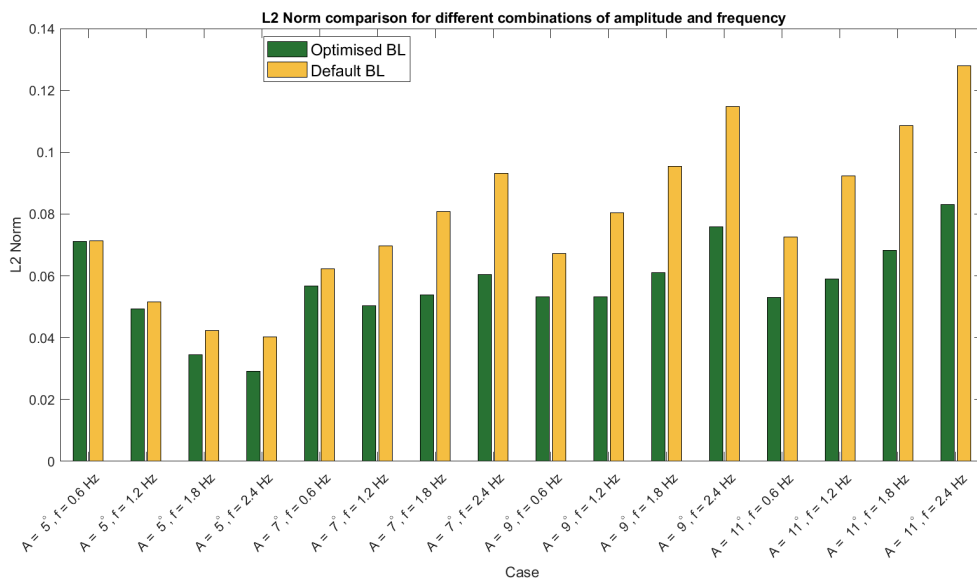


Figure 5.8: L2 parameter comparison for 11° oscillation for 2 × 10<sup>6</sup> Re

### 5.4.3. Oscillation around $\alpha_0 = -8^\circ$ at $Re = 1 \times 10^6$

As can be seen on Figure D.5, the hysteresis parameter is greatly improved by the optimized model. Tailored model values follow the overall increasing trend in the hysteresis parameter with increase in the reduced frequency. The default model, on the other hand, tends to follow the opposite pattern, i.e., gradually reducing the size of the hysteresis loop.

The reattachment parameter, shown in Figure 5.12, shows a smaller improvement between the two models. Noticeable differences can only be observed for the lowest reduced frequency. In other cases, the reattachment area is similar between the models.

Despite the decrease in the predictive accuracy of the Beddoes-Leishman model for negative stall, the optimization resulted in an overall better fit to the experimental data, as can be seen in Figure 5.13. There is a noticeable trend in the data: the errors increase with increasing amplitude. For each amplitude domain, the most significant discrepancies are observed at low frequencies, gradually decreasing with increasing frequency.

It is also noticeable that the results of the model overpredicts the value of the  $C_N$  coefficient. This phenomenon could be attributed to a couple of explanations. Firstly, as previously mentioned, the absence of dynamic corrections in the data could lead to a shift in the model results. Secondly, and perhaps more significantly, the model fails to predict the effect of leading-edge vortex detachment during the downstroke motion. While the downstroke of the model exhibits a purely linear behavior, experimental values show a change in slope due to the influence of the vortex. Lack of this predictive capabilities might have a significant effect on the shape of the hysteresis loop and the reattachment area of the boundary layer.

### 5.4.4. Oscillation around $\alpha_0 = -8^\circ$ at $Re = 2 \times 10^6$

The modeling of the hysteresis parameter at higher Reynolds numbers in Figure 5.12a generally follows the same principles outlined in the previous section. However, upon comparing the overall shape between the experimental data and the model, it becomes evident that the optimized model provides a closer match to the experimental data. The optimized version of the model more accurately predicts the shape and size of the hysteresis loops across all reduced frequency cases.

Regarding the reattachment parameter for the  $Re = 2 \times 10^6$  case, both the default and optimized values exhibit a good match with the data. However, when considering the range of values rather than a single value of the reattachment area, it becomes clear that the optimized model closely predicts the more rapid reattachment process compared to the almost linear behavior of the original model.

In this case, the L2-norm demonstrates a clear pattern. Across all amplitudes, the model performs poorest in predicting values for the lowest reduced frequencies and gradually enhances predictions for higher frequencies. This pattern is consistent for both the improved and classical versions of the models. However, it is evident that optimization enhances the fit for all cases, with the greatest improvement observed for higher frequencies.

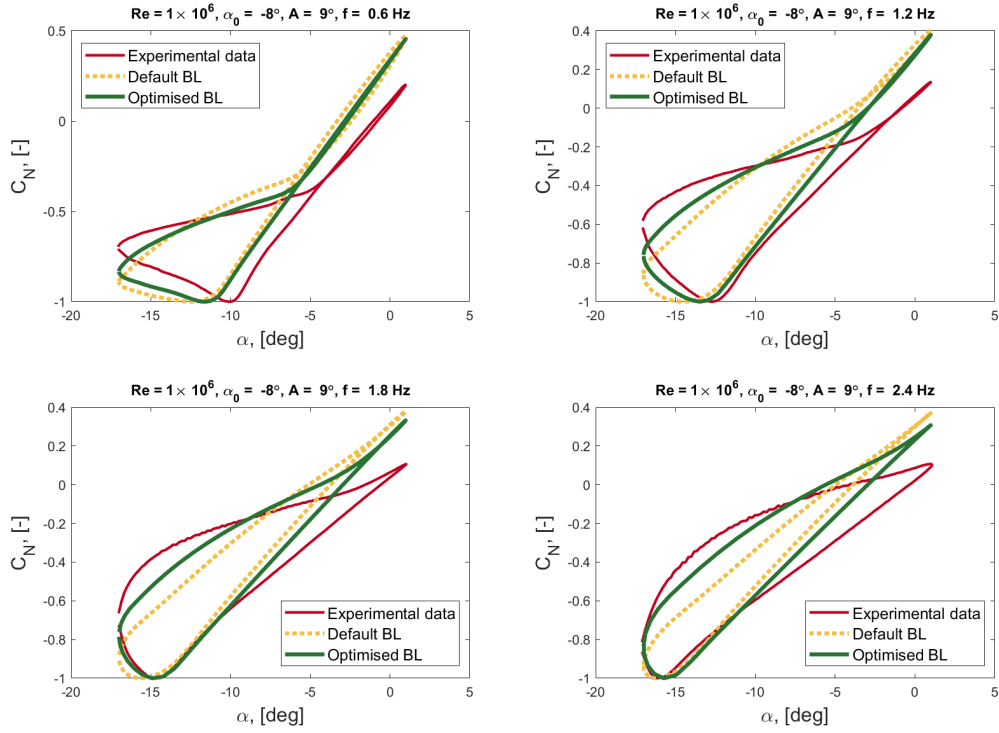


Figure 5.9: Comparison of the optimized and default BL models with experimental data for  $Re = 1 \times 10^6$ ,  $\alpha_0 = -8^\circ$ ,  $A = 9^\circ$ .

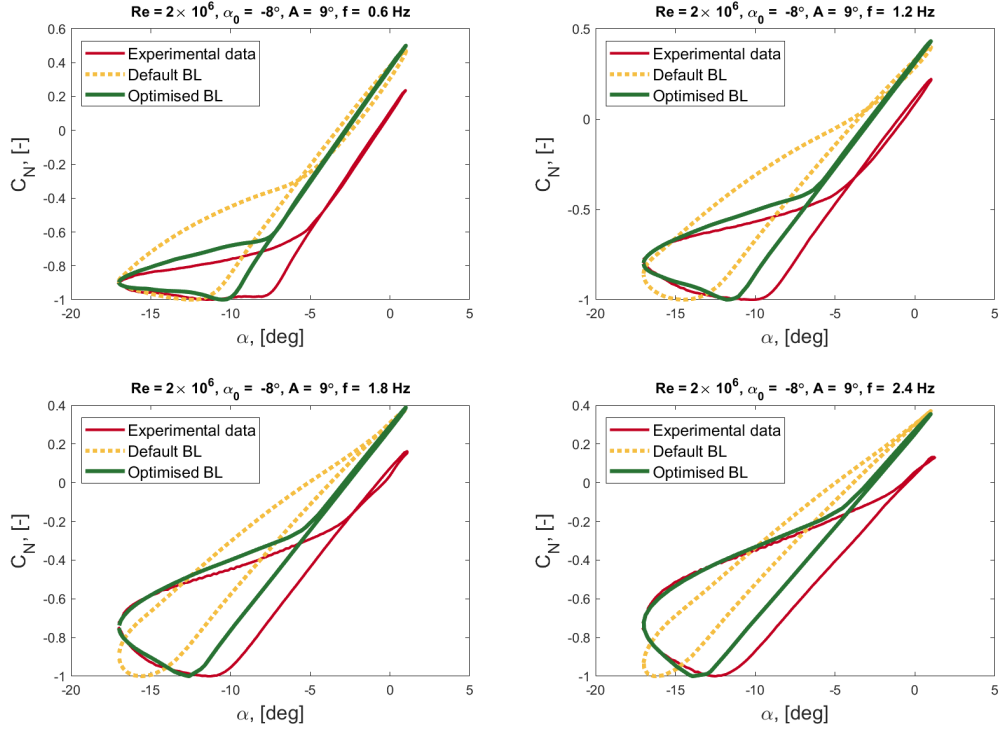


Figure 5.10: Comparison of the optimized and default BL models with experimental data for  $Re = 2 \times 10^6$ ,  $\alpha_0 = -8^\circ$ ,  $A = 9^\circ$ .

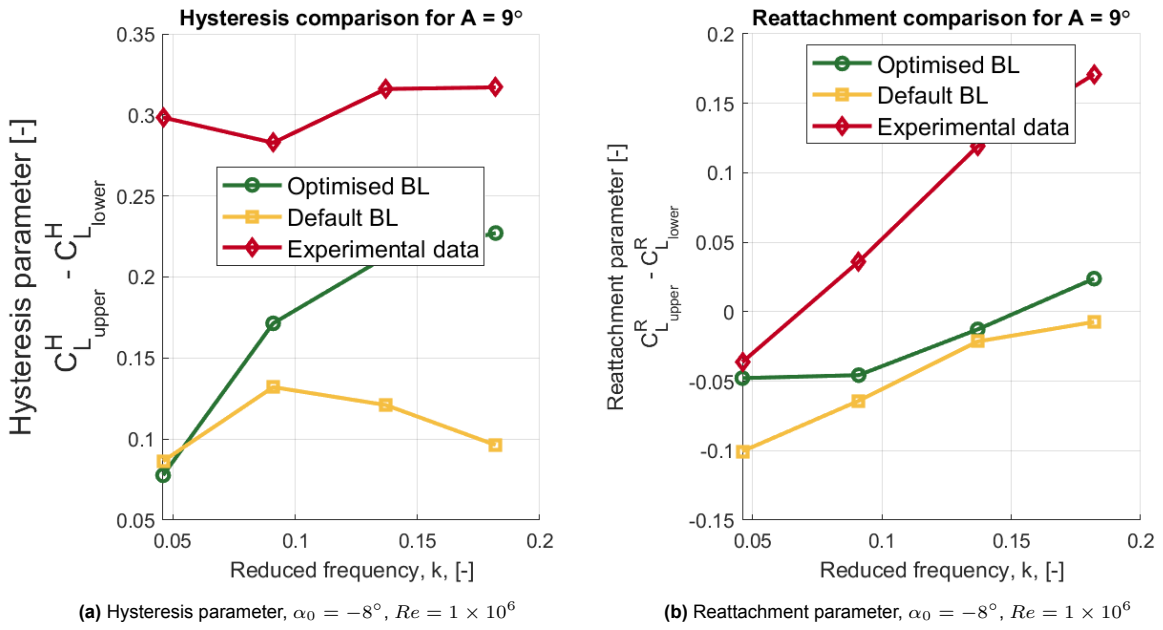


Figure 5.11: Comparison of hysteresis and reattachment parameters

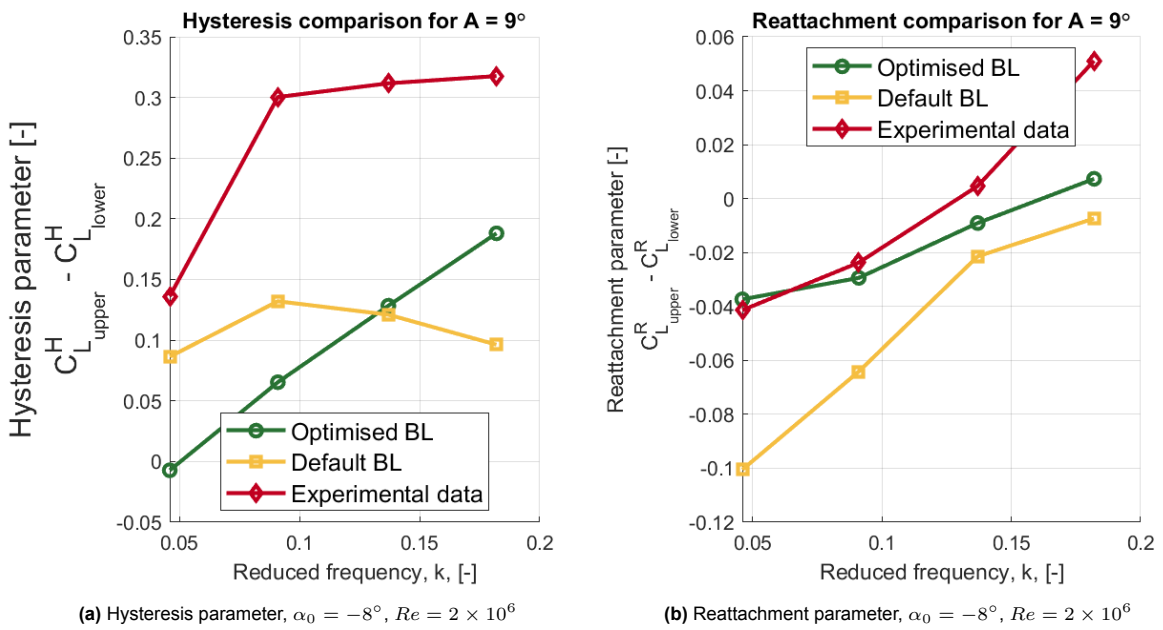


Figure 5.12: Comparison of hysteresis and reattachment parameters

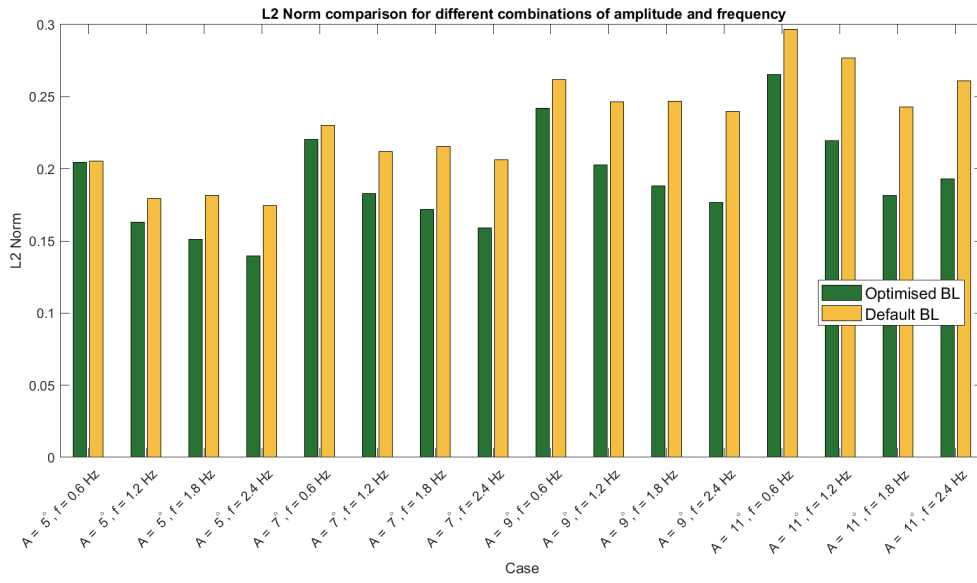


Figure 5.13: L2 parameter comparison for  $\alpha_0 = -8^\circ$ ,  $Re = 1 \times 10^6$

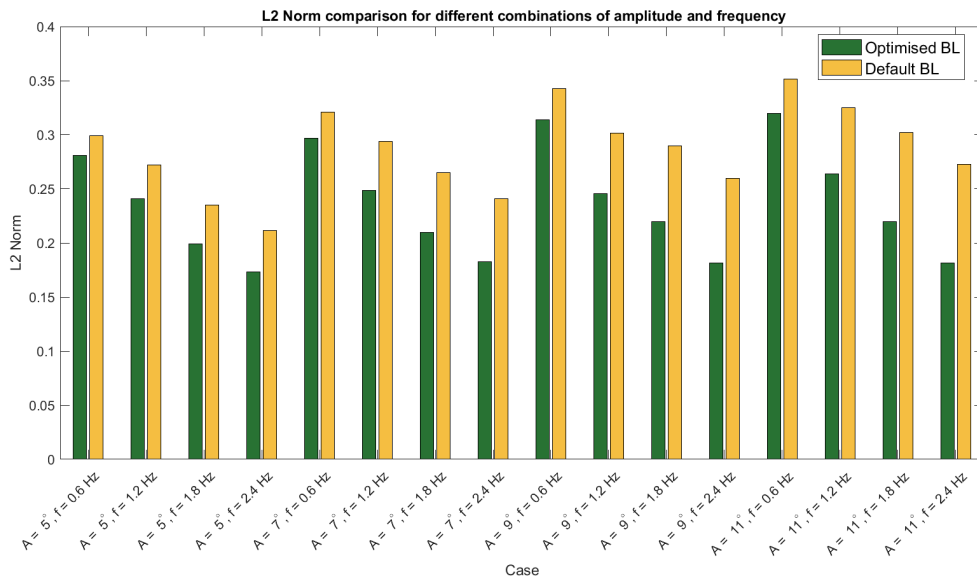


Figure 5.14: L2 parameter comparison for  $\alpha_0 = -8^\circ$ ,  $Re = 2 \times 10^6$

# 6

## Snel model optimization results

The optimization process for the Snel model is conducted in a similar way as described in chapter 5. However, due to the obvious difference in the modeling approach adopted in the Snel model, it is important to first discuss the optimization variables.

In this study, only the first-order correction is used for several reasons. First, the computational complexity of the second-order model is higher, and since the goal of the semi-empirical model is simplicity and efficiency, the first-order approach is preferred. Second, the inclusion of second-order conditions introduces additional variables and constraints, making the optimization process more complex and time-consuming. Finally, and perhaps most importantly, the experimental data did not show any secondary effects of vortex or other complex behaviors that would require the use of second-order conditions. The first-order correction is found to give satisfactory results without complicating the model.

In the first-order correction, the only parameter that affects the model is the  $cf_{10}$  coefficient, as illustrated in (3.2). It is observed that the constants  $x_{11}$  through  $x_{23}$ , outlined in (6), significantly influence the model's outcome. However, including all six independent variables makes the optimization process computationally inefficient. During the study of the model behavior, it is determined that satisfactory results could be achieved by modifying only the  $x_{12}$  and  $x_{22}$  constants during the optimization of the upstroke and downstroke motions. The remaining parameters are kept unchanged, consistent with the default model settings.

$$cf_{10} = \begin{cases} \frac{x_{11} + 0.5\Delta c_{l,pot}}{x_{12}(x_{13} + 60\tau\dot{\alpha})} & \text{if } \dot{\alpha}c_{l,pot} \leq 0 \\ \frac{x_{21} + 0.5\Delta c_{l,pot}}{x_{22}(x_{23} + 80\tau\dot{\alpha})} & \text{if } \dot{\alpha}c_{l,pot} > 0 \end{cases} \quad (6.1)$$

Similar to the BL model validation, Figure 6.1 displays the values of the  $C_N$  coefficient plotted as a function of the angle of attack along the y and x axes, respectively, for the Snel model. As can be seen, there is a similar offset of the modeled results compared to the experimental data due to the lack of corrections. However, despite this deviation, the model demonstrates proper behavior, as indicated by the constant slope of the  $C_N$  coefficient.

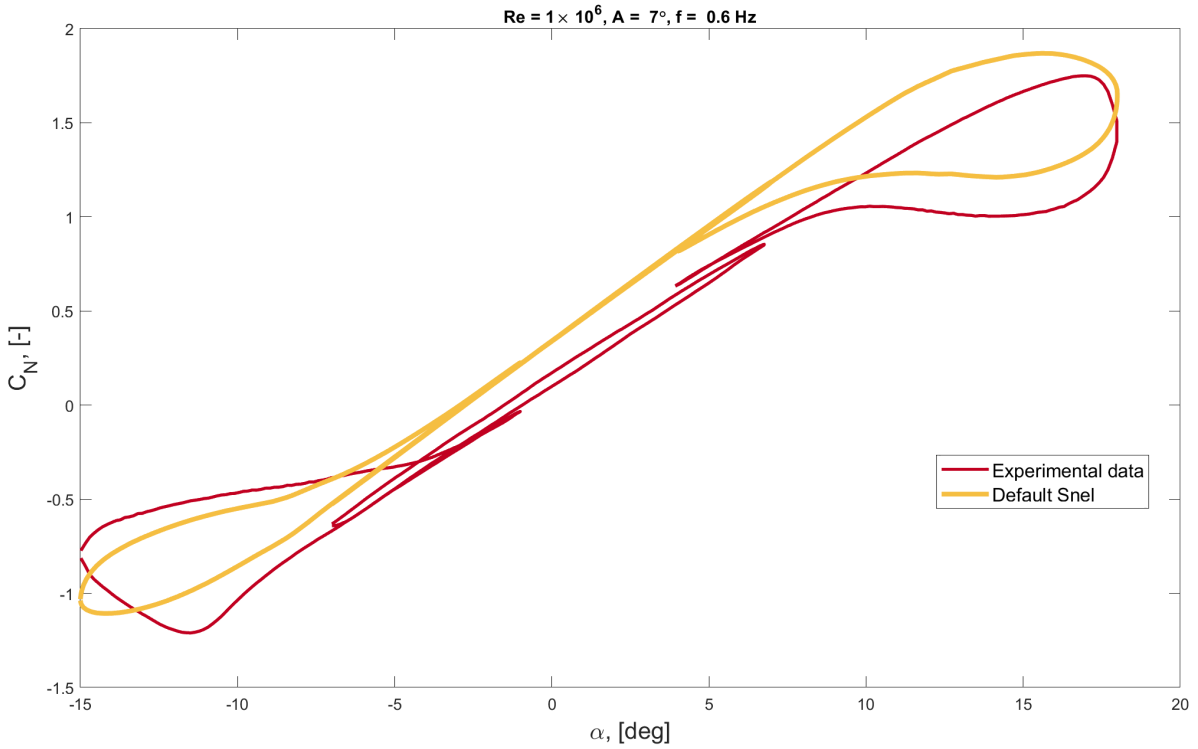


Figure 6.1: Snel model validation over the span of angle of attack

## 6.1. Results comparison

Results are described and compared in the same way as in chapter 5. L2-norm, hysteresis and reattachment parameters are compared between the experimental data, default and optimized model. Discussion of the results are separated per Reynolds number and mean angle of oscillation.

### 6.1.1. Oscillation around $\alpha_0 = 11^\circ$ at $Re = 1 \times 10^6$

When examining the hysteresis parameter illustrated in Figure 6.4a, an interesting trend emerges: the optimized model initially outperforms the default model but later loses its advantage. At a Reynolds number of  $Re = 1 \times 10^6$ , the Snel model tends to underestimate hysteresis, particularly at higher reduced frequencies. Conversely, the default model excels in predicting larger hysteresis loops as oscillation frequency increases.

Similarly, the reattachment parameter values depicted in Figure 6.4b reveal that the optimized model struggles to accurately capture reattachment areas at this Reynolds number. It exhibits earlier and more rapid reattachment compared to the actual data, a disparity more pronounced at higher reduced frequencies.

Despite these discrepancies, the L2 norm illustrated in Figure 6.6 indicates an overall improvement with the optimized model. It achieves a nearly perfect fit of the  $C_N$  coefficient during the upstroke motion, in contrast to the default values, which consistently overestimate values throughout the airfoil motion. Additionally, as shown in Figure 6.2, the optimized model enhances stall onset prediction, particularly at higher reduced frequencies.

Overall, it appears that the Snel model at this Reynolds number tends to overpredict reattachment speed, resulting in underestimations of both hysteresis and reattachment parameters. However, the optimized model demonstrates near-perfect behavior during the upstroke motion and stall onset, showcasing significant improvements in the prediction of  $C_N$  behavior.

### 6.1.2. Oscillation around $\alpha_0 = 11^\circ$ at $Re = 2 \times 10^6$

The increase in Reynolds number has notably enhanced the predictive capabilities of the optimized model. As depicted in Figure 6.5a, near-perfect hysteresis loop fit is achieved post-optimization. Notably, for  $Re = 2 \times 10^6$ , the experimental data exhibits a linear increase in hysteresis size with reduced frequency, mirroring the behavior of the optimized model. In contrast, the default model, as observed in Figure 6.3, consistently fails to capture the correct downstroke behavior and widens the hysteresis loop size.

Regarding the reattachment parameter illustrated in Figure 6.5b, the optimized model clearly outperforms the default model. Despite a slight overprediction, the tailored version closely follows the behavior depicted by the experimental data. Conversely, the default model predicts less rapid reattachment during the downstroke motion, significantly impacting the overall hysteresis shape and reattachment parameter.

Analyzing the L2-norm values showcased in Figure 6.7, it's evident that the optimized model holds a significant advantage over the default one. The L2-norm values for the new model are considerably lower, indicating a much better fit with the experimental data. However, despite these promising results, particularly for high reduced frequencies, it's worth noting that for the case of Amplitude  $A = 9^\circ$  and frequency  $f = 0.6Hz$ , the default model yields a slightly better fit.

In conclusion, the capabilities of the optimized model are markedly improved at higher Reynolds number values. It demonstrates accurate predictions of hysteresis size and shape, as well as precise estimation of reattachment areas. The most significant improvement is observed at the higher end of reduced frequencies.

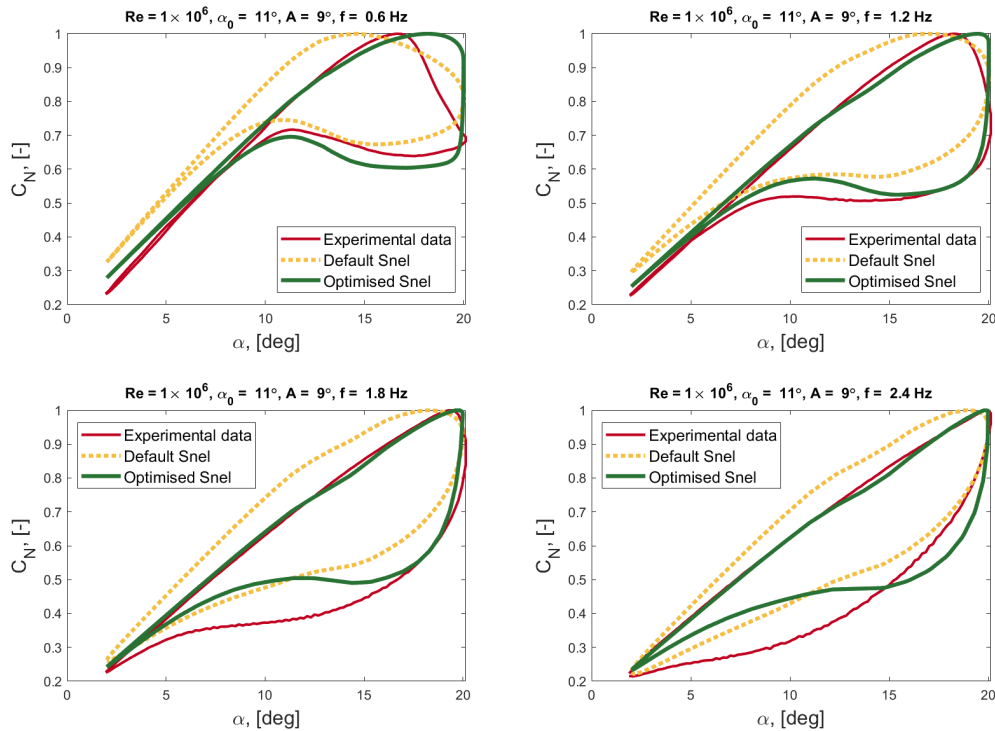


**Figure 6.2:** Comparison of the optimized and default Snel model with experimental data for  $Re = 1 \times 10^6$ ,  $\alpha_0 = 11^\circ$ ,  $A = 9^\circ$ .

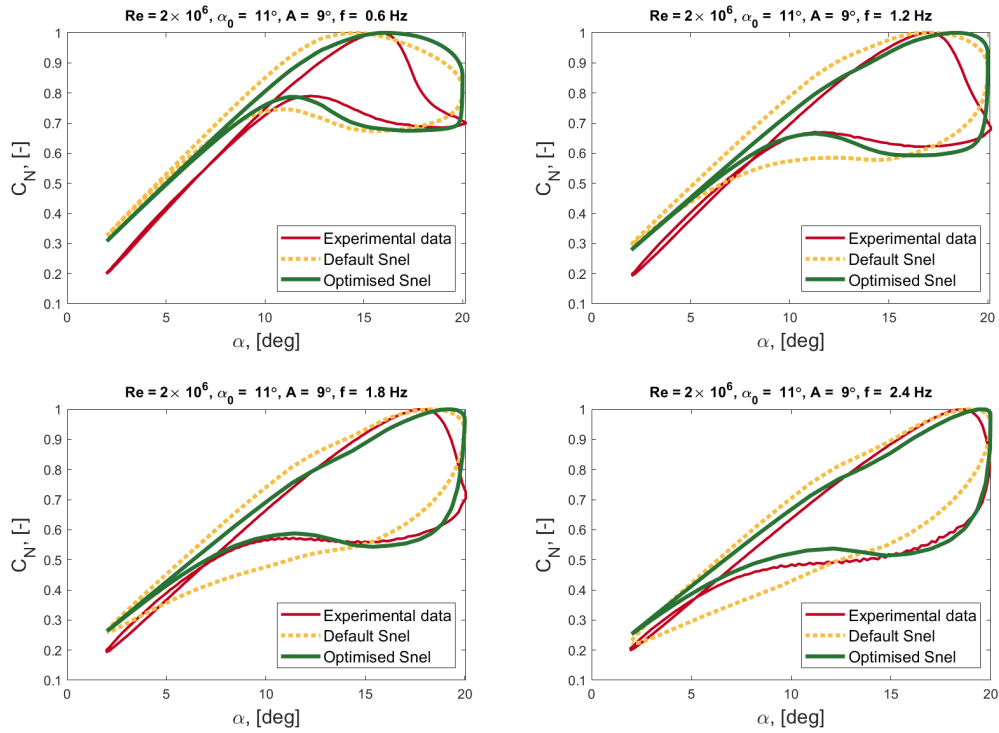
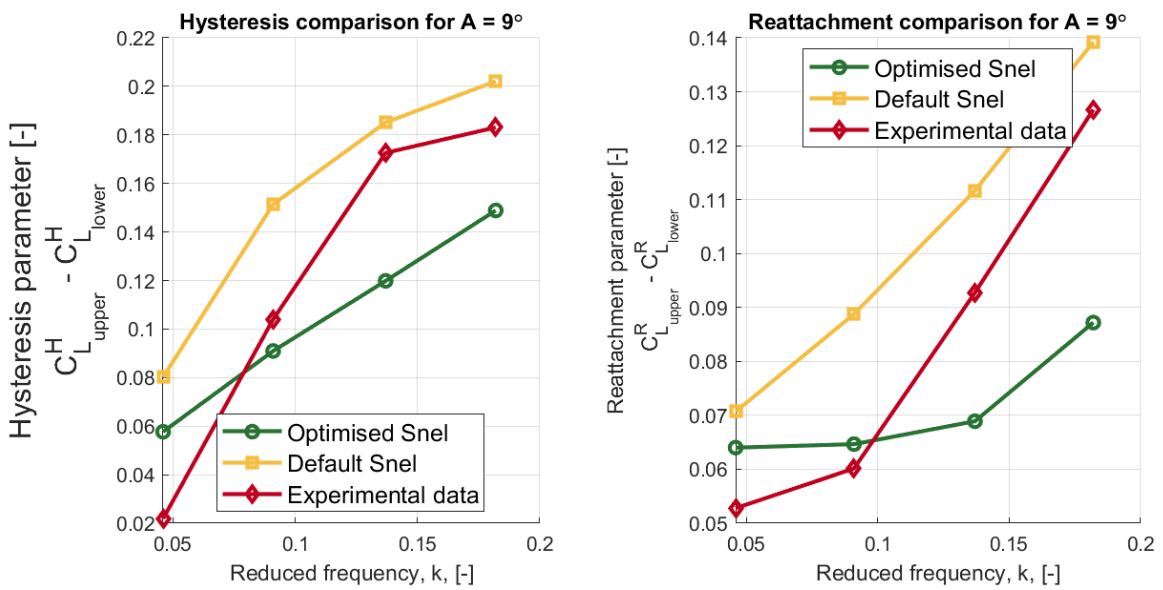


Figure 6.3: Comparison of the optimized and default Snel model with experimental data for  $Re = 2 \times 10^6$ ,  $\alpha_0 = 11^\circ$ ,  $A = 9^\circ$ .



(a) Hysteresis parameter,  $\alpha_0 = 11^\circ$ ,  $Re = 1 \times 10^6$

(b) Reattachment parameter,  $\alpha_0 = 11^\circ$ ,  $Re = 1 \times 10^6$

Figure 6.4: Comparison of hysteresis and reattachment parameters for  $Re = 1 \times 10^6$ ,  $A = 9^\circ$

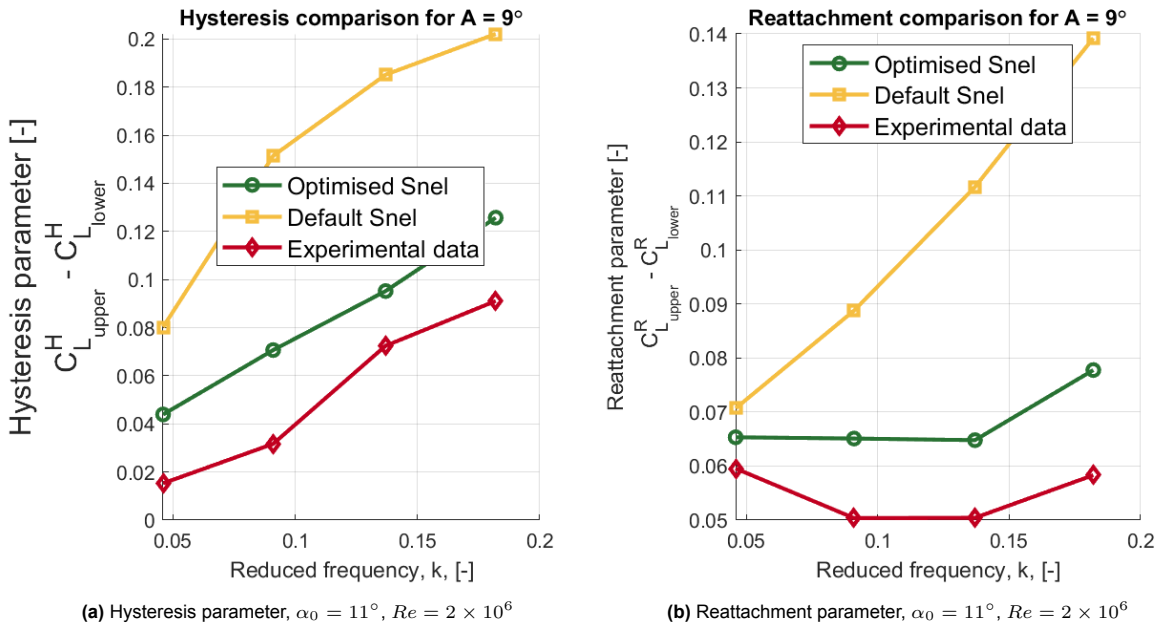


Figure 6.5: Comparison of hysteresis and reattachment parameters for  $Re = 2 \times 10^6$ ,  $A = 9^\circ$

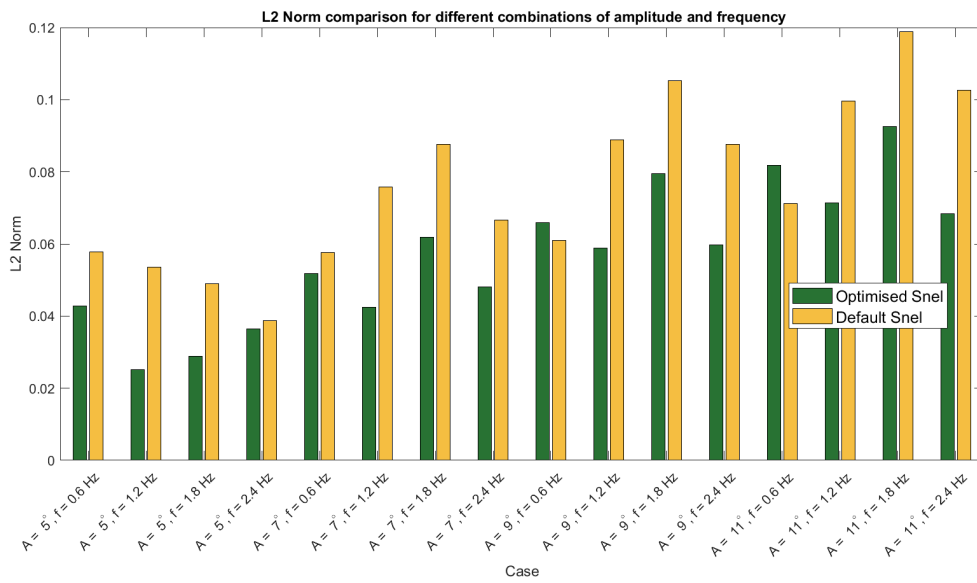


Figure 6.6: L2 parameter comparison for  $\alpha_0 = 11^\circ$ ,  $Re = 1 \times 10^6$

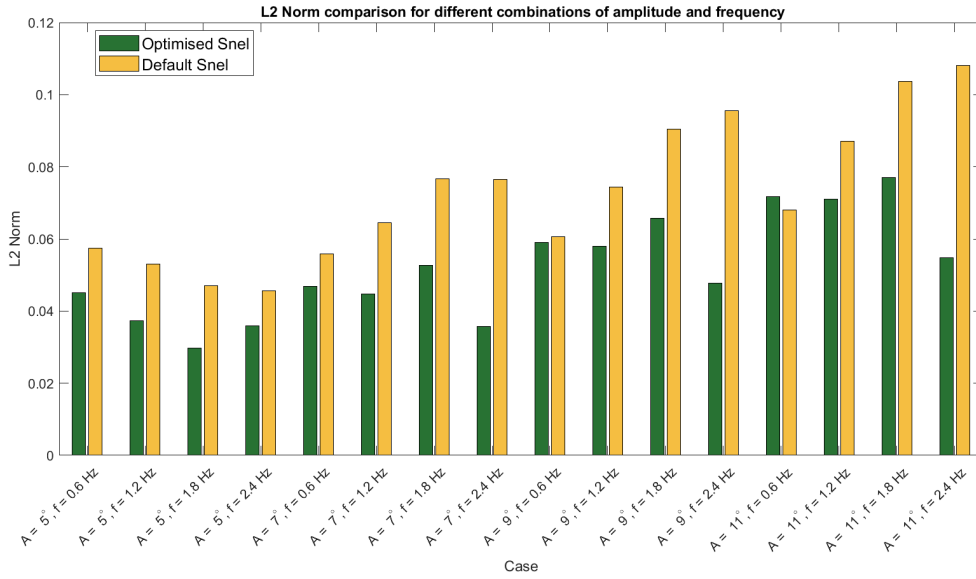


Figure 6.7: L2 parameter comparison for  $\alpha_0 = 11^\circ$ ,  $Re = 2 \times 10^6$

### 6.1.3. Oscillation around $\alpha_0 = -8^\circ$ at $Re = 1 \times 10^6$ and $Re = 2 \times 10^6$

The analysis of negative stall behavior is conducted for both Reynolds numbers due to their similar and unfavorable outcomes. As seen in Figure 6.8 and Figure 6.9, the Snel model struggles to accurately predict behavior in the negative angle of attack (AoA) domain. A critical flaw lies in its inability to properly model leading-edge vortex behavior, crucial for negative stall prediction. Unlike observed behavior, the model exhibits a decrease in the rate of change past the mean angle, resulting in an inaccurately shaped hysteresis loop.

However, the optimized version of the model shows improvement in post-stall behavior. The hysteresis shape closely resembles the experimental data, with a better fit continuing until it reaches the mean angle,  $\alpha_0 = -8^\circ$ . At this point, the model predicts rapid reattachment of the boundary layer and a noticeable change in the  $C_N$  slope. This process is particularly evident at higher reduced frequencies, where the flow does not fully reattach by the end of the cycle.

Additionally, the model incorrectly shifts the stall angle to lower values, impacting hysteresis parameter estimation, as evident in Figure 6.10a and Figure 6.11a. While both optimized and default models show an increasing hysteresis trend with frequency, the erroneous slope change of the  $C_N$  curve leads to a shifted stall onset AoA and subsequently, a distorted hysteresis shape.

Despite the initial disappointment, optimization yielded improvements in L2-norm readings. For Reynolds numbers  $Re = 1 \times 10^6$ , enhancements are observed across most cases, particularly at higher frequencies for all amplitudes. Notably, the model performed better in predicting higher reduced frequency values. Similarly, for Reynolds numbers  $Re = 2 \times 10^6$ , a stable trend in L2-norm is observed throughout the study. As oscillation frequency increased, the model consistently showed improved readings across all amplitudes. Notably, the optimized model consistently outperformed the default model, with the improvement increasing as frequency rises.

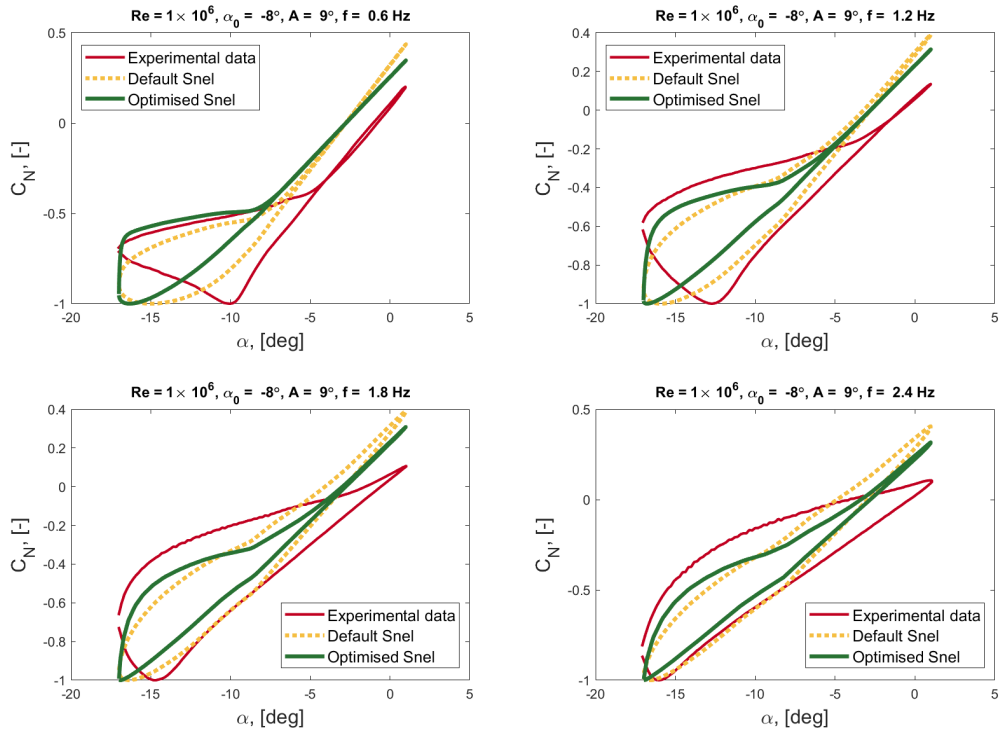


**Figure 6.8:** Optimized and default Snel models comparison with experimental data for  $Re = 1 \times 10^6$ ,  $\alpha_0 = -8^\circ$ ,  $A = 9^\circ$ .

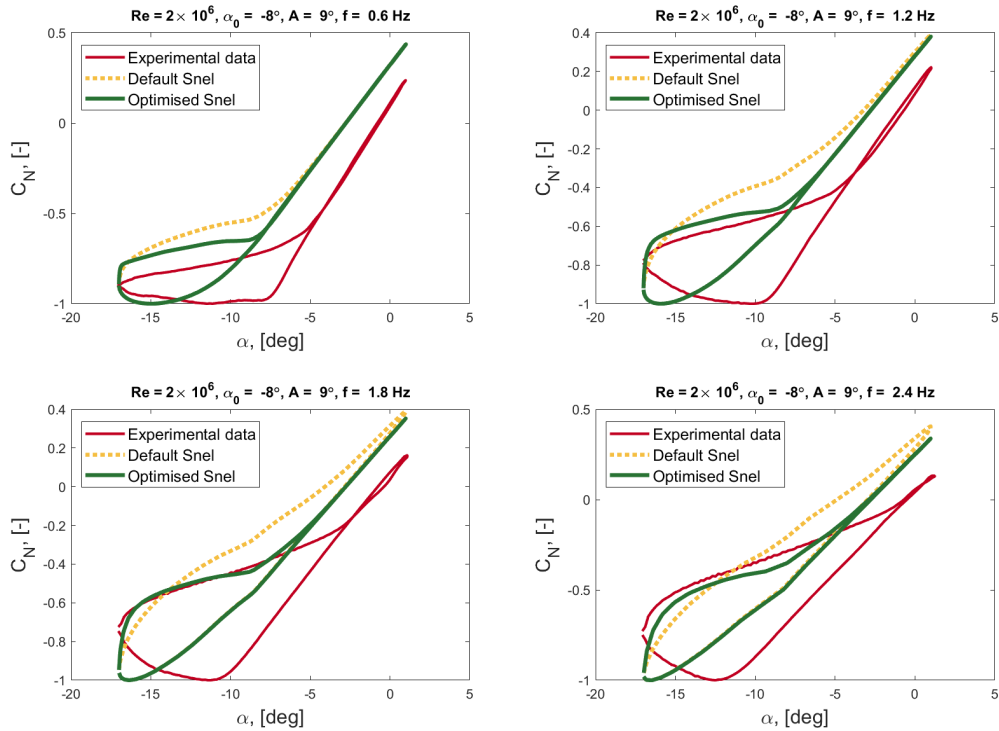


**Figure 6.9:** Optimized and default Snel models comparison with experimental data for  $Re = 2 \times 10^6$ ,  $\alpha_0 = -8^\circ$ ,  $A = 9^\circ$ .

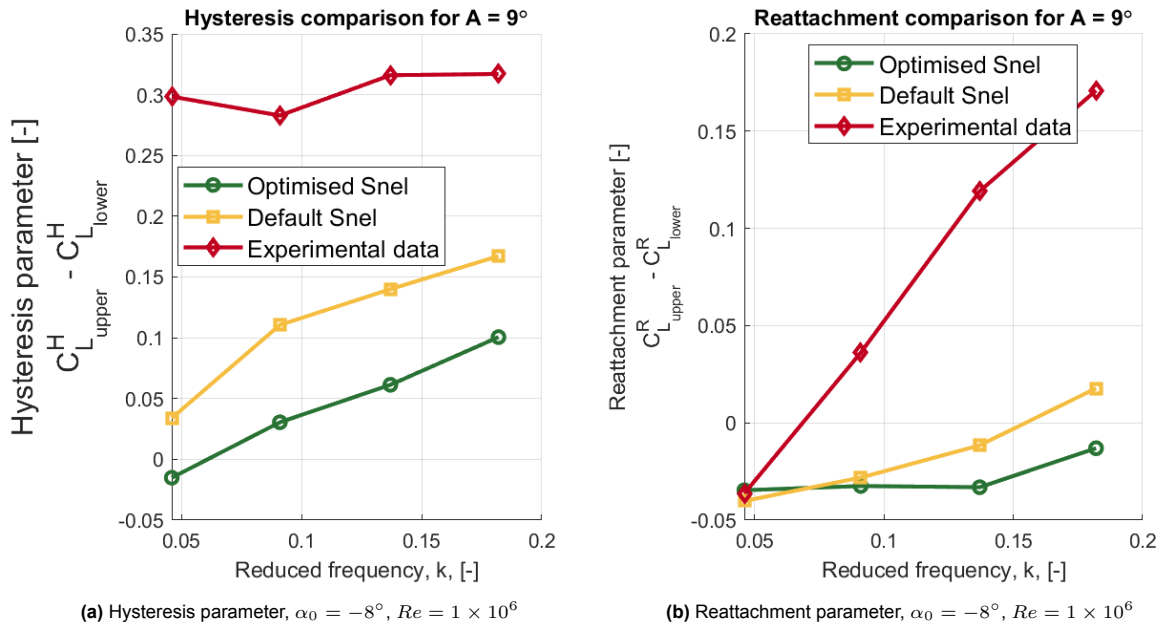


**Figure 6.10:** Comparison of hysteresis and reattachment parameters for  $Re = 1 \times 10^6$ ,  $A = 9^\circ$

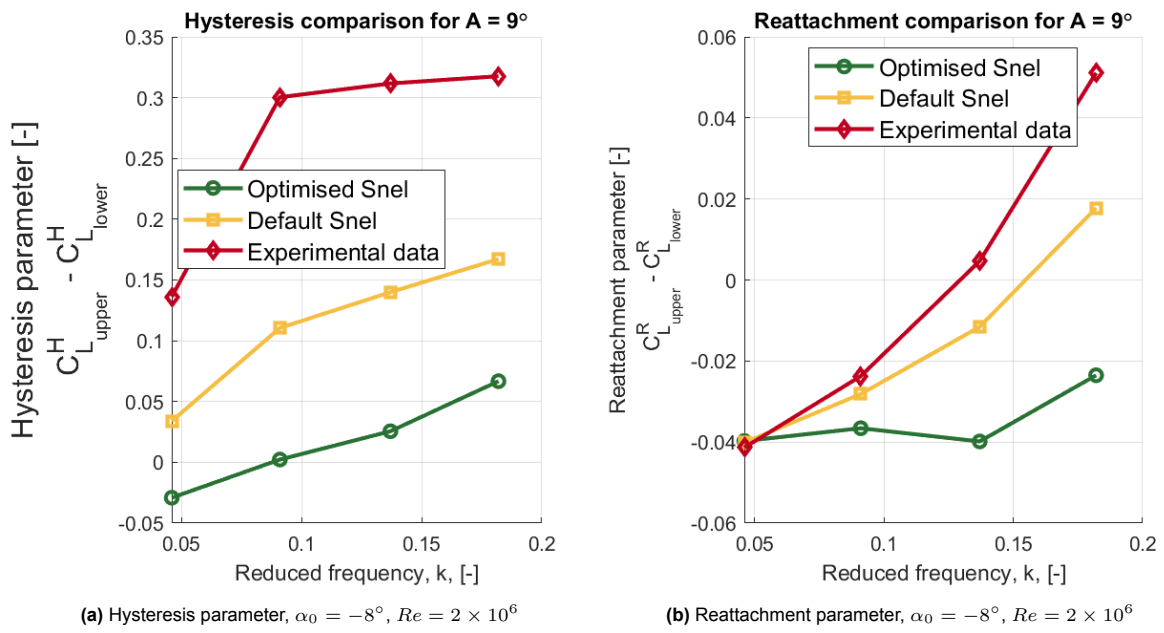


**Figure 6.11:** Comparison of hysteresis and reattachment parameters for  $Re = 2 \times 10^6$ ,  $A = 9^\circ$

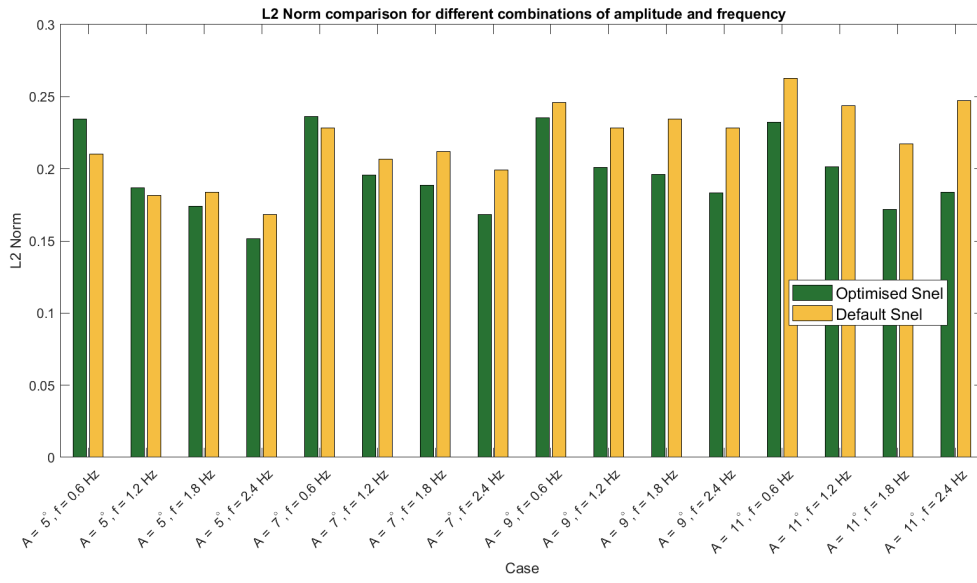


Figure 6.12: L2 parameter comparison for  $\alpha_0 = -8^\circ$ ,  $Re = 1 \times 10^6$

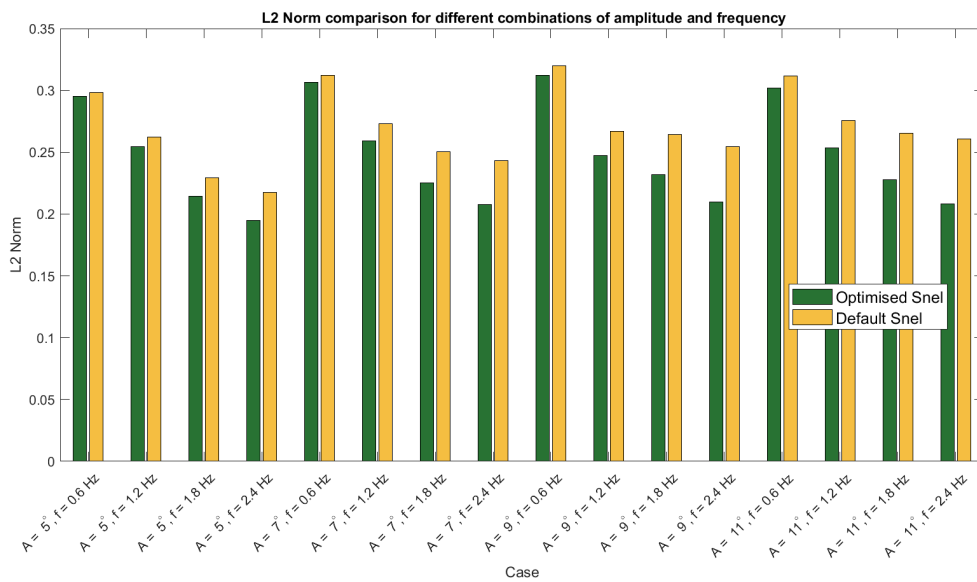


Figure 6.13: L2 parameter comparison for  $\alpha_0 = -8^\circ$ ,  $Re = 2 \times 10^6$

# 7

## Model comparison

This chapter is dedicated to comparing two optimized models. The discussion is structured as follows. Section 7.1 presents a comparison between the two models at  $\alpha_0 = 11^\circ$ . Followed by section 7.2 discussing the differences between the two models during negative stall conditions.

### 7.1. Oscillation around $\alpha_0 = 11^\circ$ at $Re = 1 \times 10^6$ and $Re = 2 \times 10^6$

For the oscillation around a positive angle of attack for both Reynolds numbers, explored in this paper, both models gives satisfactory results. Both of them have their strong and weak points. To evaluate the models performance, the metrics, described in chapter 3, are used.

The analysis begins with the hysteresis parameter, depicted in Figure 7.3a and Figure 7.4a. One can notice that for lower Reynolds number, the BL model captures the trend of the data much better compared to the Snel model. However, at lower reduced frequencies, the fit with Snel model, the value is closer to the experimental with the hysteresis parameter difference of 0.0075. An increase in reduced frequency puts the Snel model behind, increasing the difference in hysteresis parameter up to 0.12. At that region, BL model has an advantage, improving the hysteresis value difference from 0.11 to 0.013.

When considering higher Reynolds number values, supremacy of the Snel model is evident with the near-perfect match on the whole range of reduced frequencies with the maximum error of 0.02. The BL model, although having a close fit does not achieve such a close match with the data.

Hysteresis analysis continues with the noticeable difference between the two models when looking at Figure 7.1 and Figure 7.1. The BL model is susceptible to underpredicting the dynamic stall onset AoA. The most prominent difference of  $\Delta\alpha_{st} = 2.13^\circ$  and  $\Delta\alpha_{st} = 1.52^\circ$  is achieved at  $f = 0.6Hz$  for  $Re = 1 \times 10^6$  and  $Re = 2 \times 10^6$ , respectively. The difference in stall onset AoA gradually decreases as the oscillating frequency rises, reaching a value of  $\Delta\alpha_{st} = 1.26^\circ$  and close to perfect  $\Delta\alpha_{st} = 0.04^\circ$  at  $f = 2.4Hz$  for  $Re = 1 \times 10^6$  and  $Re = 2 \times 10^6$ .

The Snel model, on the other hand, tends to overpredict the stall angle. However, the higher differences are noticed at higher range of frequencies at  $f = 1.8Hz$  and  $f = 2.4Hz$ , with the values of  $\Delta\alpha_{st} = 1.8^\circ$  and  $\Delta\alpha_{st} = 0.93^\circ$  for considered Reynolds numbers. At  $Re = 1 \times 10^6$ , The Snel model has an advantage over the BL model, as the dynamic stall AoA is precisely predicted for  $f = 1.8Hz$  and  $f = 2.4Hz$  with the angle difference of  $\Delta\alpha_{st} = 0.25^\circ$  and  $\Delta\alpha_{st} = 0.11^\circ$ . This advantage, however, does not hold for higher Reynolds numbers. There, the Snel model consistently overpredicts the onset AoA:  $\Delta\alpha_{st} = 1.45^\circ$  and  $\Delta\alpha_{st} = 0.93^\circ$  for  $f = 1.8Hz$  and  $f = 2.4Hz$ .

The comparison of reattachment parameters is presented in Figure 7.3b and Figure 7.4b. For  $Re = 1 \times 10^6$ , both models exhibit similar trends. The reattachment parameter values form a relatively flat line

compared to the increasing values observed in the experimental data. Notably, both models demonstrate a good fit at  $f = 0.6Hz$  and  $f = 1.2Hz$ . However, at higher frequencies, a wider hysteresis and a slower reattachment process are introduced. At this Reynolds number, the flow does not fully reattach by the end of the oscillating cycle. Both the Snel and BL models underestimate the speed of reattachment, with this behavior becoming more pronounced at higher frequencies.

At  $Re = 2 \times 10^6$ , interesting differences between the models are observed. At higher Reynolds numbers, the reattachment of the flow occurs earlier and more rapidly. This results in smaller secondary loops in the  $C_N$  coefficient at low AoA. The BL model, as can be seen, is capable of capturing this behavior, and as mentioned before, shape-based parameters heavily affect the size of these smaller loops. However, according to the data, these loops keep getting bigger until a certain value of frequency. After reaching a certain frequency threshold, the boundary layer is not able to reattach, and the loop disappears. This behavior is not observed by the BL model. Therefore, it can be observed that these secondary loops keep growing with an increase in frequency, resulting in a continuous decrease of the reattachment parameter value, as depicted in Figure 7.4b.

On the contrary, the Snel model is incapable of capturing this effect. In all examined cases, the upstroke values are consistently higher than the downstroke values. This indicates a lack of physical representation in this simple model. Despite this shortcoming, the model does fairly accurately capture the trend in reattachment area development with increasing frequencies. As can be seen, the values are shifted upward. This can be attributed to the model's inability to create loops at low angles. Therefore, it takes more time for the model to predict the reattachment of the boundary layer.

The L2-norm comparison for two Reynolds numbers is presented in Figure 7.5 and Figure 7.6.

At  $Re = 1 \times 10^6$ , no specific patterns are observed in the dataset, but a general trend can be described. The BL model performs better at the higher end of the amplitude values, exhibiting a stable L2-norm value between 0.071 and 0.064 at  $A = 11^\circ$ . Another noticeable feature is the pronounced peaks that occur for the  $f = 0.6Hz$  cases. This occurs due to the overestimation of the  $C_N$  at this frequency. However, an increase in amplitude significantly improves this, resulting in a flattening of values with no major peaks occurring.

Conversely, the Snel model has a clear advantage when it comes to lower amplitudes at both considered Reynolds numbers. Specifically, at  $Re = 1 \times 10^6$ , the model is capable of perfectly predicting the upstroke values for the  $C_N$  coefficient for all cases, resulting in low L2-norm values down to a minimum of  $L2 = 0.025$ . Another interesting detail observed at this Reynolds number is that the Snel model peaks at frequency values of  $f = 0.6Hz$  and  $f = 1.8Hz$  and drops at others.

For  $Re = 2 \times 10^6$ , the results are similar. The BL model at the low amplitude domain results in larger errors and a distinct peak at  $f = 0.6Hz$ . Additional peaks are present for the BL L2-norm values at  $f = 2.4Hz$ , except for the  $A = 5^\circ$  case, where the BL model performs the best. These peaks can be attributed to the secondary loops at lower AoA and an overestimation of the  $C_N$  during the downstroke motion.

The Snel model begins to perform poorer compared to the BL model at  $A = 9^\circ$  and above. Interestingly, for the  $f = 2.4Hz$  cases, the L2 values significantly drop. This behavior is a result of a more accurate  $C_N$  drop modelling as well as smaller underprediction values during both upstroke and downstroke motions.

## 7.2. Oscillation around $\alpha_0 = -8^\circ$ at $Re = 1 \times 10^6$ and $Re = 2 \times 10^6$

The analysis of negative stall phenomena yields insights that, although less encouraging than those observed in positive stall, contribute to a deeper understanding of this complex phenomenon and provide avenues for improving modeling techniques.

In line with the positive stall analysis, Figure 7.3a and Figure 7.4a depict the hysteresis parameter for both Reynolds numbers. Experimental data exhibits a clear linear increase, a trend captured by both models. Notably, the BL model demonstrates superiority in hysteresis loop size, with differences ranging from 0.1 to 0.035 compared to 0.265 to 0.22 for  $Re = 1 \times 10^6$ .

At higher Reynolds numbers, the linear nature of the hysteresis parameter persists, but with larger deviations between the models and the data. For the BL model, the difference with experimental hysteresis ranges from 0.19 to 0.086 across the frequency range, while the Snel model performs even worse with differences between 0.275 and 0.272.

The poor hysteresis loop modeling can be attributed to two main factors present in both models: the overestimation of  $C_N$  during the upstroke motion and the consequential shift in stall onset AoA.

At  $Re = 1 \times 10^6$ , the BL model can predict the stall onset relatively well, with the largest difference of  $\Delta\alpha_{st} = 1.55^\circ$  at  $f = 0.6Hz$ . This discrepancy gradually decreases with increasing frequency, with the stall onset even lagging behind the experimental one by  $\Delta\alpha_{st} = 0.27^\circ$  at the highest frequency.

However, the shift in dynamic stall onset becomes more severe with increasing Reynolds number. The BL model overpredicts the dynamic stall onset and slope, with discrepancies ranging from  $\Delta\alpha_{st} = 2.71^\circ$  to  $\Delta\alpha_{st} = 1.63^\circ$  across the studied frequency range.

On the other hand, the Snel model underperforms under negative stall conditions, with delayed dynamic stall ranging from  $\Delta\alpha_{st} = 6.3^\circ$  to  $\Delta\alpha_{st} = 1^\circ$  at  $Re = 1 \times 10^6$  compared to the experimental data. The increase in Reynolds number increases this delay at higher frequency range, with differences varying from  $\Delta\alpha_{st} = 5.18^\circ$  to  $\Delta\alpha_{st} = 4.13^\circ$ .

The analysis incorporating the reattachment parameter reveals satisfactory results for both models across all considered cases. At lower Reynolds numbers, similarities in reattachment parameter values are observed between the two models. However, both models consistently underpredict the actual values throughout the frequency range. This underestimation is particularly pronounced at higher frequencies, where reattachment occurs only towards the end of the hysteresis cycle.

The early occurrence of boundary layer reattachment may be attributed to various factors. In the case of the BL model, the absence of the leading vortex effect during the upstroke motion could contribute to this effect. Similarly, the Snel model's inaccurate prediction of trailing vortex development during the upstroke may amplify the effect.

Despite the overpredictions described above, the BL model can correctly predict the overall shape of the hysteresis loop at negative stall for all cases. Severity of the  $C_N$  coefficient drop after the dynamic stall onset angle as well as the downstroke motion matches the experimental data in term of general shape. The Snel model, on the other hand, due to the strongly delayed stall onset experience a sudden, in some cases almost instantaneous, drop of the  $C_N$ . This might have a significant effect on the fatigue loads modeling and requires the model to properly adapt for the negative stall features.

The L2-norm comparison for two Reynolds numbers is depicted in Figure 7.11 and Figure 7.12.

A discernible pattern emerges across both Reynolds numbers. As frequency increases for all studied amplitude values, both models exhibit improved performance. However, this trend is more pronounced at  $Re = 2 \times 10^6$ . Interestingly, as the Reynolds number increases, both models generally exhibit worse performance compared to the reverse behavior observed for positive stall.

Specifically, the BL model demonstrates slightly better agreement with experimental data at lower amplitudes, but its performance deteriorates as amplitude increases. This discrepancy is particularly evident when examining L2-norm values at  $f = 0.6$  for each amplitude. Conversely, the Snel model shows only marginal improvement with increasing amplitude, with this improvement becoming negligible at  $Re = 2 \times 10^6$ .

In summary, in contrast to positive stall, it is evident that both models are not fully suited for negative stall. Further modifications and improvements are necessary to incorporate all complex phenomena and achieve satisfactory results.

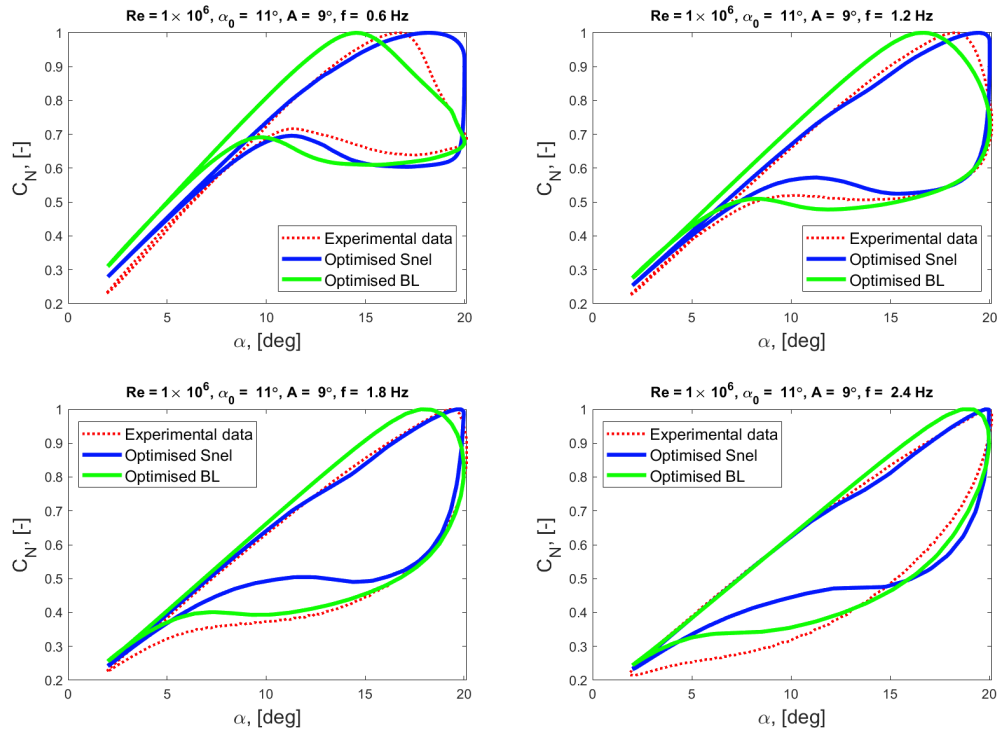


**Figure 7.1:** Comparison of the optimized and default Snel model with experimental data for  $Re = 1 \times 10^6$ ,  $\alpha_0 = 11^\circ$ ,  $A = 9^\circ$ .

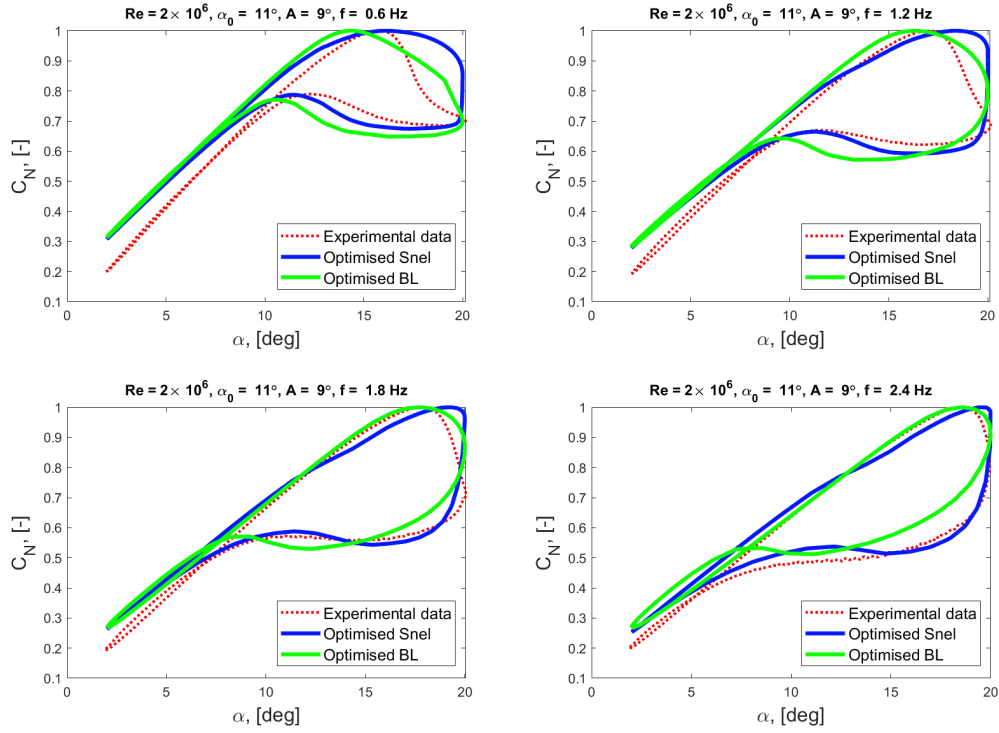
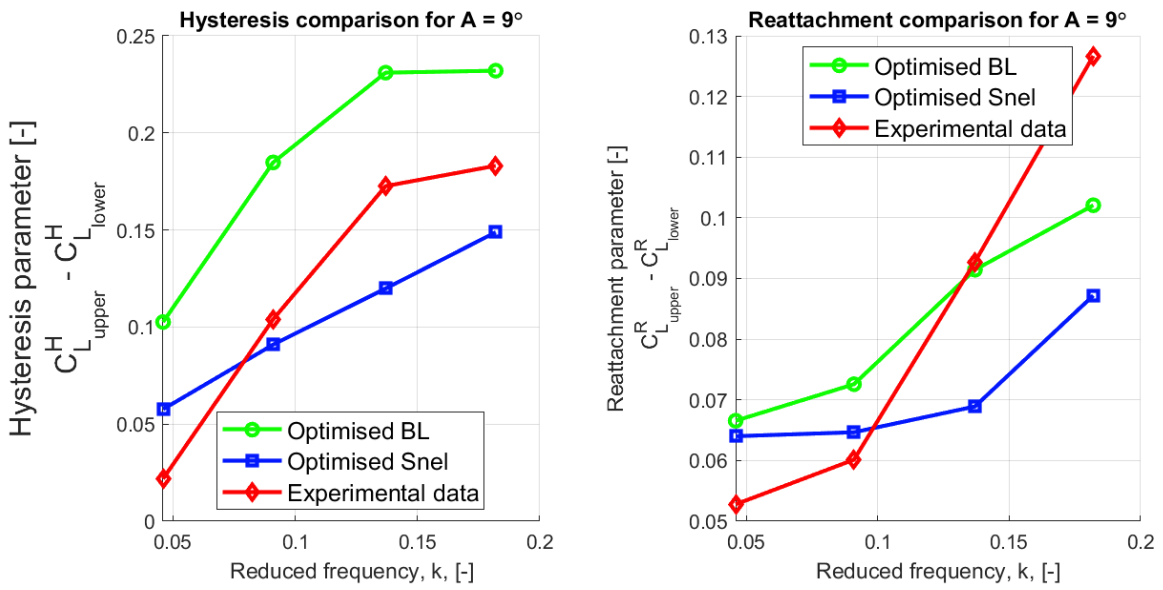


Figure 7.2: Comparison of the optimized and default Snel model with experimental data for  $Re = 2 \times 10^6$ ,  $\alpha_0 = 11^\circ$ ,  $A = 9^\circ$ .



(a) Hysteresis parameter,  $\alpha_0 = 11^\circ$ ,  $Re = 1 \times 10^6$

(b) Reattachment parameter,  $\alpha_0 = 11^\circ$ ,  $Re = 1 \times 10^6$

Figure 7.3: Comparison of hysteresis and reattachment parameters for  $Re = 1 \times 10^6$ ,  $A = 9^\circ$

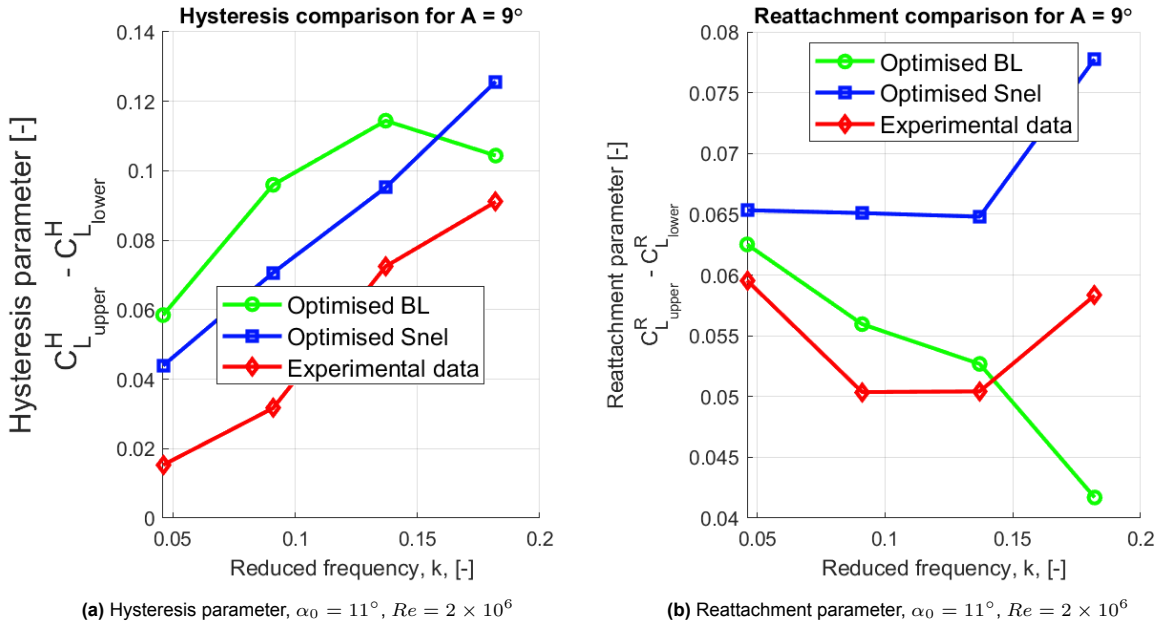


**Figure 7.4:** Comparison of hysteresis and reattachment parameters for  $Re = 2 \times 10^6$ ,  $A = 9^\circ$

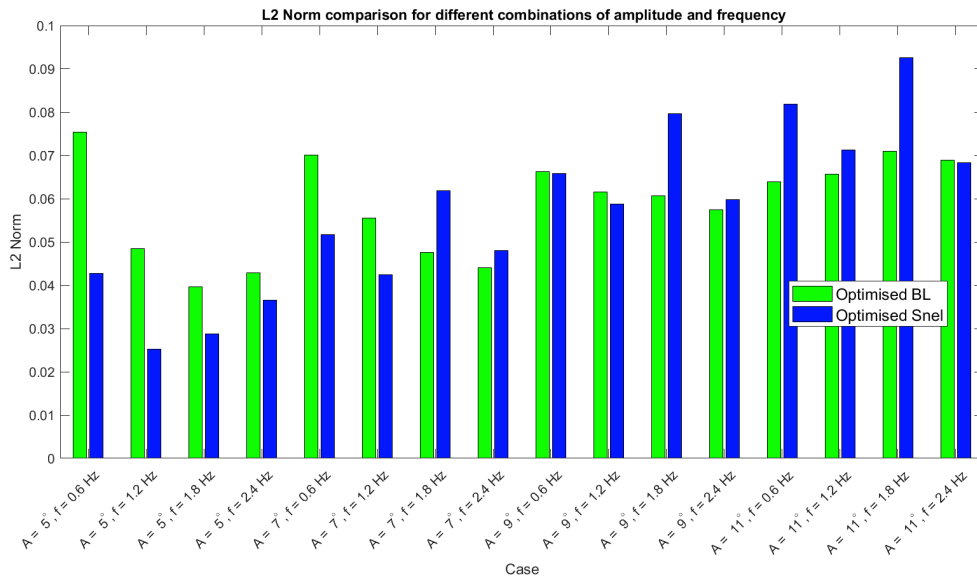


**Figure 7.5:** L2 parameter comparison for  $\alpha_0 = 11^\circ$ ,  $Re = 1 \times 10^6$

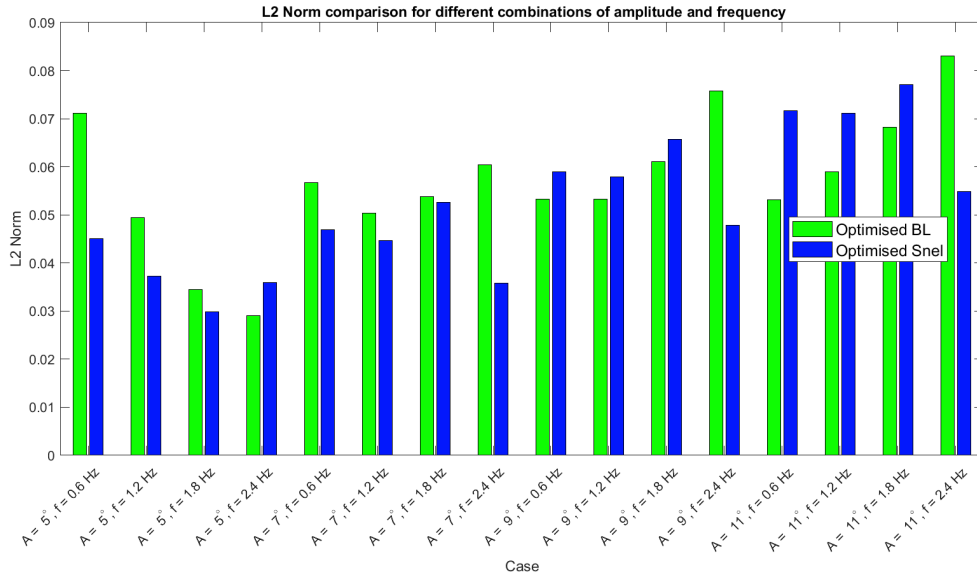


Figure 7.6: L2 parameter comparison for  $\alpha_0 = 11^\circ$ ,  $Re = 2 \times 10^6$

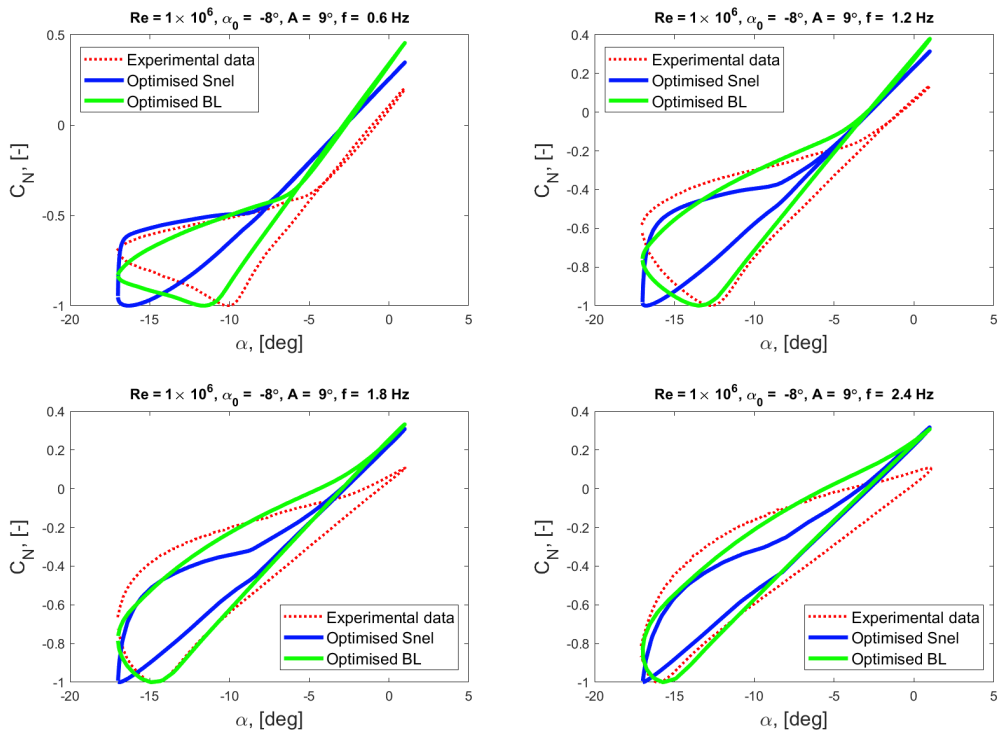
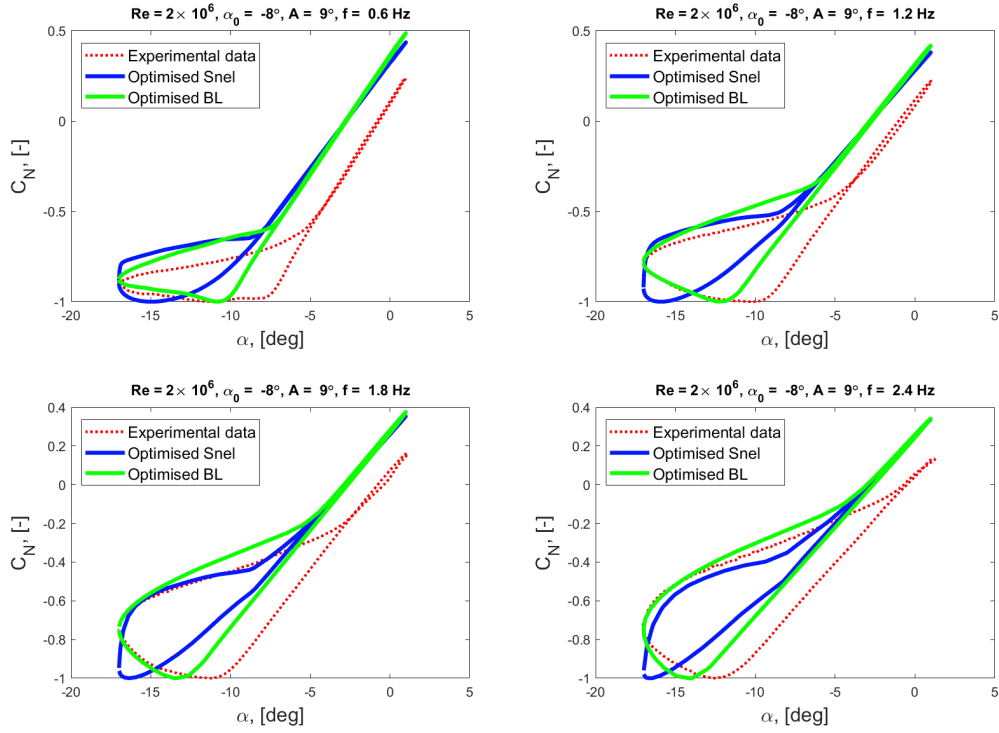
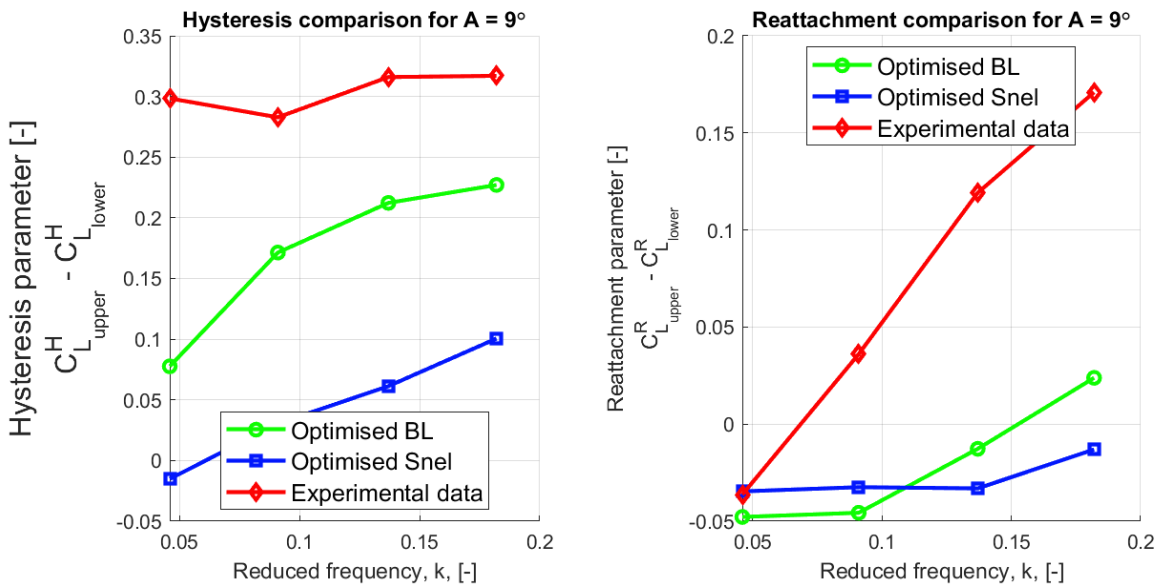


Figure 7.7: Optimized and default Snel models comparison with experimental data for  $Re = 1 \times 10^6$ ,  $\alpha_0 = -8^\circ$ ,  $A = 9^\circ$ .



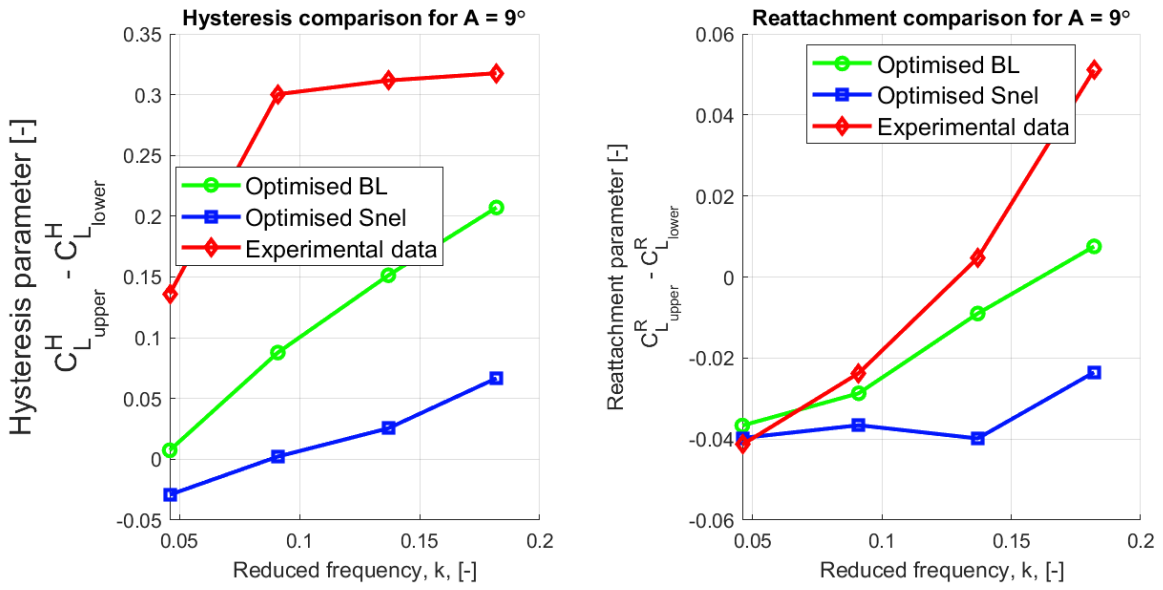
**Figure 7.8:** Optimized and default Snel models comparison with experimental data for  $Re = 2 \times 10^6$ ,  $\alpha_0 = -8^\circ$ ,  $A = 9^\circ$ .



**(a)** Hysteresis parameter,  $\alpha_0 = -8^\circ$ ,  $Re = 1 \times 10^6$

**(b)** Reattachment parameter,  $\alpha_0 = -8^\circ$ ,  $Re = 1 \times 10^6$

**Figure 7.9:** Comparison of hysteresis and reattachment parameters for  $Re = 1 \times 10^6$ ,  $A = 9^\circ$



(a) Hysteresis parameter,  $\alpha_0 = -8^\circ$ ,  $Re = 2 \times 10^6$

(b) Reattachment parameter,  $\alpha_0 = -8^\circ$ ,  $Re = 2 \times 10^6$

**Figure 7.10:** Comparison of hysteresis and reattachment parameters for  $Re = 2 \times 10^6$ ,  $A = 9^\circ$

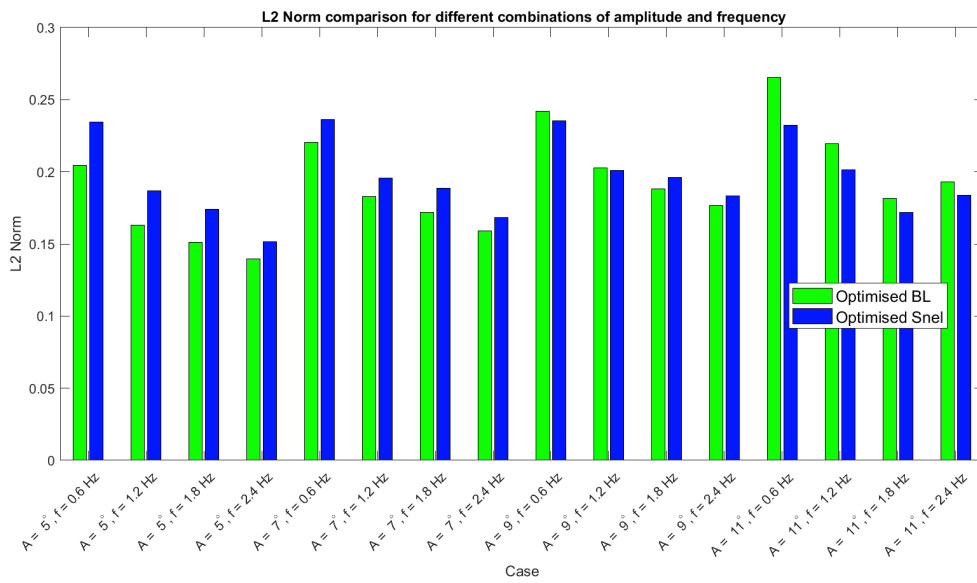


**Figure 7.11:** L2 parameter comparison for  $\alpha_0 = -8^\circ$ ,  $Re = 1 \times 10^6$

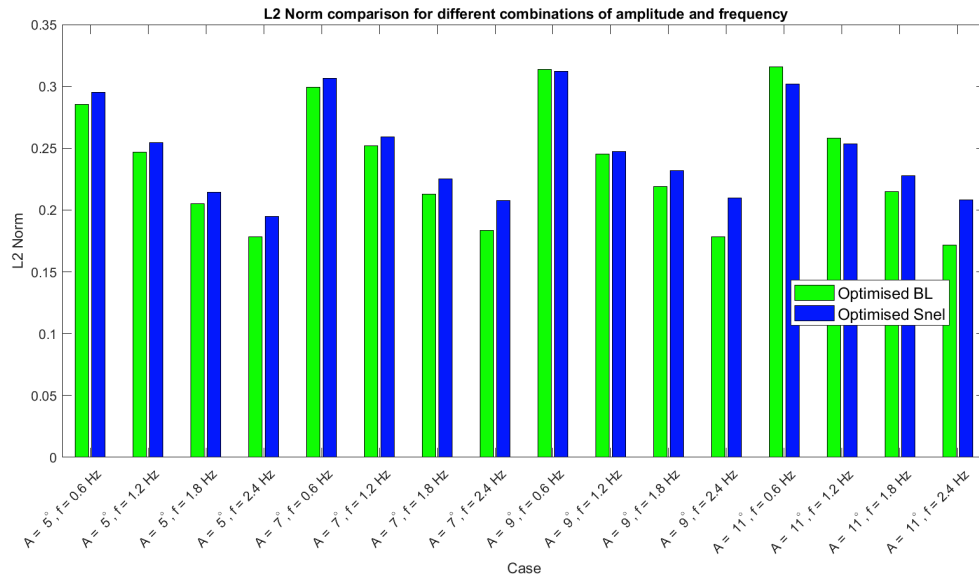
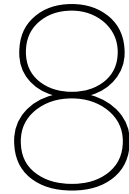


Figure 7.12: L2 parameter comparison for  $\alpha_0 = -8^\circ$ ,  $Re = 2 \times 10^6$



# Conclusions and Further work

This chapter will discuss the results obtained during the research. First, the comparison between the default models and the optimized models will be evaluated. Then, the optimized models will be compared with each other. In addition, potential directions for future research will be provided.

## 8.1. Evaluation of the Beddoes-Leishman model results

Comparison between the default and optimized models was conducted in Chapter 5. It is evident that the optimized model significantly outperforms the default one in almost all studied cases. The optimization routine adopted in this research differs from the typical Beddoes-Leishman model optimization reported in the literature. Here, the shape-based coefficients were included in the model optimization. Upon analyzing the results, it is found that the values of these coefficients play a significant role in modeling dynamic stall. The greatest influence is found on the boundary layer reattachment point. When optimizing only time delay-based coefficients, the modeling of the hysteresis loop at small angles of attack is significantly degraded. This discrepancy is particularly evident in the appearance of secondary loops in the  $C_N$  coefficient during boundary layer reattachment. Additionally, non-optimized values of these parameters affect the width of the cycle, which is particularly pronounced at high values of reduced frequency of oscillation.

One of the shortcomings of the model is the overestimation of the normal force coefficient values throughout the entire range of angles of attack during the upstroke. The same overestimation is observed in the second half of the downstroke motion for most studied cases. Furthermore, it is found that for positive dynamic stall, this model performs best in the range of medium frequency oscillations, in the region of  $f = 1.2$  Hz and  $f = 1.8$  Hz. Lower frequencies are accompanied by a greater overestimation of values during the upstroke, whereas higher frequencies predict larger values during the downstroke.

Optimizing the model in cases of negative stall also significantly improved the model's performance. It allowed for a significant improvement in modeling the width of the hysteresis loop, indicating the degree of unsteadiness of the flow during this event, as well as the behavior of  $C_N$  after dynamic stall onset. The default model predicts a more linear behavior, which can significantly affect load predictions and fatigue life. Additionally, the optimised model significantly improves its behavior during boundary layer reattachment. A major drawback of the model in modeling negative stall is the lack of formation and movement of the leading edge vortex during the upstroke motion, which is an important factor in studying dynamic aeroelastic problems and dynamic loading on turbine blades.

An effect of Reynolds number on the predictive ability of the model is also observed. For positive stall, increasing the Reynolds number slightly worsens the model's performance in modeling the size of the hysteresis loop. However, characteristics such as reattachment parameter or dynamic stall onset AoA are predicted more accurately with increasing Reynolds number.

Increasing the Reynolds number for negative stall has a dual effect. On one hand, the overall fit of the model also slightly worsens, which is associated with an exaggeration of the stall onset AoA. However, on the other hand, with increasing Reynolds number, the effect of the leading edge vortex significantly decreases. The absence of a pronounced influence during the upstroke allows the optimized Beddoes-Leishman model to predict the overall hysteresis force with sufficient accuracy, albeit with larger  $C_N$  values compared to lower Reynolds numbers.

## 8.2. Evaluation of the Snel model results

Snel model optimization results are presented in Chapter 6. It is evident that the model optimization significantly improved the model's performance. During the model development, it is noted that the standard model incorrectly predicts the tilt of the  $C_N$  coefficient during the upstroke motion. However, it is found during the model optimization process that adjusting the coefficients can significantly improve this parameter. Additionally, it is discovered that this model fails to predict minor secondary loops during boundary layer reattachment. This behavior is observed in all relevant cases, leading the model to predict an earlier reattachment moment than experimental data.

When studying positive stall, both strengths and weaknesses of the model were observed. The selected coefficients allowed control over the model's behavior. This improvement led to better behavior of the  $C_N$  drop after the onset of dynamic stall. Compared to the standard model, optimization significantly improved the upstroke and the first half of the downstroke motion. However, the second half of the downstroke motion consistently exaggerates the hysteresis values, maintaining a sharper  $C_N$  behavior during boundary layer reattachment. On one hand, this results in more accurate modeling at lower reduced frequencies. On the other hand, this model feature exaggerates the drop in normal force and reattachment speed after the onset of dynamic stall for cases with higher oscillation frequencies. However, it should be noted that significant differences due to this characteristic are more pronounced at  $Re = 1 \times 10^6$ . With increasing Reynolds number, experimental data also exhibit similar behavior, and the described model drawback becomes its advantage. This can be observed in significantly improved hysteresis and reattachment parameter predictions at  $Re = 2 \times 10^6$ . Considering that wind turbines operate at significantly higher Reynolds numbers, this feature may positively impact dynamic stall modeling for real operational conditions.

Modeling negative dynamic stall using this model revealed that this area is a weak point of the model. Both the standard and optimized models fail to accurately reproduce the hysteresis loop, significantly reducing its size. This is associated with a critical flaw found in the model. During the upstroke motion, the model predicts the formation of a trailing edge vortex. This effect is noticeable by the change in the  $C_N$  slope angle during upstroke motion compared to experimental data, where the leading edge vortex effect is clearly visible. This fact negatively affects all cycle parameters, especially the dynamic stall onset AoA. A too late onset of dynamic stall leads to a sharp drop in the normal force coefficient. This fact may contribute to incorrect structural analysis results. Compared to the default model, which in some cases did not predict flow reattachment at all, the optimized model results in significantly earlier and sharper flow reattachment processes.

## 8.3. Evaluation of model comparison results

Based on the analysis, it is challenging to definitively conclude whether one model is superior to the other for the positive dynamic stall modeling. Both of them have their strengths and weaknesses under different operational conditions.

For positive dynamic stall at  $Re = 1 \times 10^6$ , the Snel model accurately reproduces the  $C_N$  slope for all cases considered. This feature allows it to outperform the BL model at amplitudes  $A = 5^\circ$  and  $A = 7^\circ$ . However, as the amplitude and frequency increase, the BL model consistently performs better at modeling the level of unsteadiness, more accurately predicting the severity of the hysteresis. This model's characteristic contributes to high performance at amplitudes  $A = 9^\circ$  and above. One of the drawbacks

of the BL model at the considered Reynolds number is the consistent underestimation of dynamic stall onset. The Snel model, on the other hand, accurately predicts this parameter, especially for  $f = 1.8$  Hz and  $f = 2.4$  Hz across all amplitudes. The reattachment zone is almost identical between the two models in the considered case.

With an increase in Reynolds number to  $2 \times 10^6$ , it is observed that both models overestimate the minimum  $C_N$  values, leading to incorrect determination of the  $C_N$  slope and, consequently, inaccurate prediction of dynamic stall onset: underestimation for the BL model and overestimation for the Snel model. As described earlier, with an increase in Reynolds number, the Snel model accurately predicts the hysteresis loop size and overall shape, with even greater accuracy with increasing oscillation frequency. Conversely, the BL model begins to miss nuances in the hysteresis, negatively affecting the modeling of high-frequency oscillations, especially at high amplitudes. Another advantage of the Snel model is its more accurate modeling of the  $C_N$  drop after stall. However, in some cases, due to the delayed onset of dynamic stall, this drop can be excessively sharp. The BL model predicts a smoother hysteresis than reality. The BL model also has an advantage in predicting secondary smaller loops at low AoA's, which the Snel model is incapable of, thus improving reattachment parameter values.

When considering cases of negative dynamic stall, it is evident that the Beddoes-Leishman model possesses superior predictive capabilities. However, both the Snel and BL models require additional modifications for accurate modeling at these angles of attack.

The main reason for the inaccurate modeling of negative dynamic stall in both models is the absence of the leading-edge vortex effect during the upstroke motion. However, while the BL model simply does not detect any effects and maintains linear behavior of  $C_N$ , the Snel model experiences the opposite effect of a trailing-edge vortex, contrary to reality. A common issue with both models is the exaggeration of the maximum normal force value throughout the entire upstroke motion in all cases studied. Consequently, this leads to overprediction in dynamic stall onset angle, especially severe for the Snel model. For the same reasons, both models predict reattachment earlier than it actually occurs.

The Reynolds number effect is less noticeable than in positive stall cases. At  $Re = 2 \times 10^6$ , the prediction of the stall onset angle deteriorates further, resulting in a sharper  $C_N$  jump. Despite this, the first half of the downstroke motion improves for both models, showing close agreement with experimental data in this small interval. Differences between the models are observed in predicting the hysteresis loop size. It is noticed that the BL model consistently overpredicts the values in all considered cases. The Snel model also overpredicts initially, but with increasing oscillation frequency, the values decrease, and at the maximum frequency of  $f = 2.4$  Hz, the model underpredicts the hysteresis. It is also observed that the amplitude values do not significantly influence this effect for the Snel model, while increasing the oscillation amplitude brings the downstroke motion hysteresis values of the BL model closer to experimental values.

The reattachment zone, although not ideal, is predicted with fairly high accuracy by both models. In all considered cases, boundary layer reattachment occurs earlier than in the experimental data. Additionally, both models capture the general trend of increasing reattachment parameter with increasing frequency.

## 8.4. Further research

Based on the information obtained in this report, several areas of potential further research are identified. These suggestions are grouped according to the directions of the activity and are presented below:

- **Wind tunnel dynamic polars corrections**

As noted, experiments in wind tunnels are an integral part of studying complex aerodynamic parameters. Having precise experimental data can significantly aid in understanding physical processes and developing more accurate models. Experiments to collect dynamic polars in wind

tunnels are accompanied by some distortions due to the physical limitations of the tunnel test sections. Currently, there is a gap in the literature regarding the necessary corrections to apply to the obtained data to approximate them to real values.

- **Additional data**

In this study, an experiment is conducted, and dynamic polars for the FFA-W2-211 airfoil are obtained. However, the amount of data obtained is limited by the physical constraints of the LLT wind tunnel experimental setup. Data at higher Reynolds numbers, amplitudes, and frequencies will help in developing new and upgrading existing models.

Negative stall is a poorly studied but a key area for wind energy. Further data collection for other airfoils used in wind turbines will contribute to optimizing models and providing more accurate predictions.

- **Beddoes-Leishman model further research**

The Beddoes-Leishman model remains a widely used tool for assessing unsteady aerodynamics in wind energy. However, from the results obtained, it can be concluded that this tool requires additional modifications to increase prediction accuracy.

One of the model's problems for all cases studied is the exaggeration of the normal force during the upstroke. Modifications in the attached flow block of the model can significantly improve this drawback. Additionally, a modification of the stall onset criteria could be an important enhancement to more accurately predict the onset of dynamic stall and the model's behavior during downstroke motion.

Another direction for work with this model is a deeper study of shape-based coefficients and their relationship with hysteresis characteristics and the geometry of different airfoils. Sensitivity analysis and checking the robustness of the model compared to other airfoil data will provide a more detailed understanding of their influence and interaction.

Additionally, a significant addition to the model would be a modification to predict the leading-edge vortex effect during negative stall. Successfully introducing and validating this feature could make the Beddoes-Leishman model even more valuable.

- **Snel model further research**

Similar recommendations are proposed for working with the Snel model. The model is capable of accurately predicting dynamic stall, but it has some drawbacks that limit its abilities.

One such drawback is the prediction of dynamic stall onset AoA. By adding correct indicators of stall onset, even better behavior in the post-stall region can be achieved, which is especially relevant for low-frequency oscillations.

Of particular concern is negative stall. As shown, the model makes a serious mistake during upstroke motion by predicting the trailing edge effect instead of the leading edge vortex. Eliminating this drawback will significantly improve the predictions of hysteresis size and the onset of stall for negative mean angles. Similar to BL, the Snel model often exaggerates  $C_N$  values, especially during negative stall. Modifying this behavior will contribute to modeling both hysteresis and reattachment parameters.

- **Further research on the turbine level**

This study focuses on the airfoil level, but as known, the models studied here are used in software that models the whole wind turbine behavior. Potential research directions could include investigating optimized models on turbine response in software such as OpenFAST, where basic versions of the models studied in this work are applied. Research in this area can deepen the understanding of the impact of optimized coefficients on turbine energy production, as well as on loads, fatigue life, and other turbine parameters. Turbine instabilities experienced when using optimized models could also be an interesting research topic.

- **Other dynamic stall models**

This study focused on two models. However, there are other models, such as Risø (M. H. Hansen et al., 2004), Øye (Oye, 1991), ONERA (Mohamed & Wood, 2021), IAG (Bangga et al., 2023), and others. Comparing the results of other models, as well as optimizing them, is also highly desirable for further research.

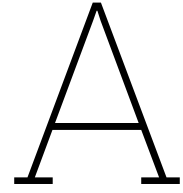
# References

- Abdallah, I., Natarajan, A., & Sørensen, J. (2015). Impact of uncertainty in airfoil characteristics on wind turbine extreme loads. *Renewable Energy*, 75, 283–300. <https://doi.org/10.1016/j.renene.2014.10.009>
- Adema, N., Kloosterman, M., & Schepers, G. (2020). Development of a second-order dynamic stall model. *Wind Energy Science*, 5(2), 577–590. <https://doi.org/10.5194/wes-5-577-2020>
- Bangga, G., Parkinson, S., & Collier, W. (2023). Development and validation of the iag dynamic stall model in state-space representation for wind turbine airfoils. *Energies*, 16(10), 3994.
- Beddoes, T. (1982). Practical computation of unsteady lift (2nd ed.). 7.
- Bertagnolio, F., Sørensen, N., Johansen, J., & Fuglsang, P. (2001). Wind turbine airfoil catalogue.
- Bešlagić, E., Lemeš, S., & Hadžikadunić, F. (2020). Procedure for determining the wind tunnel blockage correction factor. *New Technologies, Development and Application III* 6, 331–339.
- Bjoerck, A. (1997). The ffa dynamic stall model. the beddoes-leishman dynamic stall model modified for lead-lag oscillations.
- Boutet, J., Dimitriadis, G., & Amandolese, X. (2020). A modified leishman-beddoes model for airfoil sections undergoing dynamic stall at low reynolds numbers. *Journal of Fluids and Structures*, 93, 102852.
- Butterfield, C. P., Simms, D., Scott, G., & Hansen, A. C. (1991). Dynamic stall on wind turbine blades. <https://www.osti.gov/biblio/10103796>
- Carr, L. W. (1985). Dynamic stall progress in analysis and prediction. *12th Atmospheric Flight Mechanics Conference*. <https://doi.org/10.2514/6.1985-1769>
- Carr, L. W., & Chandrasekhara, M. (1996). Compressibility effects on dynamic stall. *Progress in Aerospace Sciences*, 32(6), 523–573. [https://doi.org/https://doi.org/10.1016/0376-0421\(95\)00009-7](https://doi.org/https://doi.org/10.1016/0376-0421(95)00009-7)
- Chellini, S., De Tavenier, D., & von Terzi, D. (2023, July). *The experimental characterisation of dynamic stall of the FFA-W3-211 wind turbine Airfoil* (tech. rep.). Delft University of Technology.
- Corke, T. C., & Thomas, F. O. (2015). Dynamic stall in pitching airfoils: Aerodynamic damping and compressibility effects. *Annual Review of Fluid Mechanics*, 47, 479–505.
- Dai, J., Hu, Y., Liu, D., & Long, X. (2011). Aerodynamic loads calculation and analysis for large scale wind turbine based on combining bem modified theory with dynamic stall model. *Renewable Energy*, 36(3), 1095–1104. <https://doi.org/https://doi.org/10.1016/j.renene.2010.08.024>
- De Tavernier, D., & Von Terzi, D. (2022). The emergence of supersonic flow on wind turbines. *Journal of Physics: Conference Series*, 2265(4), 042068.
- Ericsson, L. E., & Reding, J. P. (1984). Unsteady flow concepts for dynamic stall analysis. *Journal of Aircraft*, 21(8), 601–606. <https://doi.org/10.2514/3.45029>
- Ericsson, L. E., & Reding, J. P. (1972). Dynamic stall of helicopter blades. *Journal of the American Helicopter Society*, 17(1), 11–19. <https://doi.org/10.4050/jahs.17.11>
- Ericsson, L. E., & Reding, J. P. (1980). Dynamic stall at high frequency and large amplitude. *Journal of Aircraft*, 17(3), 136–142. <https://doi.org/10.2514/3.57884>
- Faber, M. (2018). A comparison of dynamic stall models and their effect on instabilities.
- Ferreira, C. S., Bijl, H., van Bussel, G., & Van Kuik, G. (2007). Simulating dynamic stall in a 2d vawt: Modeling strategy, verification and validation with particle image velocimetry data. *Journal of physics: conference series*, 75(1), 012023.
- Gaertner, E., Rinker, J., Sethuraman, L., Zahle, F., Anderson, B., Barter, G. E., Abbas, N. J., Meng, F., Bortolotti, P., Skrzypinski, W., et al. (2020). *Iea wind tcp task 37: Definition of the iea 15-megawatt offshore reference wind turbine* (tech. rep.). National Renewable Energy Lab.(NREL), Golden, CO (United States).
- Green, R., & Galbraith, R. M. (1994). Phenomena observed during aerofoil ramp-down motions from the fully separated state. *The Aeronautical Journal*, 98(979), 349–356.
- Gupta, S., & Leishman, J. G. (2006). Dynamic stall modelling of the s809 aerofoil and comparison with experiments. *Wind Energy*, 9(6), 521–547. <https://doi.org/https://doi.org/10.1002/we.200>

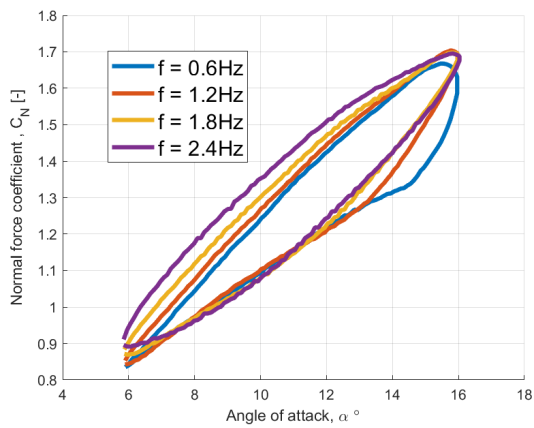
- Halfman, R. L., Johnson, H., & Haley, S. (1951). *Evaluation of high-angle attack aerodynamic-derivative data and stall-flutter prediction techniques* (tech. rep.).
- Handbook of Wind Energy Aerodynamics*. (2022, January). <https://doi.org/10.1007/978-3-030-31307-4>
- Hansen, M. H. (2007). Aeroelastic instability problems for wind turbines. *Wind Energy*, 10(6), 551–577. <https://doi.org/10.1002/we.242>
- Hansen, M. O. L., Sørensen, J. N., Voutsinas, S., Sørensen, N., & Madsen, H. A. (2006). State of the art in wind turbine aerodynamics and aeroelasticity. *Progress in aerospace sciences*, 42(4), 285–330.
- Hansen, M. H., Gaunaa, M., & Aagaard Madsen, H. (2004). A beddoes-leishman type dynamic stall model in state-space and indicial formulations [wind turbines].
- Hibbs, B. D. (1986). Hawt performance with dynamic stall. <https://doi.org/10.2172/5509059>
- IEA. (2020). *Energy Policy Review The Netherlands 2020* (tech. rep.). [https://iea.blob.core.windows.net/assets/93f03b36-64a9-4366-9d5f-0261d73d68b3/The\\_Netherlands\\_2020\\_Energy\\_Policy\\_Review.pdf](https://iea.blob.core.windows.net/assets/93f03b36-64a9-4366-9d5f-0261d73d68b3/The_Netherlands_2020_Energy_Policy_Review.pdf)
- IRENA. (2018). Renewable electricity capacity and generation statistics.
- Irena – international renewable energy agency*. (2024, May 1). <https://www.irena.org/>
- Johnson, W., & Ham, N. D. (1972). On the mechanism of dynamic stall. *Journal of the American Helicopter Society*, 17(4), 36–45. <https://doi.org/10.4050/jahs.17.36>
- Kim, Y., & Xie, Z.-T. (2016). Modelling the effect of freestream turbulence on dynamic stall of wind turbine blades. *Computers & Fluids*, 129, 53–66.
- Laneville, A., & Vittecoq, P. (1985, May). *Effect of turbulence on dynamic stall* (tech. rep.). Sandia National Laboratories, Albuquerque, NM.
- Lantz, E. J., Roberts, J. O., Nunemaker, J., DeMeo, E., Dykes, K. L., & Scott, G. N. (2019). Increasing wind turbine tower heights: Opportunities and challenges.
- Leishman, J. G. (2002). Challenges in modelling the unsteady aerodynamics of wind turbines. *Wind Energy: An International Journal for Progress and Applications in Wind Power Conversion Technology*, 5(2-3), 85–132.
- Leishman, J. G., & Beddoes, T. (1989). A semi-empirical model for dynamic stall. *Journal of the American Helicopter society*, 34(3), 3–17.
- Leishman, J. (1990). Dynamic stall experiments on the naca 23012 aerofoil. *Experiments in Fluids*, 9(1), 49–58.
- Leishman, J., & Beddoes, T. (1986). A generalised model for airfoil unsteady aerodynamic behaviour and dynamic stall using the indicial method. *Proceedings of the 42nd Annual forum of the American Helicopter Society*, 34, 3–17.
- Liu, X., Liang, S., Li, G., Godbole, A., & Lu, C. (2020). An improved dynamic stall model and its effect on wind turbine fatigue load prediction. *Renewable energy*, 156, 117–130.
- Liu, Y., Li, K., Zhang, J., Wang, H., & Liu, L. (2012). Numerical bifurcation analysis of static stall of airfoil and dynamic stall under unsteady perturbation. *Communications in Nonlinear Science and Numerical Simulation*, 17(8), 3427–3434. <https://doi.org/https://doi.org/10.1016/j.cnsns.2011.12.007>
- Mallik, W., & Raveh, D. E. (2020). Aerodynamic damping investigations of light dynamic stall on a pitching airfoil via modal analysis. *Journal of Fluids and Structures*, 98, 103111.
- McAlister, K. W., & Carr, L. W. (1979). Water Tunnel Visualizations of Dynamic Stall. *Journal of Fluids Engineering*, 101(3), 376–380. <https://doi.org/10.1115/1.3448981>
- McAlister, K. W., Carr, L. W., & McCroskey, W. J. (1978). *Dynamic stall experiments on the naca 0012 airfoil* (tech. rep.).
- McCroskey, W. J. (1981). The phenomenon of dynamic stall.
- McCroskey, W. J., McAlister, K. W., Carr, L. W., & Pucci, S. (1982). *An experimental study of dynamic stall on advanced airfoil sections. volume 1: Summary of the experiment* (tech. rep.).
- Mohamed, A., & Wood, D. H. (2021). Modeling dynamic loads on oscillating airfoils with emphasis on dynamic stall vortices. *Wind Energy*, 24(11), 1225–1248.
- Montgomerie, B. (1996). Dynamic stall model called simple.
- Muljadi, E., Pierce, K., & Migliore, P. (2000). Soft-stall control for variable-speed stall-regulated wind turbines. *Journal of Wind Engineering and Industrial Aerodynamics*, 85(3), 277–291. [https://doi.org/https://doi.org/10.1016/S0167-6105\(99\)00130-0](https://doi.org/https://doi.org/10.1016/S0167-6105(99)00130-0)

- Noll, R. B., & Ham, N. D. (1982). Effects of dynamic stall on swecs. *Journal of Solar Energy Engineering*, 104(2), 96–101. <https://doi.org/10.1115/1.3266292>
- Noll, R., Ham, N., Drees, H., & Nichol, L. (1982). *1-kilowatt high-reliability wind system development phase i - design and analysis* (tech. rep.).
- Noll, R. B., & Ham, N. D. (1980). Analytical evaluation of the aerodynamic performance of a high-reliability vertical-axis wind turbine. *American Wind Energy Association*, 106–113.
- NREL. (2009, February). *Definition of a 5-MW reference wind turbine for offshore system development* (tech. rep.). <https://www.nrel.gov/docs/fy09osti/38060.pdf>
- Ormiston, R. A., & Bousman, W. G. (1975). A study of stall-induced flap instability of hingeless rotors. *Journal of the American Helicopter Society*, 20(1), 20–30. <https://doi.org/doi:10.4050/JAHS.20.20>
- Oye, S. O. (1991). *Dynamic stall simulated as time lag of separation*.
- Pierce, K., & Hansen, A. C. (1995). Prediction of Wind Turbine Rotor Loads Using the Beddoes-Leishman Model for Dynamic Stall. *Journal of Solar Energy Engineering*, 117(3), 200–204. <https://doi.org/10.1115/1.2847783>
- RB, N., & ND, H. (1982). Effects of dynamic stall on swecs.
- Rice, T. T., Taylor, K., & Amitay, M. (2019). Wind tunnel quantification of dynamic stall on an s817 airfoil and its control using synthetic jet actuators. *Wind Energy*, 22(1), 21–33.
- Rinker, J., Dykes, K., & Laboratory, N. R. E. (2018, April). *WindPACT reference wind turbines* (tech. rep. No. NREL/TP-5000-67667). National Renewable Energy Laboratory. <https://www.nrel.gov/docs/fy18osti/67667.pdf>
- Schepers, J., & Snel, H. (2007). Model experiments in controlled conditions. *ECN Report: ECN-E-07-042*, 484.
- Sheng, W., Galbraith, R. A. M., & Coton, F. N. (2008). A Modified Dynamic Stall Model for Low Mach Numbers. *Journal of Solar Energy Engineering*, 130(3), 031013. <https://doi.org/10.1115/1.2931509>
- Shyu, L.-S., & Chuang, S.-H. (2008). Investigation of model wake blockage effects at high angles of attack in low-speed wind tunnel. *Transactions of the Japan Society for Aeronautical and Space Sciences*, 51(171), 37–42.
- Singapore Wala, A. A., Ng, E. Y., & Narasimalu, S. (2018). A beddoes-leishman type model with an optimization-based methodology and airfoil shape parameters. *Wind Energy*, 21(7), 590–603.
- Snel, H. (1997). Heuristic modelling of dynamic stall characteristics. *EWEC-CONFERENCE*, 429–433.
- Spentzos, A., Barakos, G., Badcock, K., Richards, B., Wernert, P., Schreck, S., & Raffel, M. (2004). Cfd investigation of 2d and 3d dynamic stall. *AHS International 4th Decennial Specialists' Conference on Aeromechanics*.
- Spentzos, A., Barakos, G., Badcock, K., Richards, B., Wernert, P., Schreck, S., & Raffel, M. (2005). Investigation of three-dimensional dynamic stall using computational fluid dynamics. *AIAA Journal*, 43(5), 1023–1033. <https://doi.org/10.2514/1.8830>
- Terra, W., Sciacchitano, A., Scarano, F., & van Oudheusden, B. (2018). Drag resolution of a piv wake rake for transiting models. *Experiments in Fluids*, 59, 1–6.
- The DTU 10-MW reference wind turbine*. (2013). [https://backend.orbit.dtu.dk/ws/portalfiles/portal/55645274/The\\_DTU\\_10MW\\_Reference\\_Turbine\\_Christian\\_Bak.pdf](https://backend.orbit.dtu.dk/ws/portalfiles/portal/55645274/The_DTU_10MW_Reference_Turbine_Christian_Bak.pdf)
- Timmer, W. (2008). Two-dimensional low-reynolds number wind tunnel results for airfoil naca 0018. *Wind engineering*, 32(6), 525–537.
- Timmer, W. (2014, June 14). *Procedure for measurements in the delft university low-speed wind tunnel with determination of the lift coefficient by means of the wall pressures method*. TU Delft.
- Tran, S. A., Corson, D. A., & Sahni, O. (2014). Synthetic jet based active flow control of dynamic stall phenomenon on wind turbines under yaw misalignment. *32nd ASME wind energy symposium*, 0871.
- Truong, V. (1993). A 2d dynamic stall model based on a hopf bifurcation. *Unsteady aerodynamics — openfast documentation*. (n.d.). Retrieved April 9, 2024, from [https://openfast.readthedocs.io/en/main/source/user/aerodyn/theory\\_ua.html](https://openfast.readthedocs.io/en/main/source/user/aerodyn/theory_ua.html)
- Vasakova, L., E3MLab (Energy-Economy-Environment Modelling Laboratory) of the National Technical University of Athens, Capros, P., De Vita, A., Tasios, N., Chanioti, X., Kouvaritakis, N., & Fragkos, P. (2011, December 15). *Energy roadmap 2050*. [https://energy.ec.europa.eu/system/files/2014-10/roadmap2050\\_ia\\_20120430\\_en\\_0.pdf](https://energy.ec.europa.eu/system/files/2014-10/roadmap2050_ia_20120430_en_0.pdf)

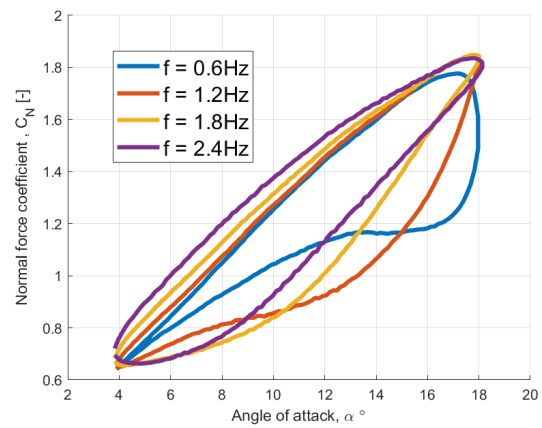
- Veers, P. (1985, May). *The effect of aerodynamic analysis on fatigue life estimation* (tech. rep.). Sandia National Laboratories, Albuquerque, NM.
- Visbal, M. R. (1990). Dynamic stall of a constant-rate pitching airfoil. *Journal of Aircraft*, 27(5), 400–407. <https://doi.org/10.2514/3.25289>
- Wong, J., Rival, D., et al. (2016). Wind shear, gust, and yaw-induced dynamic stall on wind-turbine blades. *Journal of Physics: Conference Series*, 753(3), 032023.
- Xi, L., & Zhao, L. (2022). Optimal design of wind turbine blades by combination of multi-airfoil leaf elements. *Journal of Physics: Conference Series*, 2235(1), 012008. <https://doi.org/10.1088/1742-6596/2235/1/012008>
- Ye, Z., Wang, X., Chen, Z., & Wang, L. (2020). Unsteady aerodynamic characteristics of a horizontal wind turbine under yaw and dynamic yawing. *Acta Mechanica Sinica*, 36, 320–338.
- Yoshida, S. (2020). Dynamic stall model for tower shadow effects on downwind turbines and its scale effects. *Energies*, 13(19), 5237.
- Zahle, F., Barlas, T., Lønbæk, K., Bortolotti, P., Zalkind, D., Wang, L., Labuschagne, C., Sethuraman, L., & Barter, G. (2024). Definition of the IEA Wind 22-Megawatt offshore reference wind turbine.



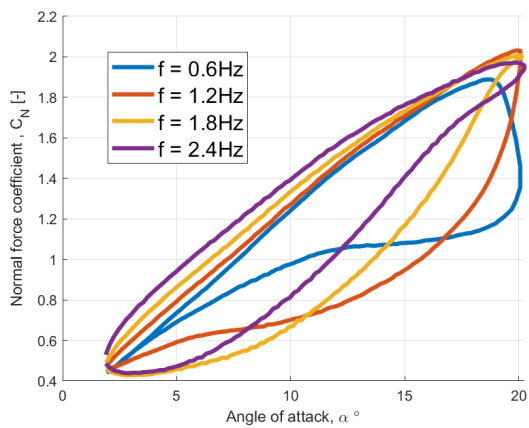
# Additional dynamic polars



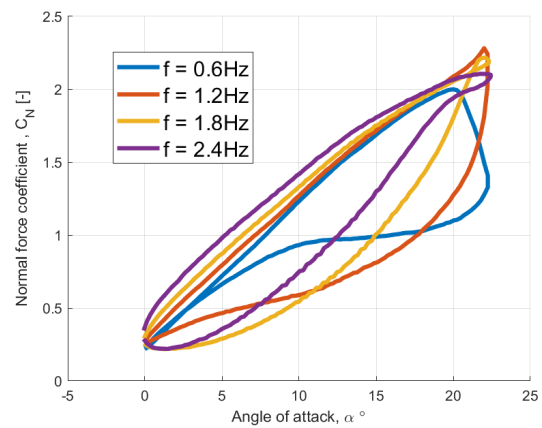
(a) Frequency dependence for  $C_N$  at  $Re = 5 \times 10^5$ ,  $A = 5^\circ$



(b) Frequency dependence for  $C_N$  at  $Re = 5 \times 10^5$ ,  $A = 7^\circ$

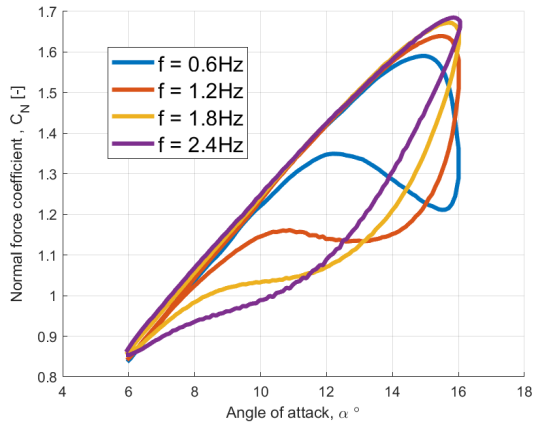


(c) Frequency dependence for  $C_N$  at  $Re = 5 \times 10^5$ ,  $A = 9^\circ$

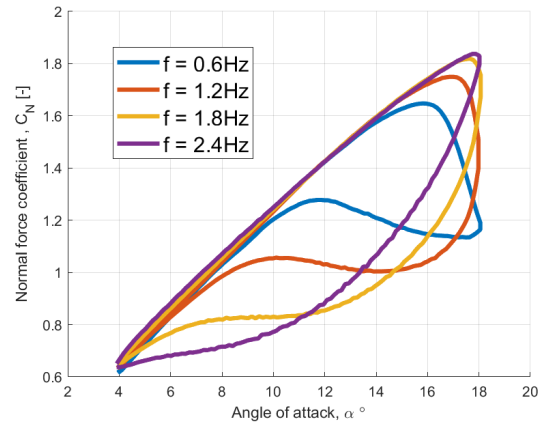


(d) Frequency dependence for  $C_N$  at  $Re = 5 \times 10^5$ ,  $A = 11^\circ$

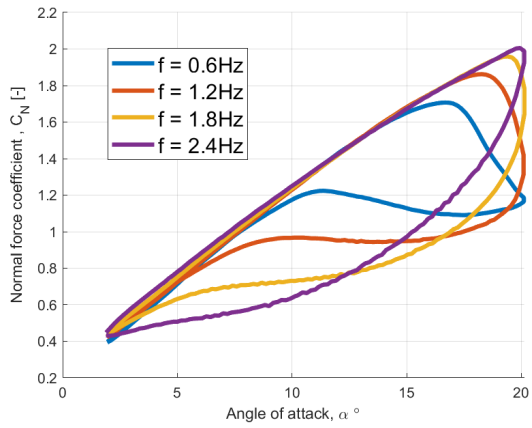
**Figure A.1:** Dynamic normal coefficient frequency dependence at  $Re = 5 \times 10^5$ ,  $\alpha_0 = 11^\circ$



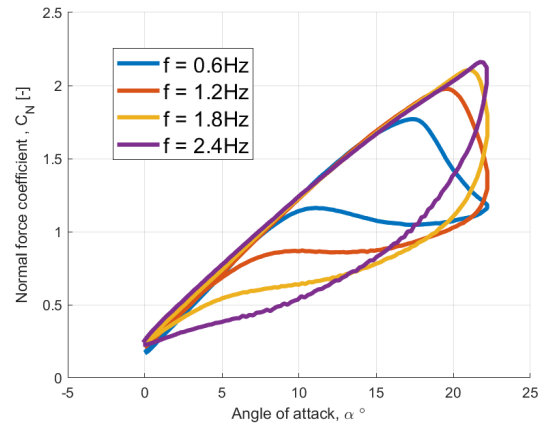
(a) Frequency dependence for  $C_N$  at  $Re = 1 \times 10^6$ ,  $A = 5^\circ$



(b) Frequency dependence for  $C_N$  at  $Re = 1 \times 10^6$ ,  $A = 7^\circ$



(c) Frequency dependence for  $C_N$  at  $Re = 1 \times 10^6$ ,  $A = 9^\circ$

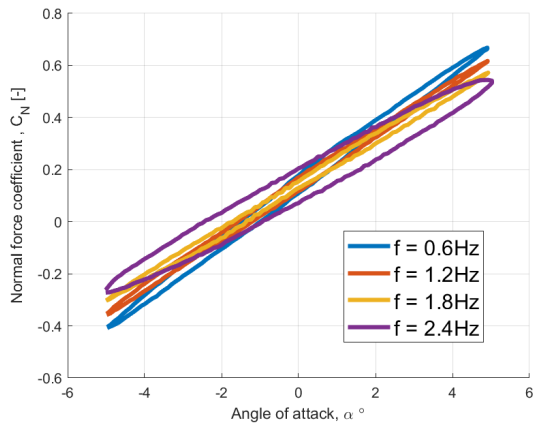


(d) Frequency dependence for  $C_N$  at  $Re = 1 \times 10^6$ ,  $A = 11^\circ$

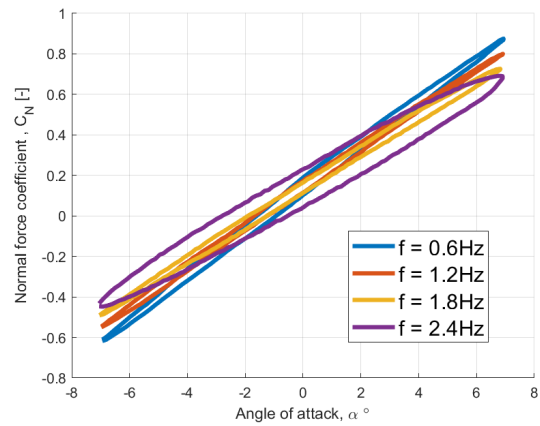
**Figure A.2:** Dynamic normal coefficient frequency dependence at  $Re = 1 \times 10^6$ ,  $\alpha_0 = -8^\circ$

# B

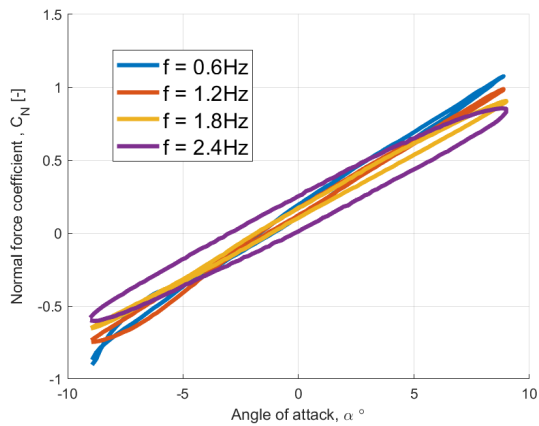
Figures for  $\alpha_0 = 0^\circ$



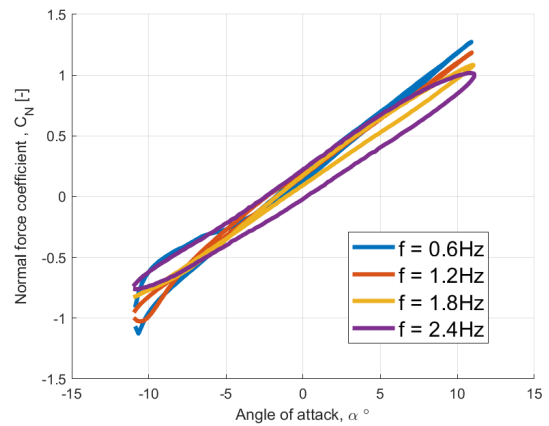
(a) Frequency dependence for  $C_N$  at  $Re = 5 \times 10^5$ ,  $A = 5^\circ$



(b) Frequency dependence for  $C_N$  at  $Re = 5 \times 10^5$ ,  $A = 7^\circ$

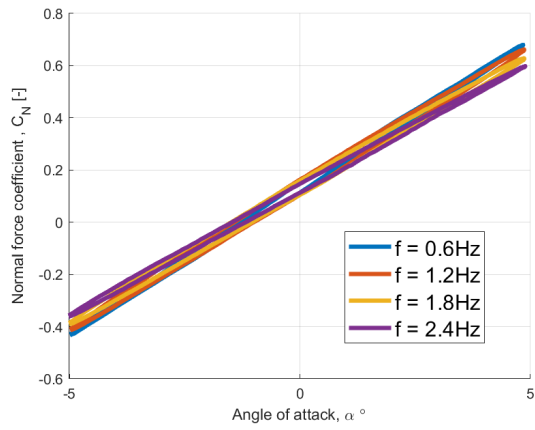


(c) Frequency dependence for  $C_N$  at  $Re = 5 \times 10^5$ ,  $A = 9^\circ$

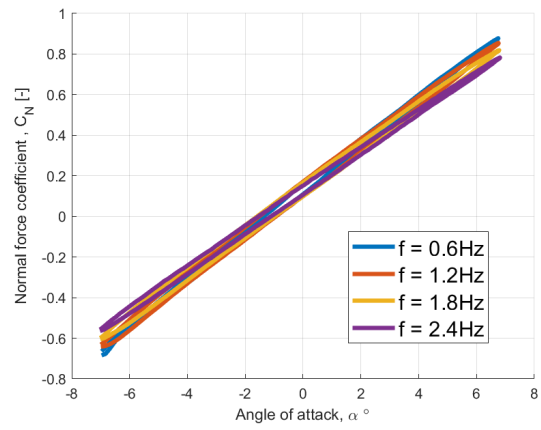


(d) Frequency dependence for  $C_N$  at  $Re = 5 \times 10^5$ ,  $A = 11^\circ$

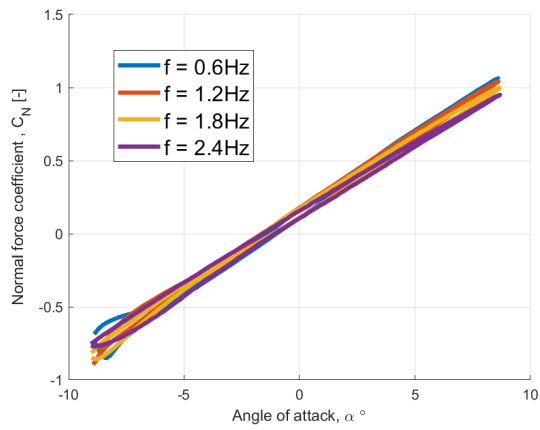
**Figure B.1:** Dynamic normal coefficient frequency dependence at  $Re = 5 \times 10^5$ ,  $\alpha_0 = 0^\circ$



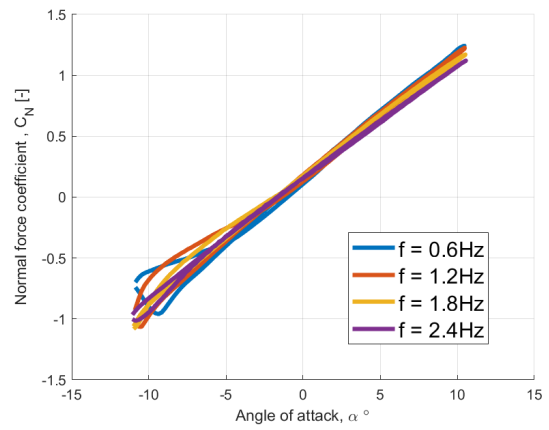
(a) Frequency dependence for  $C_N$  at  $Re = 1 \times 10^6$ ,  $A = 5^\circ$



(b) Frequency dependence for  $C_N$  at  $Re = 1 \times 10^6$ ,  $A = 7^\circ$

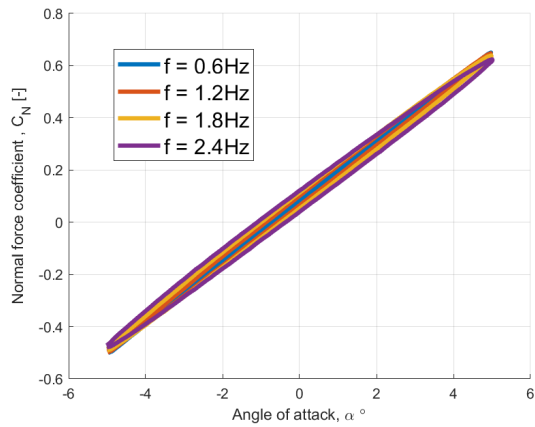


(c) Frequency dependence for  $C_N$  at  $Re = 1 \times 10^6$ ,  $A = 9^\circ$

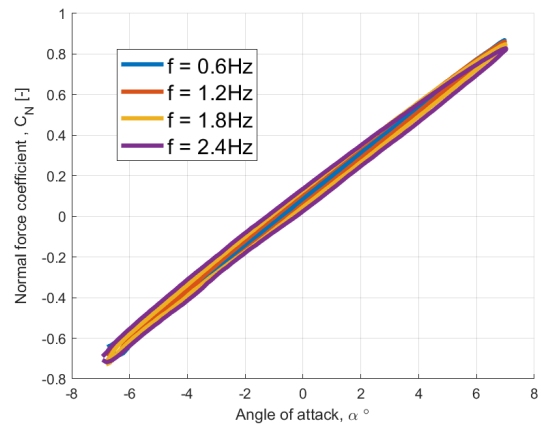


(d) Frequency dependence for  $C_N$  at  $Re = 1 \times 10^6$ ,  $A = 11^\circ$

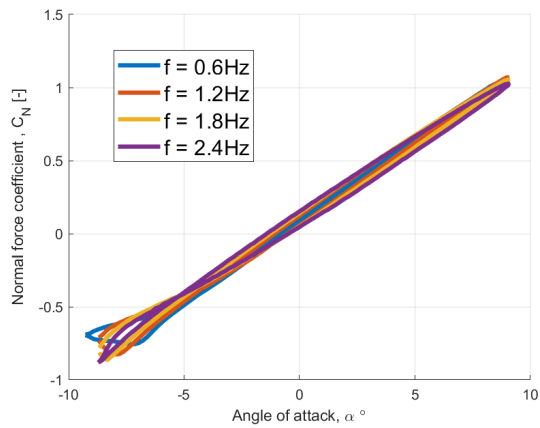
**Figure B.2:** Dynamic normal coefficient frequency dependence at  $Re = 1 \times 10^6$ ,  $\alpha_0 = 0^\circ$



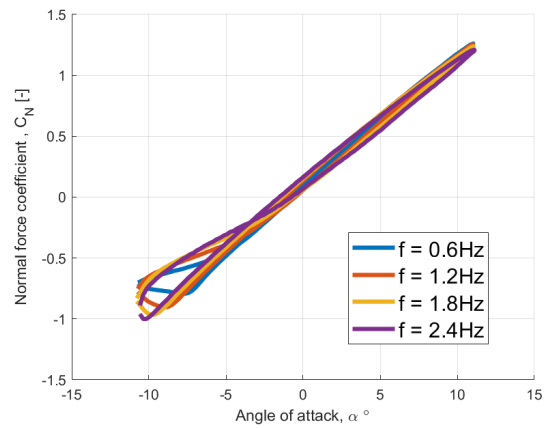
(a) Frequency dependence for  $C_N$  at  $Re = 2 \times 10^6$ ,  $A = 5^\circ$



(b) Frequency dependence for  $C_N$  at  $Re = 2 \times 10^6$ ,  $A = 7^\circ$

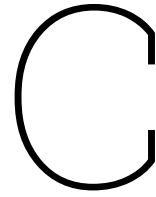


(c) Frequency dependence for  $C_N$  at  $Re = 2 \times 10^6$ ,  $A = 9^\circ$



(d) Frequency dependence for  $C_N$  at  $Re = 2 \times 10^6$ ,  $A = 11^\circ$

**Figure B.3:** Dynamic normal coefficient frequency dependence at  $Re = 2 \times 10^6$ ,  $\alpha_0 = 0^\circ$



## $T_P$ coefficient determination

Below, the MATLAB implementation of  $T_P$  coefficient is presented. In addition to the fitted lines for  $Re = 1 \times 10^6$  and  $Re = 2 \times 10^6$  separately, denoted with subscripts  $_1$  and  $_2$  respectively, the code also contain a commented lines 182. This line adds a fitted line for both Reynolds number combined.

Additionally, the code differs between the positive and negative mean AoA's. The difference can be observed in lines 106 and 122, where the *max* and *min* functions are used to find the corresponding stall onset angle at max/min value of  $CN$ .

```
1
2 %% DETERMINATION OF THE TP COEFFICIENT
3
4 % Clear workspace, close all figures, and clear command window
5 clear all
6 close all
7 clc
8
9 %% File and Folder Setup
10
11 % Path to the folder containing files
12 folder_path = 'D:\OneDrive \MSc Thesis\Matlab\exp_res';
13
14 % Define variable values for different cases
15
16 % % For negative AoA
17 % Re_values = {'1000000_m','2000000_m'};
18 % meanAngle_values = {'_n8'};
19 % ample_values = {'_ampl_3','_ampl_11','_ampl_9', '_ampl_7','_ampl_5'};
20 % freq_values = {'_f_12', '_f_18', '_f_24'};
21
22 % For positive AoA
23 % Uncomment this section and comment the previous section for positive AoA
24 Re_values = {'1000000_m','2000000_m'};
25 meanAngle_values = {'_11'};
26 ample_values = {'_ampl_11','_ampl_9', '_ampl_7', '_ampl_5'};
27 freq_values = {'_f_6','_f_12', '_f_18', '_f_24'};
28
29 % Predefined variables to save the results
30 allPitchRates = [];
31 allTimes = [];
32 allalpha_ds = [];
33
34 %% Data Processing Loop
35
36 % Looping across the data
37 for Re = Re_values
38     for meanAngle = meanAngle_values
39         for ample = ample_values
40             for freq = freq_values
41
42                 % File name construction
43                 file_name = strcat(Re, meanAngle, ample, freq);
44                 full_file_path = fullfile(folder_path, strcat(file_name, '.mat'));
45
46                 % Check if the file exists
47                 if exist(char(full_file_path), 'file') == 2
```

```

48 % Load data from the file
49 data = load(char(full_file_path));
50
51 % Extract necessary variables
52 allalpha = data.allalpha;
53 allCN = data.allCN;
54 amplitude = data.amplitude;
55 upcn = data.upcn;
56 downcn = data.downcn;
57 alphavect1 = data.alphavect1;
58 alphavect2 = data.alphavect2;
59 frequency_int = data.frequency_int;
60 mean_aoa_int = data.mean_aoa_int;
61 cnuardown = [upcn, downcn];
62 alphaupdown = [alphavect1, alphavect2];
63 %% Calculation of Reduced Frequencies
64 % Assigning the correct reduced frequencies based on the Re and f
65 if data.reynolds_indicator == 1
66     if data.frequency_int == 0.6
67         k = 0.091;
68     elseif data.frequency_int == 1.2
69         k = 0.182;
70     elseif data.frequency_int == 1.8
71         k = 0.273;
72     elseif data.frequency_int == 2.4
73         k = 0.364;
74     end
75 elseif data.reynolds_indicator == 2
76     if data.frequency_int == 0.6
77         k = 0.046;
78     elseif data.frequency_int == 1.2
79         k = 0.091;
80     elseif data.frequency_int == 1.8
81         k = 0.137;
82     elseif data.frequency_int == 2.4
83         k = 0.182;
84     end
85 elseif data.reynolds_indicator == 3
86     if data.frequency_int == 0.6
87         k = 0.046;
88     elseif data.frequency_int == 1.2
89         k = 0.091;
90     elseif data.frequency_int == 1.8
91         k = 0.137;
92     elseif data.frequency_int == 2.4
93         k = 0.182;
94     end
95 end
96
97 %% Dynamic Stall Parameters Calculation
98
99 % Dynamic stall onset angle calculation
100 if data.mean_aoa_int == -8
101     % Creating the time and AoA of moving airfoil
102     time = 1/(2*frequency_int):0.001: 1/frequency_int;
103     AoA = deg2rad(mean_aoa_int) + deg2rad(amplitude)*sin(2*pi*frequency_int*time+(pi
104         /2));
105
106     % Finding the dynamic stall onset angle
107     [~, minIndex] = min(cnuardown);
108     alpha_ds = round(alphaupdown(minIndex),3);
109
110     % Locating the closest value on the created timeline
111     [~, index] = min(abs(AoA - alpha_ds));
112
113     % Getting the time of the DS onset
114     time_ds = round(time(index),3);
115
116     % Getting the value of the pitchrate at the DS onset
117     pitchrate_ds = abs(k * deg2rad(amplitude) * cos(2 * pi * frequency_int * time_ds
118         ));
119
120 elseif data.mean_aoa_int == 11
121     time = 0:0.001: 1/(2*frequency_int);
122     AoA = deg2rad(mean_aoa_int) + deg2rad(amplitude)*sin(2*pi*frequency_int*time+(pi
123         /2));
124
125     [~, maxIndex] = max(cnuardown);
126     alpha_ds = alphaupdown(maxIndex);
127
128     % Locating the closest value on the created timeline
129     [~, index] = min(abs(AoA - alpha_ds));
130
131     % Getting the time of the DS onset

```

```

129         time_ds = round(time(index),3);
130
131         % Getting the value of the pitchrate at the DS onset
132         pitchrate_ds = abs(k * deg2rad(amplitude) * cos(2 * pi * frequency_int * time_ds)
133             );
134     end
135     %% Results Saving
136     % Saving the results
137     allPitchRates = [allPitchRates, pitchrate_ds];
138     allTimes = [allTimes, time_ds];
139     allalpha_ds = [allalpha_ds, alpha_ds];
140 end
141     end
142 end
143 end
144 end
145
146 %% Plotting
147
148 % Plotting the final values
149 figure
150 plot(allPitchRates(1:15), allalpha_ds(1:15), 'x', 'LineWidth',2)
151 hold on
152 plot(allPitchRates(16:30), allalpha_ds(16:30), 'x', 'LineWidth',2)
153 grid on
154 ylabel('Dynamic stall onset angle, \alpha_{ds} [\circ]')
155 xlabel('Reduced pitch, r [-]')
156
157 % Fit a line for 1 mil Re
158 coefficients1 = polyfit(allPitchRates(1:15), deg2rad(allalpha_ds(1:15)), 1);
159 % Fit a line for 2 mil Re
160 coefficients2 = polyfit(allPitchRates(16:30), deg2rad(allalpha_ds(16:30)), 1);
161 % Fit a line for all values
162 coefficients = polyfit(allPitchRates, deg2rad(allalpha_ds), 1);
163
164 % Get the slope of the fitted line
165 slope1 = coefficients1(1);
166 slope2 = coefficients2(1);
167 slope = coefficients(1);
168
169 % Create strings with the slope values
170 slopeText1 = sprintf('Slope for 1*10^6 Re: %.4f', slope1);
171 slopeText2 = sprintf('Slope for 2*10^6 Re: %.4f', slope2);
172
173 % Plotting the fitted lines
174 x_values = linspace(min(allPitchRates), max(allPitchRates), 100);
175 y_values1 = polyval(coefficients1, x_values);
176 y_values2 = polyval(coefficients2, x_values);
177 y_values = polyval(coefficients, x_values);
178
179 plot(x_values, rad2deg(y_values1), 'b--', 'LineWidth', 1.5, 'DisplayName', slopeText1);
180 plot(x_values, rad2deg(y_values2), 'r--', 'LineWidth', 1.5, 'DisplayName', slopeText2);
181 % To plot the combined slope
182 % plot(x_values, rad2deg(y_values), 'k--', 'LineWidth', 1.5, 'DisplayName', 'Overall Slope');
183
184 legend('Re = 1*10^6','Re = 2*10^6',slopeText1, slopeText2,'Location','best');

```

# D

## Beddoes-Leishman cases comparison

### D.1. Oscillation around a mean angle of $\alpha_0 = 11^\circ$

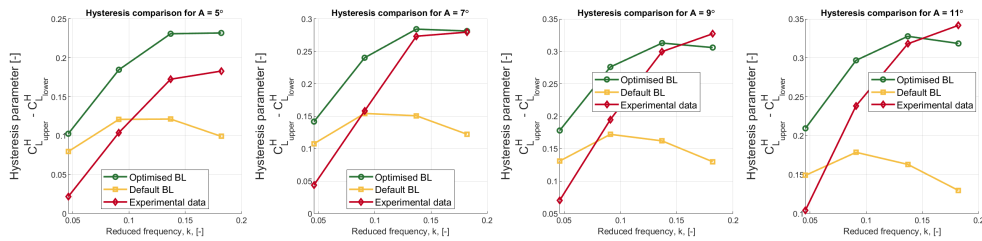


Figure D.1: Hysteresis parameter comparison for  $11^\circ$  oscillation for  $1 \times 10^6$  Re

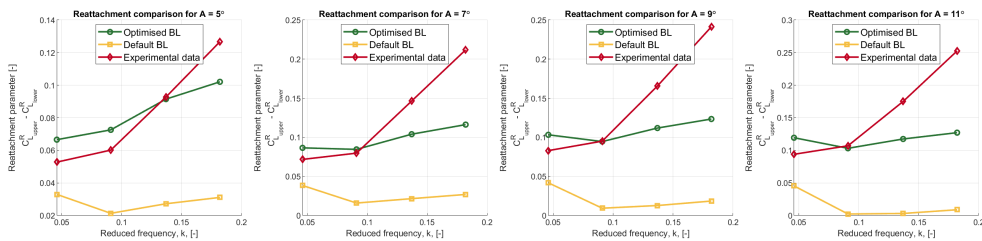


Figure D.2: Reattachment parameter comparison for  $11^\circ$  oscillation for  $1 \times 10^6$  Re

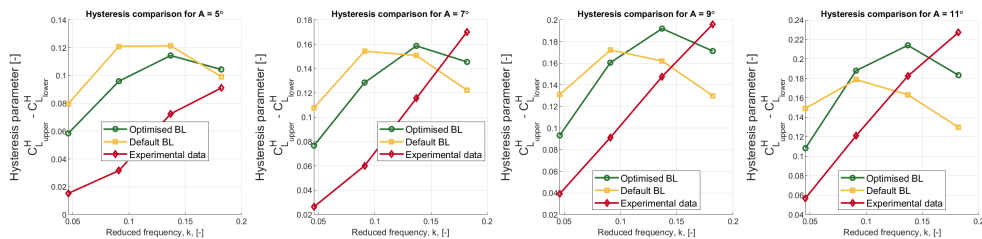


Figure D.3: Hysteresis parameter comparison for  $11^\circ$  oscillation for  $2 \times 10^6$  Re

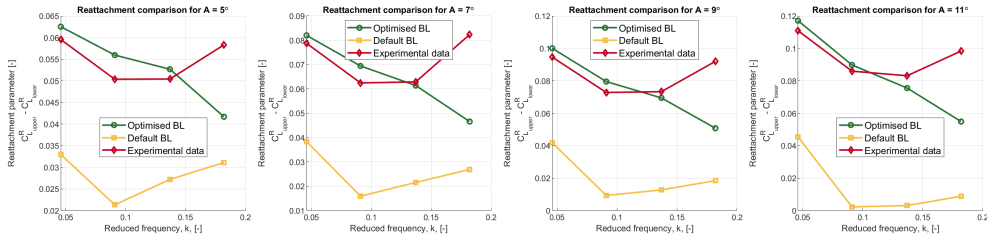


Figure D.4: Reattachment parameter comparison for  $11^\circ$  oscillation for  $2 * 10^6$  Re

D.2. Oscillation around a mean angle of  $\alpha_0 = -8^\circ$

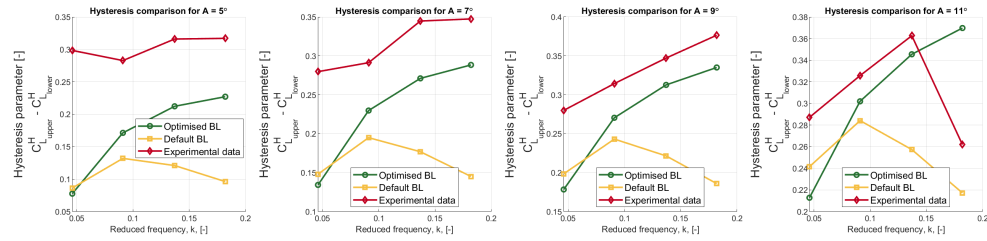


Figure D.5: Hysteresis parameter comparison for  $-8^\circ$  oscillation for  $1 * 10^6$  Re

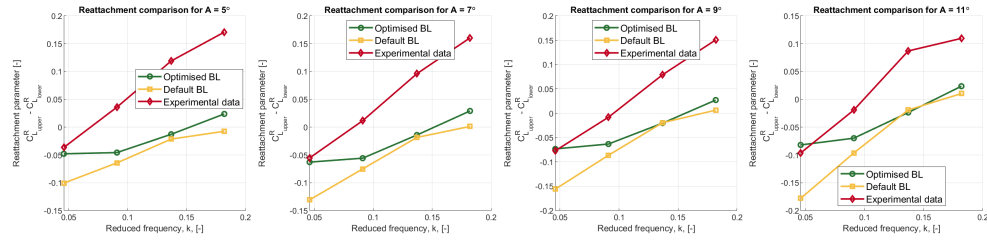


Figure D.6: Reattachment parameter comparison for  $-8^\circ$  oscillation for  $1 * 10^6$  Re

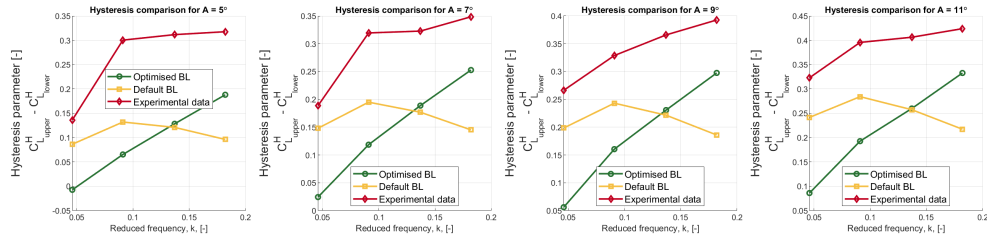


Figure D.7: Hysteresis parameter comparison for  $-8^\circ$  oscillation for  $2 * 10^6$  Re

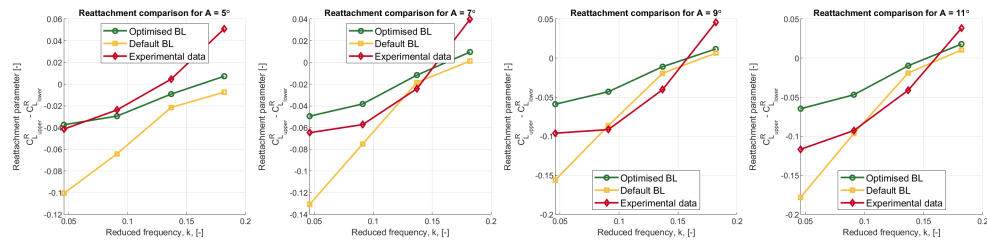
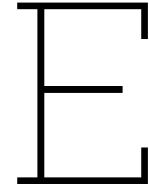


Figure D.8: Reattachment parameter comparison for  $-8^\circ$  oscillation for  $2 * 10^6$  Re



# Snel cases comparison

## E.1. Oscillation around a mean angle of $\alpha_0 = 11^\circ$

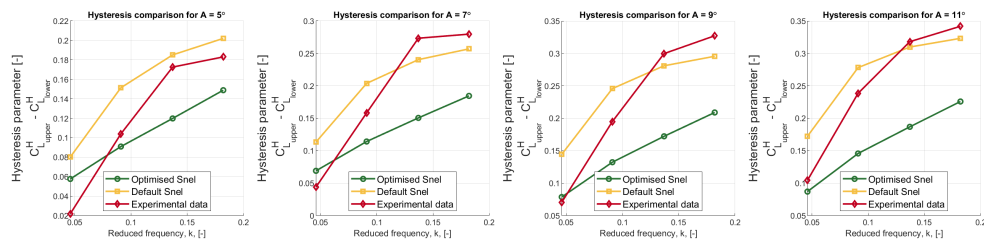


Figure E.1: Hysteresis parameter comparison for  $11^\circ$  oscillation for  $1 \times 10^6$  Re

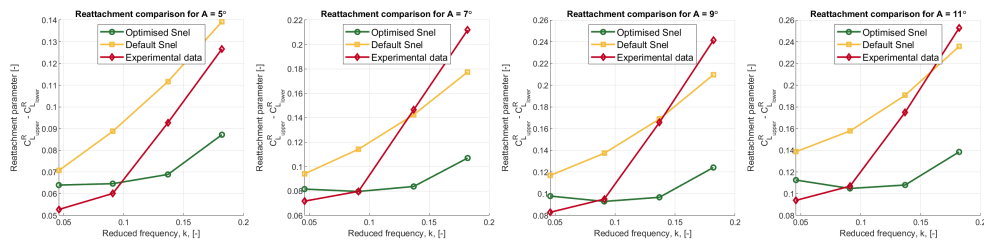


Figure E.2: Reattachment parameter comparison for  $11^\circ$  oscillation for  $1 \times 10^6$  Re

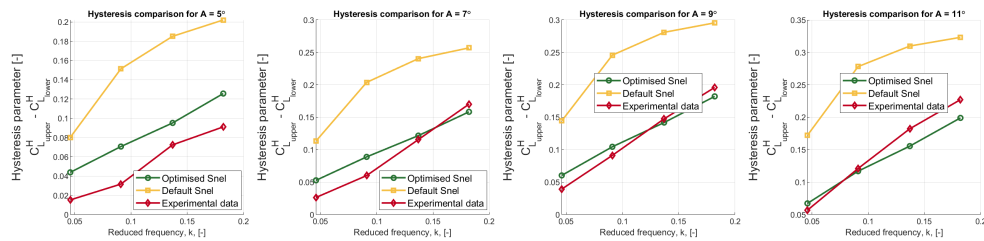


Figure E.3: Hysteresis parameter comparison for  $11^\circ$  oscillation for  $2 \times 10^6$  Re

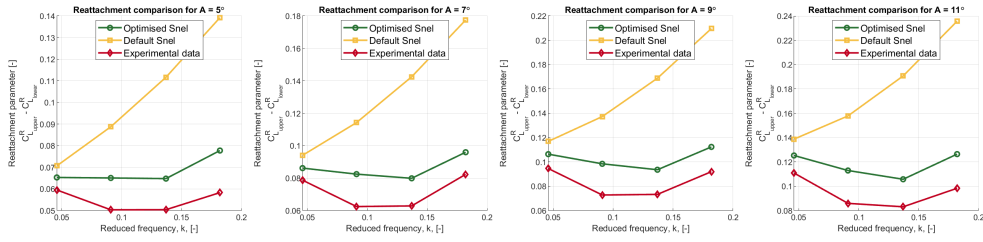


Figure E.4: Reattachment parameter comparison for  $11^\circ$  oscillation for  $2 * 10^6$  Re

E.2. Oscillation around a mean angle of  $\alpha_0 = -8^\circ$

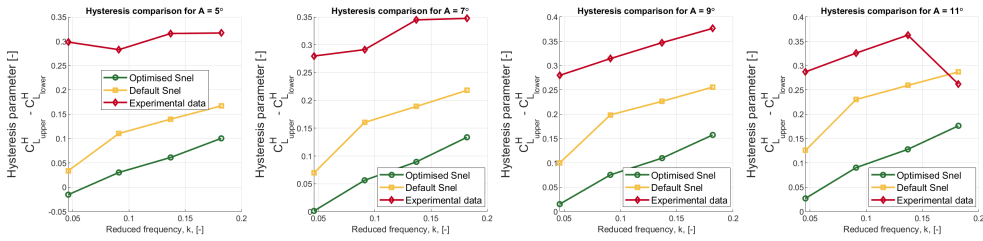


Figure E.5: Hysteresis parameter comparison for  $-8^\circ$  oscillation for  $1 * 10^6$  Re

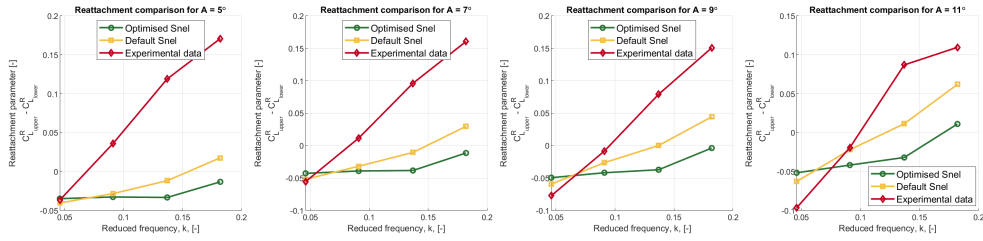


Figure E.6: Reattachment parameter comparison for  $-8^\circ$  oscillation for  $1 * 10^6$  Re

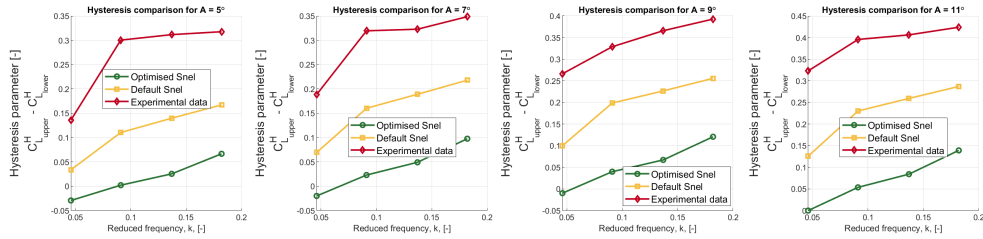


Figure E.7: Hysteresis parameter comparison for  $-8^\circ$  oscillation for  $2 * 10^6$  Re

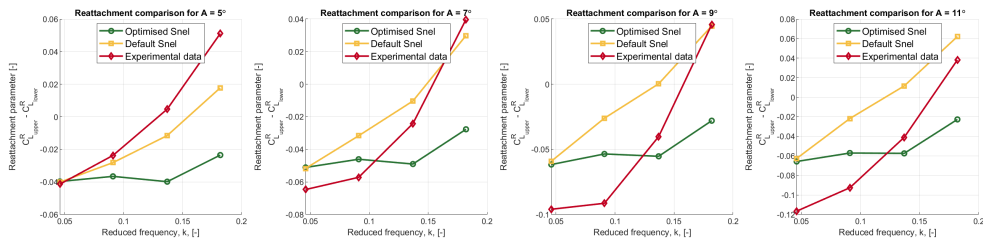


Figure E.8: Reattachment parameter comparison for  $-8^\circ$  oscillation for  $2 * 10^6$  Re